

Copyright

by

Yifei Xu

2015

The Thesis Committee for Yifei Xu
Certifies that this is the approved version of the following thesis:

**Implementation and Application of the Embedded Discrete Fracture
Model (EDFM) for Reservoir Simulation in Fractured Reservoirs**

APPROVED BY
SUPERVISING COMMITTEE:

Supervisor:

Kamy Sepehrnoori

Lee Chin

**Implementation and Application of the Embedded Discrete Fracture
Model (EDFM) for Reservoir Simulation in Fractured Reservoirs**

by

Yifei Xu, B.E.

Thesis

Presented to the Faculty of the Graduate School of
The University of Texas at Austin
in Partial Fulfillment
of the Requirements
for the Degree of

Master of Science in Engineering

The University of Texas at Austin
December 2015

Dedication

To my beloved parents Zhongzheng and Lihong,
for their endless love, support and encouragement

Acknowledgements

I would like to express my deepest gratitude to my supervisor, Dr. Kamy Sepehrnoori, for his insightful ideas, excellent supervision and consistent support throughout my Master study. His knowledge and intuition in reservoir simulation have always guided me to explore this area.

I am grateful to Dr. Lee Chin, for his time and effort to review my thesis. I benefit so much from the invaluable comments and feedback he provided.

I would like to thank Dr. Chowdhury Mamun for his careful review of my thesis. I learned a lot of writing skills from his helpful comments.

I would like to thank Mahmood Shakiba, for his time in teaching me the Embedded Discrete Fracture Model (EDFM) and UTCOMP. The technical discussion with him deepened my understanding of reservoir simulation. I would also like to thank Jose Sergio Cavalcante, who is the developer of the EDFM preprocessor. He was always ready and eager to help me in fixing bugs in the code and changing the output format the preprocessor. I also enjoyed the discussion of the EDFM with him. I would also like to express my gratitude to Dr. Ali Moinfar, who was the first student working on the EDFM in our research group. His excellent work is the basis of my research.

I would like to thank Dr. Wei Yu for his helpful discussions with me regarding unconventional reservoirs. I benefited much from his suggestions in my research directions. I also learned software skills and writing skill from him. Special thanks go to Dr. Hamid Reza Lashgari and Dr. Aboulghasem Kazemi Nia, for their patience in answering so many questions from me. I will also extend my thanks to all my friends and officemates, for the great time I spent with them at UT.

I express my appreciation to Dr. Håkon Høgstøl from Statoil, for bringing “Fishbone well”, which is a very interesting research topic, to our research group. This topic has greatly expanded the range of problems we are working on.

I appreciate the financial support from Statoil and the members of Reservoir Simulation Joint Industry Project (RSJIP) at the Center for Petroleum and Geosystems Engineering at The University of Texas at Austin.

Finally, I would like to express my deepest gratitude to my parents, for their continuous love and endless support during my study. Their encouragement constantly motivated me in my work and life. I would also like to express my thanks to my best friend, Yue Zhang. She is the most beautiful girl I have ever seen in my life. I treasure every moment with her and her smiles are the source of my happiness.

Abstract

Implementation and Application of the Embedded Discrete Fracture Model (EDFM) for Reservoir Simulation in Fractured Reservoirs

Yifei Xu, M.S.E.

The University of Texas at Austin, 2015

Supervisor: Kamy Sepehrnoori

Fractured reservoirs have gained continuous attention from oil and gas industry. A huge amount of hydrocarbon are trapped in naturally fractured carbonate reservoirs. Besides, the advanced technology of multi-stage hydraulic fracturing have gained a great success in economic development of unconventional oil and gas reservoirs. Fractures add complexity into reservoir flow and significantly impact the ultimate recovery. Therefore, it is important yet challenging to accurately and effectively predict the recovery from fractured reservoirs. Conventional dual-continuum approaches, although effective in the simulation of naturally fractured reservoirs, may fail in some cases due to the highly idealized reservoir model. The unstructured-grid discrete fracture models, although flexible in representing complex fracture geometries, are restricted by the high complexity in gridding and high computational cost.

An Embedded Discrete Fracture Model (EDFM) was recently developed to honor the accuracy of discrete fracture models while keeping the efficiency offered by structured gridding. By dividing the fractures into segments using matrix cell boundaries and creating

non-neighboring connections (NNCs), the flow influence of fractures can be efficiently modeled through transport indices. In this work, the EDFM was implemented in UTCHEM, a chemical flooding in-house reservoir simulator developed at The University of Texas, to study complex recovery processes in fractured reservoirs. In addition, the model was applied in commercial simulators by making use of the non-intrusive property of the EDFM and the NNC functionality offered by the simulators. The accuracy of the EDFM in the modeling of orthogonal, non-orthogonal, and inclined fractures was verified against fine-grid explicit fracture simulations. Furthermore, case studies were performed to investigate the influence of hydraulic fracture orientations on primary depletion and the impact of large-scale natural fractures on water flooding processes. The influence of matrix grid size and fracture relative permeability was also studied. Finally, with modifications in NNC transmissibility calculation, the EDFM was applied to the modeling of a multi-lateral well stimulation technology. The accuracy of the modified formulations was verified through comparison with a multi-branch well method. The simulations carried out in this work confirmed the flexibility, applicability, and extensiveness of the EDFM.

Table of Contents

List of Tables	xii
List of Figures	xiii
Chapter 1: Introduction	1
1.1 Reservoir Simulation for Fractured Reservoirs	1
1.2 Objectives of This Research	4
1.3 Brief Description of Chapters	5
Chapter 2: Literature Review	6
2.1 Dual-Continuum Models	6
2.2 Discrete Fracture Models	13
2.3 Analytical Solutions	18
Chapter 3: Overview of UTCHEM Reservoir Simulator and the Embedded Discrete Fracture Model (EDFM)	20
3.1 UTCHEM Reservoir simulator	20
3.1.1 Features of UTCHEM	21
3.1.2 Governing Equations	22
3.1.2.1 Mass Conservation Equation	22
3.1.2.2 Pressure Equation	23
3.1.2.3 Energy Conservation Equation	24
3.1.2.4 Constitutive Relations	25
3.2 Embedded Discrete Fracture Model (EDFM)	25
3.2.1 Development of the EDFM	25
3.2.2 Methodology Description	28
3.2.3 Calculation of the NNC Transmissibility Factors and Fracture Well Index	31
3.2.3.1 Matrix-Fracture Connection	31
3.2.3.2 Connection between Fracture Segments in an Individual Fracture	32
3.2.3.3 Fracture Intersection	34

3.2.3.4 Well-Fracture Intersection	36
3.2.4 Porosity cutoff method.....	37
3.2.5 EDFM Preprocessor.....	38
3.3 Highlights of the chapter.....	40
 Chapter 4: Model Implementation and Verification.....	41
4.1 Implementation of the EDFM in Reservoir Simulators.....	41
4.1.1 EDFM in UTCHEM Reservoir Simulator	41
4.1.2 EDFM in Commercial Reservoir Simulators.....	45
4.2 Model Verifications	47
4.2.1 3D Orthogonal Fractures.....	47
4.2.2 2D Non-Orthogonal Fractures	54
4.2.3 3D Inclined Fracture	60
4.3 Highlights of the chapter.....	65
 Chapter 5: Application of the Embedded Discrete Fracture Model (EDFM) using UTCHEM and Commercial Simulators.....	66
5.1 Influence of Fracture-Well Intersection Angle	66
5.2 Water Flooding in Naturally Fractured Reservoir	76
5.3 Fishbone Well Simulation With The EDFM	87
5.3.1 Multi-lateral Well Stimulation Technology.....	87
5.3.2 Modeling Fishbones Using the Modified EDFM Formulations .	89
5.3.3 Multi-Branch Well Method.....	93
5.3.4 Comparison of the Modified EDFM and the Multi-Branch Well Method	94
5.3.5 Simulation result analysis	100
5.3.5.1 Fishbone Lateral Number Impact	100
5.3.5.2 Reservoir Anisotropy Impact.....	101
5.3.6 Porosity Cutoff Application.....	102
5.4 Highlights of the chapter.....	103
 Chapter 6: Summary, Conclusions and Recommendations	105
6.1 summary and conclusions	105

6.2 Recommendations for future work	107
Nomenclature.....	110
References.....	114

List of Tables

Table 4.1:	Reservoir properties and some of the simulation parameters.	49
Table 4.2:	Reservoir properties and some of the simulation parameters.	56
Table 4.3:	Reservoir properties and some of the simulation parameters.	61
Table 4.4:	Gridding information for the EDFM simulations. Three different grid sizes are used.....	63
Table 5.1:	Reservoir properties and some of the simulation parameters.	69
Table 5.2:	Reservoir properties and some of the simulation parameters.	79
Table 5.3:	Reservoir properties and some of the simulation parameters.	97
Table 5.4:	CPU time for different porosity cutoff values.	103

List of Figures

Figure 2.1: Reservoir idealization in dual porosity models.....	7
Figure 2.2: Discretization of matrix blocks (a) MINC (b) dual porosity (c) explicit discretization (Wu and Pruess 1988).	11
Figure 2.3: Comparison of the connections in dual porosity and dual permeability models (Dean and Lo 1988).....	12
Figure 2.4: Unstructured discretization of the fractured media using Delaunay triangulation (Karimi-Fard et al. 2004).....	16
Figure 2.5: Pressure distribution predicted by a discrete fracture model using unstructured grids (Cipolla et al. 2011a). The model has been implemented in a commercial simulator.....	17
Figure 2.6: Pressure distribution of a complex fracture network predicted by semi-analytical solution (Zhou et al. 2014).	19
Figure 3.1: Explanation of EDFM. In (a) we show a Case with 3 matrix blocks, 2 fractures, and a wellbore in physical domain. In (b) we show the corresponding cells in computational domain and the arrows show different types of connections.....	30
Figure 3.2: Illustration of the connection between matrix cell and fracture segment.	31
Figure 3.3: An example of different shapes of fracture segments in an individual fracture. The fracture is cut into 29 segments by the cell boundaries shown in (a). In (b), the segments are colored based on number of vertices. They can be triangle, quadrilateral, pentagon, or hexagon.	33

Figure 3.4: Illustration of the fracture intersection. At the intersection, every fracture segment is divided into 2 subsegments. In (a), all the subsegments have similar dimensions. In (b), there is a high contrast between areas of the subsegments	35
Figure 3.5: Illustration of the well-fracture intersection. The blue tube represents a wellbore and the red plane represents a fracture segment in a matrix gridblock.	36
Figure 4.1: A reservoir model with 8 intersecting orthogonal fractures.	48
Figure 4.2: Illustration of local grid refinement at the fracture intersections in the fine model. The white box shows the size of the coarse gridblock. The sub-cells representing fractures are shown in orange and the sub-cells representing matrix are shown in blue.	50
Figure 4.3: Comparison of average reservoir pressure for different models.....	51
Figure 4.4: Comparison of (a) oil rate and (b) water rate of different models. Both of the rates are in reservoir condition. The oil rate is shown in log scale as it changes very rapidly during the early time.....	52
Figure 4.5: Pressure profiles of Layer 5 predicted by (a) UTCHEM-EDFM and (b) CMG-LGR. The rows from top to bottom show the pressure profiles for 5 days and 32 days, respectively.....	53
Figure 4.6: A reservoir model with 4 non-orthogonal fractures. Fractures have an intersection angle of 63° with the wellbore.	56
Figure 4.7: Explanation of “zigzag” in the fine model. The red lines in (a) represents the high permeability sub-grids for fractures. A closer view is given in (b), where the red line shows the actual fracture shape and the blue lines show the “zigzag” representation of the fracture shape.....	57

Figure 4.8: Comparison of average reservoir pressure for different models.....	58
Figure 4.9: Comparison of oil production rates (reservoir condition) for different models. The oil rate is shown in log scale due to its rapid change during early time.	58
Figure 4.10: Pressure profiles predicted by (a) UTCHEM-EDFM and (b) CMG-LGR. The rows from top to bottom show the pressure profiles for 20 days, 90 days and 300 days, respectively.....	59
Figure 4.11: A reservoir model with an inclined fractures.....	61
Figure 4.12: High permeability cells in the fine-grid model.	62
Figure 4.13: Comparison of average reservoir pressure predicted by fine-grid models and the EDFM approach with different matrix grid size.	63
Figure 4.14: Pressure profiles predicted by (a) EDFM using a $5 \times 5 \times 5$ matrix grid (b) EDFM using a $10 \times 10 \times 10$ matrix grid (c) EDFM using a $20 \times 20 \times 20$ matrix grid (d) Fine-grid model using a $70 \times 70 \times 70$ grid.....	64
Figure 5.1: A reservoir model with 4 non-orthogonal fractures. Fractures have an angle of α with the X axis.....	68
Figure 5.2: Relative permeability curves for (a) matrix cells and (b) fracture cells.	69
Figure 5.3: Positions of the fractures with different α . Lines with different colors show fractures with different well-fracture intersection angles. Five values of α are chosen in this study (90° , 75° , 60° , 45° , and 30°).70	70
Figure 5.4: Average reservoir pressure for different fracture angles.	72
Figure 5.5: Cumulative oil production (reservoir condition) for different fracture angles.	72

Figure 5.6: Oil production rates (reservoir condition) for different fracture angles at early time and late time.....	73
Figure 5.7: Pressure profiles predicted by UTCHEM-EDFM at 60 days for (a) $\alpha=90^\circ$ (b) $\alpha=75^\circ$ (c) $\alpha=60^\circ$ (d) $\alpha=45^\circ$, and (e) $\alpha=30^\circ$	74
Figure 5.8: Pressure profiles at 200 days for (a) $\alpha=90^\circ$ (b) $\alpha=30^\circ$. Radial flow can be observed.	75
Figure 5.9: Cumulative oil production (reservoir condition) for different α after 100 days, 500 days, and 1000 days.....	76
Figure 5.10: A reservoir model with 8 large-scale fractures. The blue circles represent injectors and the green circles represent producers. The fractures are represented by red lines.	77
Figure 5.11: 3D views of the fractures planes. (a) Top view. (b) Slanted view. The numbers in (a) represent the dip angles of the fractures.	78
Figure 5.12: Oil Saturation profiles (bottom layer) after 500 days. (a) Without fractures (b) With fractures.....	80
Figure 5.13: Comparison of the producers' oil production rates (reservoir condition) for cases with and without fractures ("Frac" and "No frac").....	81
Figure 5.14: Water Saturation profiles after 500 days predicted by the EDFM. (a) Top layer (b) Bottom layer.....	81
Figure 5.15: Oil production rates (reservoir condition) predicted by the EDFM using different grid resolutions.....	82
Figure 5.16: Oil Saturation profiles (bottom layer) after 500 days predicted by the EDFM with (a) $20 \times 20 \times 2$ grid (b) $60 \times 60 \times 2$ grid (c) $100 \times 100 \times 2$ grid.	83

Figure 5.17: Oil Saturation profiles (bottom layer) after 500 days predicted by the EDFM using different fracture relative permeability models. (a) Straight-line model (b) Corey model (the same as matrix).....	85
Figure 5.18: Oil production rates (reservoir condition) for different fracture relative permeability models.....	86
Figure 5.19: Relative mobility for different relative permeability models. (a) Straight-line model (b) Corey model (the same as matrix).....	86
Figure 5.20: A 3D visualization of the Fishbone well (http://www.fishbones.as).88	
Figure 5.21: A schematic for the Fishbones stimulation system (Carvajal et al. 2015).	88
Figure 5.22: Illustration of the fishbone modeling methodology. We model the fishbone laterals as equivalent fractures in this study.....	89
Figure 5.23: Explanation of the transport index calculations in the fishbone well modeling.	92
Figure 5.24: Reservoir dimensions and location of the horizontal well and fishbone subs.	96
Figure 5.25: Positions of the fishbone subs for cases with (a) 4 fishbone laterals (b) 8 fishbone laterals (c) 16 fishbone laterals and (d) 60 fishbone laterals.97	
Figure 5.26: Comparison of cumulative oil production (reservoir condition) between multi-branch approach and the EDFM approach for the isotropic case. Different curves show results for different numbers of fishbone laterals.	98

Figure 5.27: Comparison of cumulative oil production (reservoir condition) between multi-branch approach and the EDFM approach for the anisotropic case. Different curves show results for different numbers of fishbone laterals.

.....98

Figure 5.28: Pressure profiles after 5 days predicted by (a) Modified EDFM (b) Multi-branch method99

Figure 5.29: Variation of ΔCOP_L with fishbone lateral numbers. The X axis is shown in log scale.....101

Figure 5.30: Verification of porosity cutoff method for the isotropic case with 60 fishbone laterals103

Chapter 1: Introduction

1.1 RESERVOIR SIMULATION FOR FRACTURED RESERVOIRS

More than 60% of the proven oil reserves and more than 40% of the gas reserves are trapped in carbonate reservoirs¹. A vast majority of carbonate reservoirs are naturally fractured. Fractures are usually caused by mechanical failure induced by some geological processes such as folding, faulting, weathering, etc. (Fernø 2012). As “channels” for fluids, natural fractures bring high complexity as well as heterogeneity into reservoirs. Since the pattern of natural fractures is a reflection of the local state of stresses when the fractures initiated, the natural fractures usually show preferred orientations in a specific region, adding anisotropy to reservoir permeability. Furthermore, large numbers of highly connected natural fractures may enhance the effective reservoir permeability (Oda 1985). Therefore, some geological methods, such as seismic inversion (Far et al. 2013), are developed to accurately characterize the orientations and density of natural fractures.

In addition to naturally fractured reservoirs, recently much attention has been paid to hydraulically fractured reservoirs. The “shale revolution” has rejuvenated the oil and gas industry in the United States. The advanced technologies of horizontal drilling and multi-stage hydraulic fracturing gained a great success in economic development of unconventional oil and gas reservoirs. Large amounts of water, sand and chemicals are injected into reservoirs to break apart the rock and create hydraulic fractures. With the entire near-wellbore region stimulated, complex fracture networks may also be generated during the operation due to the pre-existing natural fractures (Fisher et al. 2004; Gale et al. 2007; Maxwell et al. 2002; Warpinski et al. 2009; Cipolla et al. 2010b; Cipolla et al. 2011b). Many geomechanics research studies have been conducted in fracture propagation

¹“Carbonate Reservoirs: Meeting unique challenges to maximize recovery”, Schlumberger, 2007

modeling to predict the geometry of the hydraulic fractures or the complex fracture networks (Olson 2008; Weng et al. 2011; Wu and Olson 2014; Wu and Olson 2015). In addition, fracture diagnostic tools, such as microseismic and distributed temperature sensing (DTS), also provide valuable information for fracture characterization and monitoring.

Fluid flow in fractured reservoirs is complicated. Fractures provide complex paths for fluid movement, and they introduce a direction of maximum and minimum permeability, which may ultimately impact the total recovery positively or negatively (Nelson 2001). Therefore, it is challenging to accurately predict the recovery from such reservoirs. Furthermore, the difficulty of making appropriate production schemes also increases in this type of reservoirs. The efficiency of a production scheme may highly depend on the fracture network connectivity, which is not easy to be directly measured (Lee et al. 1993). In addition, the high capillary contrast between fracture and matrix may cause differences in recovery performance between fractured reservoirs and non-fractured reservoirs. For water flooding processes in water-wet rocks, since the injected water has the tendency to flow in fracture networks, a high water saturation boundary is formed for matrix blocks (Lemonnier and Bourbiaux 2010); therefore, the water in fractures may spontaneously be imbibed into the rock to displace the oil in the opposition direction (Fernø 2012). Fractures may also cause early water breakthrough, leading to low sweep efficiency (Lemonnier and Bourbiaux 2010). Some enhanced oil recovery (EOR) methods may also face problems in fractured reservoirs as the injected chemical fluids may likely flow through the fractures and bypass the matrix (Manrique et al. 2007).

Since the presence of fractures plays such a significant role in production, it is important to accurately model the influence of fractures in reservoir simulation. Extensive work has been conducted to solve this problem analytically (Cinco-ley and Samaniego-v

1981; Zhou et al. 2014) and numerically (Warren and Root 1963; Karimi-Fard and Firoozabadi 2001; Hoteit and Firoozabadi 2004).

Dual porosity and dual permeability (DPDP) approaches (Warren and Root 1963; Blaskovich et al. 1983) were proposed to model naturally fractured reservoirs. Until now, they are still the most commonly used approaches in reservoir simulators. Due to the fact that for reservoirs with densely distributed and highly connected fractures, the overall flow may be dominated by the flow in fractures, in this approach, a fractured medium is divided into two continua, one with high flow capacity (fracture) and one with high storage capacity (matrix). The flow equations are effectively solved by coupling the two continua through a transfer function. DPDP approaches are very efficient in computation and have been successfully applied to many real field studies. However, due to the simplification in the models, they are only adequate for reservoirs with a large number of inter-connected small-scale fractures. Therefore, discrete fracture models (DFMs), both in finite-element method or in finite-difference method, have been developed to overcome such problems. Unstructured grids are utilized in most DFMs (Hoteit and Firoozabadi 2006; Hui et al. 2013; Karimi-Fard and Firoozabadi 2003) to explicitly model the fracture geometry and orientation. In these models, large numbers of small grids are created around the fractures, especially for intersecting fractures. DFMs are relatively accurate in the modeling of large-scale fractures and the details in fracture geometry can be appropriately represented. However, due to the complex gridding and high computational cost accompanying unstructured grids, the usage of DFMs in real field studies is still limited.

As a compromise, an embedded discrete fracture model (EDFM) was developed (Lee et al. 2001; Li and Lee 2008; Hajibeygi et al. 2011) to honor the accuracy of DFMs while keeping the efficiency offered by structured gridding. In this approach, the reservoir is discretized using Cartesian grids and additional cells are introduced for fractures. The

influences of fractures are explicitly modeled through transport indices between non-neighboring cells. Moinfar et al. (2014) extended the EDFM to 3D simulations and implemented the model in GPAS, a fully-implicit in-house compositional reservoir simulator developed at The University of Texas. Later, Shakiba (2014) implemented the EDFM in another compositional simulator (UTCOMP) and a chemical simulator (UTGEL). However, to study complex EOR processes in fractured reservoirs, such as polymer flooding, surfactant flooding, wettability alteration, four-phase flow, and steam injection, there is a requirement to implement the EDFM in another powerful in-house chemical EOR simulator, UTCHEM, which has the capability to handle the above processes. Furthermore, the EDFM is a general approach, and one important feature of it is the compatibility with existing reservoir simulators. In order to make the EDFM more powerful as well as more widely-used, there is a demand to develop a general procedure to apply the EDFM to other simulators (such as commercial simulators) in a non-intrusive way. With this procedure, the EDFM will be able to be combined with the original functionalities of these simulators and the range of problems the EDFM can solve will be greatly expanded.

1.2 OBJECTIVES OF THIS RESEARCH

Based on the problems described above, the objectives of this research are

1. Implement the EDFM approach in an in-house, IMPES-type, multi-component reservoir simulator, UTCHEM. Fracture cells in the EDFM need to be added in the computational domain. Also, the governing equations in UTCHEM need to be modified to allow for non-neighboring connections.

2. Apply the EDFM in commercial simulators using a non-intrusive way.
Hence, the EDFM will become a more general approach and it can be combined with the functionalities of commercial simulators.
3. Verify the accuracy, flexibility, applicability, and extensiveness of the EDFM through case studies in different production scenarios.

1.3 BRIEF DESCRIPTION OF CHAPTERS

In Chapter 2, we present a literature review of some proposed methods for fluid flow predictions in fractured reservoirs, including dual-continuum approaches, discrete fracture models, and analytical solutions. In Chapter 3, we first give a brief description of the UTCHEM reservoir simulator, then the methodology and formulations in the EDFM are discussed. Chapter 4 introduces the implementation methodology of the EDFM in UTCHEM and commercial reservoir simulators, followed by several case studies to verify the accuracy of the EDFM and its implementation. In Chapter 5, we present some example simulations of the modified UTCHEM and commercial simulators, showing the applications of EDFM in naturally and hydraulically fractured reservoirs. The modified EDFM formulations for modeling of a multilateral well stimulation technology will also be presented. Finally, in Chapter 6, we summarize this research and give the recommendations for future studies.

Chapter 2: Literature Review

Presence of fractures poses challenges for numerical simulations of hydrocarbon production from fractured media. The small pore volumes of fractures and the high permeability contrast between matrix and fracture create numerical problems in simulation. Furthermore, consideration of some special recovery mechanisms in fractured media creates more difficulties for accurate and efficient reservoir simulation. Several models were proposed and developed to simulate the fractured media, within which dual-continuum models and discrete fracture models are the most widely-used ones. Hence, in this chapter, we present an introduction of these two models. Also, several analytical solutions developed for fractured reservoirs will be discussed.

2.1 DUAL-CONTINUUM MODELS

The dual porosity approach was first proposed by Barenblatt et al. (1960). Warren and Root (1963) enhanced this approach and applied it in the interpretation of well test data. In this approach, the porous medium is envisioned as two continua: one contributes significantly to the pore volume but contributes little to the flow capacity (matrix); another one contributes significantly to the flow capacity but its contribution to the pore volume is negligible (fracture). Two sets of parameters are respectively defined for these two continua. Figure 2.1 shows the idealization of the fractured medium in dual porosity approach, where the fractures are uniformly spaced and parallel to one of the principal axes of permeability, and the matrix is homogeneous and isotropic. Since the matrix blocks are separated by fractures, no flow between matrix blocks can occur. The flow equations for pseudo-steady state, single-phase flow in dual porosity systems are

$$\frac{K_{fx}}{\mu} \frac{\partial^2 P_f}{\partial x^2} + \frac{K_{fy}}{\mu} \frac{\partial^2 P_f}{\partial y^2} - \phi_m c_m \frac{\partial P_m}{\partial t} = \phi_f c_f \frac{\partial P_f}{\partial t}, \quad (2.1)$$

$$\phi_m C_m \frac{\partial P_m}{\partial t} = \frac{\sigma K_m}{\mu} (P_f - P_m), \quad (2.2)$$

where K_{fx} is the fracture permeability in X direction, K_{fy} is the fracture permeability in Y direction, μ is fluid viscosity, P_f is pressure in fracture, P_m is pressure in matrix, ϕ_m is matrix porosity, ϕ_f is fracture porosity, c_f is fracture compressibility, c_m is matrix compressibility, t is time, and σ is shape factor. The shape factor controls the flow communications between matrix and fracture, and it is determined by the geometry of matrix blocks. Warren and Root (1963) derived the expression for the shape factor as

$$\sigma = \frac{4N(N+2)}{L^2}, \quad (2.3)$$

where N is the number of normal sets of fractures and L is the characteristic length of the block.

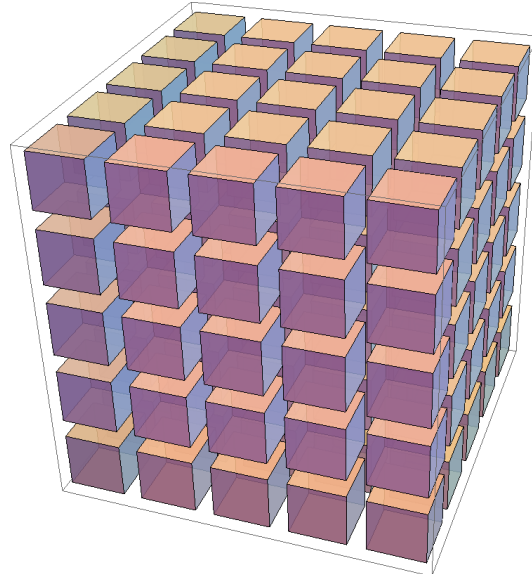


Figure 2.1: Reservoir idealization in dual porosity models.

Warren and Root (1963) found an analytical solution for Equations 2.1 and 2.2, and the solution was successfully applied in well test data analysis. Later, Kazemi (1969) developed the dual porosity model for radial systems. He reproduced the results of Warren and Root (1963) and concluded that their solution is only applicable for cases with large contrasts between matrix and fracture flow capacities. He also mentioned that at large times, a fractured reservoir behaves as an equivalent homogeneous reservoir.

In the idealization of the dual porosity model, several assumptions are made as mentioned before to simplify the reservoir flow. More than fifty years have passed since the model was proposed, and lots of efforts have been paid to improve the accuracy and applicability of the model.

In Warren and Root (1963)'s formulations, the fluid transfer term between fracture and matrix, which is also referred to as "transfer function", has the form of

$$T = \frac{\sigma K_m}{\mu} (P_f - P_m). \quad (2.4)$$

In this equation, only single phase flow is considered, and several recovery mechanisms such as gravity, diffusion, and capillarity are ignored. Major improvements of the model in later research include extending the model to multi-phase flow and combining different mechanisms in the transfer function.

Kazemi et al. (1976) extended the single-phase model of Warren and Root (1963) and developed a three-dimensional two-phase reservoir simulator for fractured media with the capability of modeling relative fluid mobilities, gravity effect, imbibition, and variable reservoir properties. The simulator was used to model the imbibition in oil-water systems. In their finite-difference formulations, the transfer function is

$$T_{s,\alpha} = \sigma \frac{K \cdot k_{ra}}{\mu_\alpha} (P_\alpha^m - P_\alpha^f), \quad (2.5)$$

where α refers to phase and σ has the expression of

$$\sigma = 4 \left(\frac{1}{L_x^2} + \frac{1}{L_y^2} + \frac{1}{L_z^2} \right), \quad (2.6)$$

where L_x , L_y , and L_z are the block dimensions in three directions.

In another two-phase simulator, Rossen (1977) modeled the fluid transfer between matrix and fracture in a dual porosity model where matrix blocks were treated as sink or source terms, thus a conventional simulator could be used to model the fracture system. These source and sink terms were handled semi-implicitly in his simulation. As a result, the stability of the simulator was improved.

For three-phase simulations, Thomas et al. (1983) developed a three-dimensional dual porosity reservoir simulator to handle the flow of water, oil, and gas in naturally fractured reservoirs. They included the capillary pressure, gravity, and viscous forces in the transfer function. Pseudo-relative permeability and pseudo-capillary pressure curves were used in their model with the vertical equilibrium assumption.

Reiss (1980) was the first one to discuss the influence of gravity on matrix-fracture transfer function. To the gravity term, additional attention needs to be paid in the simulation because it is affected by the direction of the flow. Gilman and Kazemi (1983) used different depths for matrix and fracture to account for the gravity force. Litvak (1985) improved this method by introducing a time-dependent gravity term. Vertical equilibrium was assumed in both media. Coats et al. (1971) considered the gravity effects through a pseudo-capillary pressure in order that no explicit gravity term needs to be added into the flow equations. This approach was also used by Rossen and Shen (1989), where the authors showed that it reaches a balance between accuracy and computational cost.

Another limitation in the original transfer function formulation is the pseudo-steady state assumption. This assumption may underestimate the early time recovery and

mismatch the final recovery for some special systems such as gravity drainage systems (Abushaikha and Gosselin 2008). Much work has been done to overcome this obstacle. Beckner et al. (1988) developed a dynamic dual porosity formulation to model transverse imbibition. In their formulation, the mass transfer between matrix and fracture is related to the “effective exposure time” of the matrix blocks to fracture water. Experimental data was used in their model verification and they claimed that to get a better match between dual porosity simulation and experimental results, an increase in shape factor is required with increasing water injection rate. Chang (1993) derived a time-dependent shape factor for one-dimensional case but his formulation is too complicated to be implemented in simulators. Lim and Aziz (1995) derived an expression of single-phase flow shape factor using an analytical solution to eliminate the pseudo-steady state assumption and the results were verified with fine-grid single-porosity simulations. For general cases, as pointed out by some authors (Lemonnier and Bourbiaux 2010), it is difficult to derive a transfer function that is only time-dependent and valid through all stages of the field exploitation.

In most dual porosity models, “lumped parameters” are given to matrix and fracture blocks by taking averages of the properties over the block volume. With large rates of pressure drop and large block sizes, the pseudo-steady state assumption (where it is appropriate to represent the blocks with lumped parameters) in dual porosity models may introduce large errors compared to transient formulation (Saidi 1983). The case is even worse when “lumped parameters” are used in the simulation of gravity drainage and imbibition processes (Saidi 1983). Saidi (1983) proposed a method to improve the accuracy of dual porosity models in the above cases using subgridding techniques. In his model, with gridded matrix blocks in both radial and vertical directions, the exchange between fracture and matrix was calculated more accurately, and better accuracy could be obtained for simulation of gravity drainage and diffusion processes.

Besides, a “Multiple Interacting Continua” (MINC) method (Pruess and Narasimhan 1982; Pruess and Narasimhan 1985; Wu and Pruess 1988) was proposed as another subgridding technique to study fluid and heat flow in fractured porous media. For multi-phase and non-isothermal flow, the transient period of matrix-fracture flow may be very long. By assuming that the changes in thermodynamics conditions of a matrix block are controlled by the distance between the block and the nearest fractures, a series of “nested” control volumes are created in MINC method as shown in Figure 2.2. Using this method, the flow between matrix and fracture are treated as one-dimensional (for two-dimensional fractured media) and the number of extra cells introduced by subgridding can be effectively reduced compared to explicit discretization.

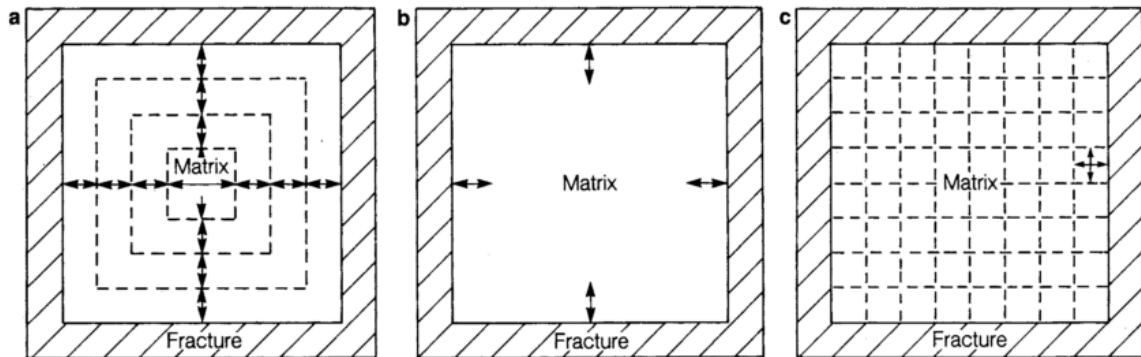


Figure 2.2: Discretization of matrix blocks (a) MINC (b) dual porosity (c) explicit discretization (Wu and Pruess 1988).

The MINC method was successfully applied to model the water/oil flow during the imbibition processes by Wu and Pruess (1988). They claimed that the traditional dual porosity model may result in large computational errors, especially for large block sizes and low reservoir permeability, while the MINC method could obtain accurate results in

these cases. In addition, the increase in computational time of the MINC was modest compared to traditional dual porosity model.

The MINC method was later applied in three-dimensional simulations (Chen et al. 1987; Gilman 1986) where matrix blocks are subdivided in both horizontal and vertical directions, in order that the gravity effect and phase segregation can be precisely modeled.

Attention has also been paid to matrix-matrix connection in order to improve the accuracy of the dual porosity model. In traditional dual porosity models, the flow between matrix blocks is ignored. An extended model, known as dual permeability model, was proposed to account for the flow between matrix blocks (Blaskovich et al. 1983; Hill and Thomas 1985). Figure 2.3 shows a comparison of the connections in dual porosity and dual permeability models, where an extra type of matrix/matrix connection is added in the latter model. Studies showed that the dual permeability model may predict higher waterflood recoveries than and similar primary recoveries as the dual porosity model, with a much higher computational cost and higher memory requirement (Dean and Lo 1988).

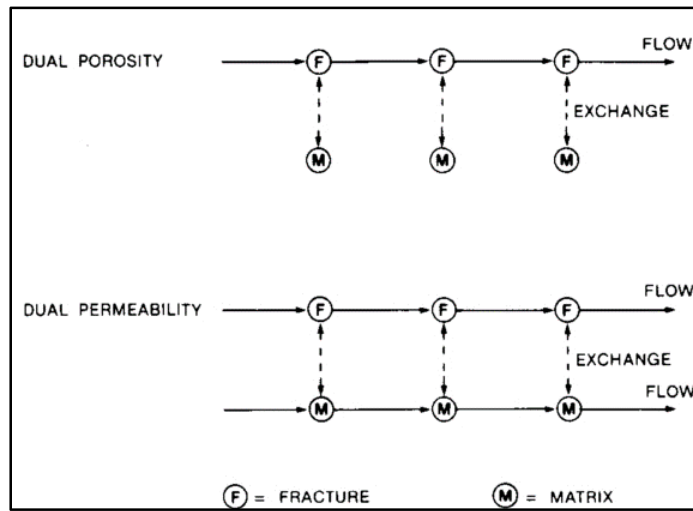


Figure 2.3: Comparison of the connections in dual porosity and dual permeability models (Dean and Lo 1988).

2.2 DISCRETE FRACTURE MODELS

The dual porosity/dual permeability models are effective ways to model naturally fractured reservoirs. However, there are some limitations in these models. First, they are not appropriate for modeling of disconnected fractures and a small number of large-scale fractures (Karimi-Fard and Firoozabadi 2003; Karimi-Fard et al. 2004). Then, they may have difficulties representing highly localized anisotropy in reservoirs (Moinfar et al. 2013a). Also, it is not easy to accurately evaluate the transfer function between matrix and fracture, especially when gravity and viscous effects exist (Karimi-Fard et al. 2004; Monteagudo and Firoozabadi 2004). To overcome these limitations, discrete fracture models, where each fracture is explicitly represented by an element or a control volume, were developed to obtain more realistic representation of fractures. In discrete fracture models, each fracture is assigned a size, an orientation, and a permeability. These parameters could be obtained from fracture diagnosis monitoring or geomechanics modeling of fracture propagation, or they could be generated using stochastic methods.

A direct way to represent the discrete fractures is to put high permeability cells in the corresponding locations. For orthogonal fractures or orthogonal fracture networks, a structured grid could be used (Cipolla et al. 2010a; Frantz et al. 2005; Cipolla et al. 2011a) with very fine grid size near fractures or local grid refinement. However, for fractures with arbitrary orientations, and for complex fracture intersections, an unstructured grid may be required in most discrete fracture models (Karimi-Fard et al. 2004; Cipolla et al. 2011a) to accurately represent the fractures. Cipolla et al. (2011a) summarized the gridding approaches associated with discrete fracture models. Since the usage of structured grids is fairly straightforward, we concentrate on discrete fracture models using unstructured grids.

As an early attempt, Noorishad and Mehran (1982) and Baca et al. (1984) developed a discrete fracture model for two-dimensional single-phase flow. In their finite-

element method, the fracture was treated as a two-nodal point transport element. Juanes et al. (2002) generalized the usage of discrete fracture models in finite element methods for two-dimensional and three-dimensional single-phase simulations.

Kim and Deo (2000) and Karimi-Fard and Firoozabadi (2003) extended the finite-element discrete fracture models to the simulation of oil-water two-phase flow. Triangular elements and line elements were used in their models for matrix and fracture, respectively. They claimed that the high contrast between length scales of matrix and fracture makes the traditional single porosity method very computationally inefficient, while the discrete fracture models do not suffer from this limitation.

Hoteit and Firoozabadi (2006) combined the mixed-finite-element (MFE) method with discontinuous Galerkin (DG) method for numerical simulation in two-dimensional fractured media. The MFE was used to solve the pressure equation and the DG was used to approximate the species-balance equations. The computational problem associated with multi-intersecting fractures was also overcome through the usage of MFE.

Bastian et al. (2000) applied the discrete fracture model in a control-volume method, where finite-volume formulations were used over dual cells (Monteagudo and Firoozabadi 2004). The advantages of this method are that it maintains a local mass conservation and it has a clear upwind criterion. In their work, Bastian et al. (2000) included the gravity term but they ignored the capillary term. The capillary effects in control-volume method based discrete fracture model were first discussed by Monteagudo and Firoozabadi (2004) in their study of two-phase immiscible flow.

Fu et al. (2005) developed a control-volume finite-element (CVFE) method for three-dimensional three-phase reservoir simulation with discrete fractures. The fractures were represented by lines and planes in two-dimensional and three-dimensional problems, respectively. The authors claimed that the CVFE has similar numerical complexity as

finite-difference scheme; moreover, the obtained solution is locally mass conservative. Similar approaches were also used by some other researchers (Matthai et al. 2005).

Karimi-Fard et al. (2004) presented a discrete fracture model suitable for simulators that work with connectivity list. In their unstructured control-volume finite-difference technique, orthogonal or near orthogonal grids were created, with an isotropic permeability field; therefore, a two-point flux approximation (TPFA) scheme could be applied. With a hierarchical representation of the object geometries, the fractures were represented by segments in two-dimensional problems (as shown in Figure 2.4) and by polygons in three-dimensional problems. Similar approaches were used by other authors (Sandve et al. 2012; Hui et al. 2013; Jiang and Younis 2015). Sandve et al. (2012) applied a multi-point flux approximation (MPFA) scheme to study reservoirs with anisotropic permeability. The authors claimed that for anisotropic porous media, MPFA has a great advantage over TPFA.

Matthai et al. (2007) developed a hybrid finite-element/finite-volume method using hybrid-element meshes. For three-dimensional simulations, they represented matrix cells with tetrahedra, hexahedra, pyramids, or prism elements and used lower-dimensional elements for fractures, such as triangles and quadrilaterals. For each element type, generalized node-centered finite-difference stencils were constructed. The usage of hybrid elements could reduce the number of nodes, resulting in low computational cost. Similar methods were also used by Paluszny et al. (2007) and Geiger et al. (2009).

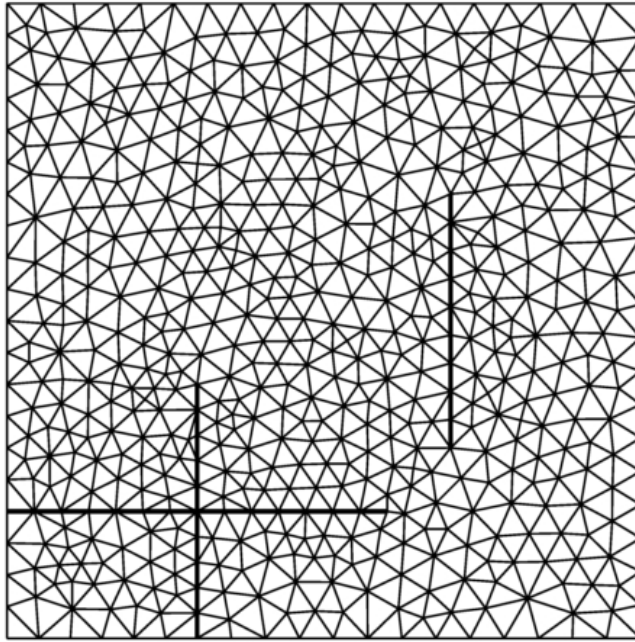


Figure 2.4: Unstructured discretization of the fractured media using Delaunay triangulation (Karimi-Fard et al. 2004).

In discrete fracture models, when two fractures intersect each other, a small control volume or small element will be created at the intersection node, which may cause problems in preconditioning and limit the simulation time step to an unreasonable value. Efforts have been made to properly solve this problem. Karimi-Fard et al. (2004) eliminated the intersection nodes using a “star-delta” transformation, which also allows for multi-fracture intersection. The authors mentioned that this transformation is exact only for single phase incompressible flow. The effectiveness of this method to increase the time step was later confirmed by Sandve et al. (2012). Another method is to “borrow” volume from neighboring fracture blocks (Li et al. 2015), which could also effectively reduce the computational time with a small computational error.

The usage of unstructured grids in discrete fracture models provides the flexibility to model more realistic fracture geometries; however, on the other hand, the difficulty in

mesh generation makes discrete fracture models hard to be implemented in simulators and the high computational burden may hinder its applications in field studies. Owing to the recent development in linear solvers and parallel computing, the discrete fracture models based on unstructured grids have gained extensive development and some models have been used in commercial simulators (an example is shown in Figure 2.5). Nevertheless, there are still numerous technical challenges to be solved, including automated unstructured gridding, efficient representation of fracture intersection, and overlap of fracture networks (Cipolla et al. 2011a). Therefore, there is a still a demand for improvement in discrete fracture models. The embedded discrete fracture model (EDFM), proposed by Li and Lee (2008), is an efficient approach to solve the problems in unstructured gridding, and it will be discussed in details in Chapter 3.

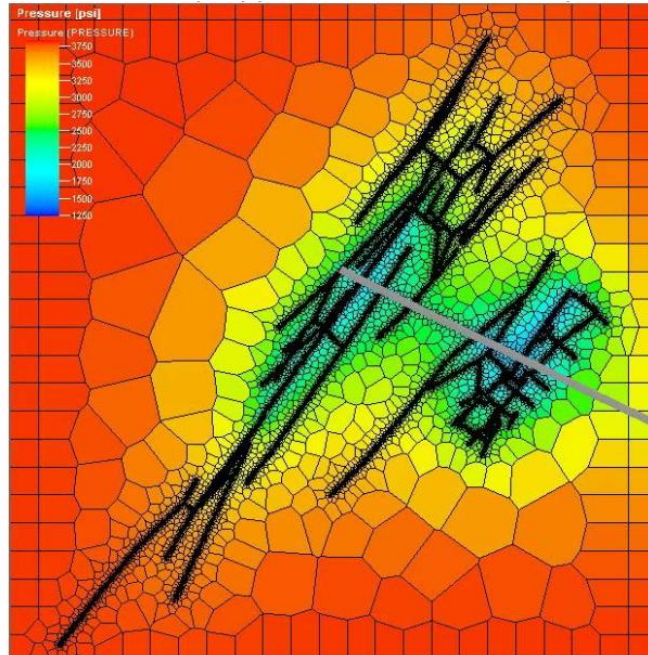


Figure 2.5: Pressure distribution predicted by a discrete fracture model using unstructured grids (Cipolla et al. 2011a). The model has been implemented in a commercial simulator.

2.3 ANALYTICAL SOLUTIONS

Analytical solutions have been developed for decades in petroleum industry. Often they are limited to specific problems with a lot of simplifications and high idealization, such as single-phase flow, regular reservoir shape, etc. However, they form the basis of pressure and rate transient analysis. In addition, analytical solutions are very useful in the verification of numerical models.

For hydraulically fractured reservoirs, there are many analytical solutions derived for single planar fractures (Gringarten et al. 1974; Cinco-Ley et al. 1978; Cinco-Ley and Samaniego-V. 1981) using Green function or other mathematical approaches. In Cinco-Ley and Samaniego-V. (1981)'s very important work, they analyzed the pressure transient behavior of a vertically fractured well, and divided the flow into four periods: fracture linear flow, bilinear flow, formation linear flow, and pseudo-radial flow. This is the basis of many later works in pressure transient analysis of fractured reservoirs.

In unconventional reservoir development, most horizontal wells are multi-fractured. Raghavan et al. (1997) derived a mathematical solution for multi-fractured horizontal wells with finite-conductivity fractures. Using their solution, they evaluated the influence of fracture length, conductivity, location, and orientation on ultimate recovery. Chen and Raghavan (1997) developed an analytical solution for a multi-fractured horizontal well in a rectangular reservoir. Later, using Fourier analysis, Wan and Aziz (2002) developed a semi-analytical solution to predict correct well index for multi-fractured horizontal wells. In their solution, the fractures could be rotated at any horizontal angle and they may not necessarily fully penetrate the formulation vertically.

Most analytical solutions could not consider complex fracture geometries and variable fracture properties along the length. As an important extension, Zhou et al. (2014) presented a semi-analytical solution combining a point-source solution with a numerical

solution for single-phase production analysis of complex fracture networks (shown in Figure 2.6). In their solution, the non-Darcy flow in fractures could be modeled and different fractures could have different properties. The different flow regimes for a fracture network could be conveniently analyzed using this solution. Yu et al. (2014) added the gas adsorption mechanism into this model and extended this work to shale gas reservoirs. Yu et al. (2015) further extended Zhou et al. (2014)'s model to consider non-planar fracture shape and variable fracture aperture along the length. The stress dependency of fracture aperture was also included in the model.

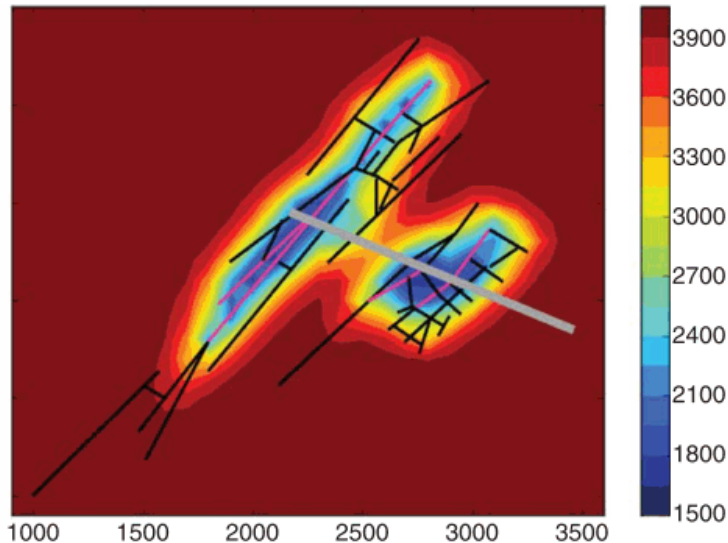


Figure 2.6: Pressure distribution of a complex fracture network predicted by semi-analytical solution (Zhou et al. 2014).

Chapter 3: Overview of UTCHEM Reservoir Simulator and the Embedded Discrete Fracture Model (EDFM)

The Embedded Discrete Fracture Model (EDFM) was developed to simulate fractured reservoirs as well as to take advantage of the original functionalities of the reservoir simulators. It extends the formulations in reservoir simulators through non-neighboring connections (NNCs) to model fractured media with structured grids. In this work, the EDFM is implemented into UTCHEM, an in-house reservoir simulator developed at The University of Texas. For the first part of this chapter, we give a brief introduction of the UTCHEM reservoir simulator, including its basic functionalities and the governing equations. Then, we introduce the methodology of the EDFM and related equations for transport indices calculations. The preprocessor developed for the EDFM will also be described.

3.1 UTCHEM RESERVOIR SIMULATOR

UTCHEM is a multi-phase, multi-component reservoir simulator. It was originally developed in 1978 (Pope and Nelson 1978) to model the enhanced oil recovery (EOR) processes using surfactant and polymer. Now, it has been greatly extended to simulate different processes. It has the capability of modeling complex phase behaviors, various chemical EOR mechanisms, and geochemical reaction processes. In this section, we introduce some features and the governing equations of UTCHEM. For more detailed description of the formulations and features in UTCHEM, the reader is referred to *UTCHEM Technical Documentation (2011)*.

3.1.1 Features of UTCHEM

UTCHEM allows for multi-phase, multi-component reservoir simulation. In this simulator, the user can specify any number of chemical components, including water, surfactant, polymer, alcohols, calcium, chloride, microbiological species, etc. These components can form four phases: water, oil, microemulsion, and gas. Complex phase behaviors are modeled in UTCHEM for EOR processes.

Some main features of UTCHEM are summarized below:

- Cartesian, corner point, radial, and curvilinear grid
- Variable temperature
- Heterogeneous permeability and porosity
- Vertical and horizontal well
- Dual porosity model
- Wettability alteration and water hysteretic capillary pressure
- Full tensor dispersion and molecular diffusion
- Non-equilibrium dissolution of organic components from a non-aqueous phase into aqueous or microemulsion phase
- Surfactant model
- Polymer with non-Newtonian rheology
- Steam and electrical heating models

The simulator uses a block-centered finite-difference scheme to solve the flow equations. An IMPES-type formulation is applied, which means solving the pressure equation implicitly and solving the concentration equation explicitly. In the following sections, we introduce the governing equations in UTCHEM.

3.1.2 Governing Equations

In UTCHEM, there are mainly three governing equations: the mass conservation equation for species, the pressure equation for aqueous phase, and the energy conservation equation. The equations allow for rock and fluid compressibility, chemical reaction, physical dispersion, and molecular diffusion in the simulation.

3.1.2.1 Mass Conservation Equation

The mass conservation equation is expressed in terms of the overall volume of the components as

$$\frac{\partial}{\partial t} \left(\phi \tilde{C}_k \rho_k \right) + \vec{\nabla} \cdot \left[\sum_{l=1}^{n_p} \rho_k \left(C_{kl} \vec{u}_l - \vec{D}_{kl} \right) \right] = R_k , \quad (3.1)$$

where

$$\tilde{C}_k = \left(1 - \sum_{k=1}^{n_c} \hat{C}_k \right) \sum_{l=1}^{n_p} S_l C_{kl} + \hat{C}_k , \quad k = 1, 2, \dots, n_c . \quad (3.2)$$

In the above equations,

\tilde{C}_k = overall (sum over all phases) volume of component k per unit pore volume

t = time

ϕ = porosity

n_p = number of phases

$\rho_k = \rho_{P_R, k} / \rho_{P_{R0}, k}$

$\rho_{P_R, k}$ = density of pure component k at a reference phase pressure P_R

$\rho_{P_{R0}, k}$ = density of pure component k at a reference pressure P_{R0} , usually $P_{R0} = 1 \text{ atm}$

C_{kl} = concentration of species k in phase l

\vec{u}_l = flux of phase l

\vec{D}_{kl} = dispersive flux of species k in phase l

R_k = Source term of species k

S_l = saturation of phase l

\hat{C}_k = adsorbed concentration of species k

n_{cv} = total number of volume-occupying species (including water, oil, surfactant, and air)

3.1.2.2 Pressure Equation

The pressure equation in UTCHEM is derived by combining the Darcy's law, the definition of capillary pressure, the constitutive relations, and the sum of mass conservation equations over the volume-occupying components. The differential form of the pressure equation is

$$\varphi c_t \frac{\partial P_1}{\partial t} - \vec{\nabla} \cdot \vec{\vec{K}} \cdot \lambda_{rTc} \vec{\nabla} P_1 = -\vec{\nabla} \cdot \sum_{l=1}^{n_p} \vec{\vec{K}} \cdot \lambda_{rlc} \gamma_l \vec{\nabla} h + \vec{\nabla} \cdot \sum_{l=1}^{n_p} \vec{\vec{K}} \cdot \lambda_{rlc} \vec{\nabla} P_{cl1} + \sum_{k=1}^{n_{cv}} Q_k , \quad (3.3)$$

where

$$\lambda_{rlc} = \frac{k_{rl}}{\mu_l} \sum_{k=1}^{n_{cv}} \rho_k C_{kl} , \quad (3.4)$$

$$\lambda_{rTc} = \sum_{l=1}^{n_p} \lambda_{rlc} , \quad (3.5)$$

and

$$c_t = c_r + \sum_{k=1}^{n_{cv}} c_k^0 \tilde{C}_k , \quad (3.6)$$

In the above equations,

P_1 = pressure of phase 1 (water)

c_t = total compressibility

$\vec{\vec{K}}$ = reservoir permeability tensor

λ_{rTc} = total relative mobility over all phases

λ_{rlc} = relative mobility of phase l with correction for fluid compressibility

γ_l = specific gravity of phase l

h = depth

P_{cll} = capillary pressure between phase l and water

Q_k = source/sink term for species k

k_{rl} = relative permeability of phase l

μ_l = viscosity of phase l

c_r = rock compressibility

3.1.2.3 Energy Conservation Equation

The energy conservation equation is derived by considering the advection and heat conduction term as

$$\frac{\partial}{\partial t} \left[(1-\phi)\rho_s C_{vs} + \phi \sum_{l=1}^{n_p} \rho_l S_l C_{vl} \right] T + \vec{\nabla} \cdot \left(\sum_{l=1}^{n_p} \rho_l C_{pl} u_l T - \lambda_T \vec{\nabla} T \right) = q_H - Q_L, \quad (3.7)$$

where

T = reservoir temperature

C_{vs} = soil heat capacity at constant volume

C_{vl} = heat capacity of phase l at constant volume

C_{pl} = heat capacity of phase l at constant pressure

λ_T = thermal conductivity

q_H = enthalpy source term per bulk volume

Q_L = heat loss to overburden and underburden formations or soil

ρ_l = density of phase l

S_l = saturation of phase l

3.1.2.4 Constitutive Relations

In addition to the above equations, there are some constitutive relations used in UTCHEM as

$$\sum_{l=1}^{n_p} S_l = 1, \quad (3.8)$$

$$\sum_{k=1}^{n_c} C_{kl} = 1. \quad (3.9)$$

These relations are implicitly contained in the derivations of the governing equations.

3.2 EMBEDDED DISCRETE FRACTURE MODEL (EDFM)

The EDFM was first developed by Li and Lee (2008) to honor the accuracy of discrete fracture models (DFMs) while keeping the efficiency offered by structured gridding. In this approach, the reservoir is discretized using Cartesian grids and additional cells are introduced for fractures. The influence of fractures on fluid flow is explicitly modeled through transport indices between non-neighboring cells. In this section, we briefly introduce the development of the EDFM and discuss the methodology in the model.

3.2.1 Development of the EDFM

The presence of highly-conductive fractures can significantly impact the flow behaviors in reservoirs. Therefore, it has been a significant issue to model fractures in reservoir simulators accurately and efficiently. Dual-continuum approaches are often used to model naturally fractured reservoirs. Nevertheless, as mentioned in Chapter 2, they are not adequate for modeling large-scale fractures or capturing the influence of fracture connectivity (Karimi-Fard et al. 2004; Moinfar et al. 2013a). This leads to the development of discrete fracture models where fractures are modeled explicitly. However, the usage of

unstructured grids in many DFMs has limited their applications due to the high complexity in gridding and high computational cost. The EDFM was proposed as a tradeoff between the computational performance of dual-continuum models and the accuracy of DFMs.

As an early attempt, Lee et al. (2001) proposed a hierarchical approach to model fractures with different length scales (compared to the gridblock size) using different methods. In their approach, short fractures are upscaled by calculating Oda's permeability tensor and medium fractures are simulated using a combination of Green function and boundary element method. For long fractures, in analogy with the concept of well index, they defined a transport index to describe the flow between a gridblock and the part of fracture in that gridblock.

Later, Li and Lee (2008) extended the methodology of long fracture modeling to model fractures as 2D planes, include fracture networks, and allow for fracture-wellbore intersection. Since in this model, the fractures are cut into segments by matrix cell boundaries, and the fracture cells are “embedded” into the structured matrix cells, it is called the embedded discrete fracture model (EDFM). The formula for transport index calculation between matrix and a fracture segment was proposed by defining an average normal distance between the fracture plane and the matrix gridblock. The intersection between a vertical fracture and a vertical wellbore was also considered by superposing the productivities from the fracture and the wellbore. They showed several examples with two-dimensional reservoirs and vertical fractures to confirm the capability of the EDFM.

Later, in order to apply the EDFM to more realistic scenarios, Moinfar et al. (2014) further developed the EDFM for three-dimensional problems to include inclined fractures. They systematically proposed three types of non-neighboring connections in the EDFM and later added another type of connection between fracture and wellbore (Moinfar et al. 2013c). They implemented the EDFM in an in-house fully-implicit compositional reservoir

simulator (GPAS) and conducted several case studies including primary depletion and water flooding in naturally fractured and hydraulically fractured reservoirs. The dynamic behaviors of fractures were also considered by coupling geomechanics and flow simulation in the EDFM using a correlation between fracture aperture and effective normal stress (Moinfar et al. 2013b).

Recently, more attention has been paid to the EDFM due to its accuracy and flexibility. Shakiba (2014) implemented the EDFM in two in-house reservoir simulators (UTCOMP and UTGEL) to show the applicability of the EDFM in different simulators and verify the accuracy against a semi-analytical model. Cavalcante Filho et al. (2015) developed a preprocessing code for the EDFM for transport indices calculations. They also include the Oda's permeability tensor calculation, partial fracture intersections, and porosity-cutoff method in the preprocessor. Shakiba and Sepehrnoori (2015) combined the EDFM with microseismic monitoring data for complex fracture network characterization. Panfili et al. (2014) applied the EDFM to a commercial simulator and performed case studies of miscible gas injection in fractured carbonate reservoirs using corner point geometry grids. Jiang et. al (2014) integrated the EDFM with dual-continuum approaches and MINC (multiple interacting continua) method to model the fracture networks in shale gas reservoirs and they showed that the hybrid model can reduce the computational cost as well as handle the extreme conductivity contrast between small-scale fractures and tight matrix.

Owing to the great success it has gained during the last several years, the EDFM has become a promising approach in DFMs. In next section, we will describe the discretization and connections in the EDFM in details.

3.2.2 Methodology Description

The EDFM borrows the concept from dual-continuum approaches that create fracture cells in contact with corresponding matrix cells to account for the mass transfer between continua. Once a fracture penetrates a matrix cell, an additional cell is created to represent the fracture segment in the physical domain. Each individual fracture could be discretized into several fracture segments by the matrix cell boundaries. To differentiate the newly added cells from the original matrix cells, these additional cells are called fracture cells.

In Figure 3.1, we illustrate the procedure to add fracture cells in the EDFM using a simple case with only 3 matrix blocks and 2 fractures. Figure 3.1a shows the physical domain and Figure 3.1b shows the computational domain. Each matrix block and fracture segment in the physical domain is represented by a cell in the computational domain with the same color. Before adding the fractures, we have 3 matrix cells: cell 1, cell 2, and cell 3. After adding the fractures, the total number of cells increases. Fracture 1 penetrates all three matrix blocks, hence three fracture cells (cells 4, 5, and 6) are introduced into the computational domain to represent the corresponding fracture segments. Similarly, only one extra cell (cell 7) is added for Fracture 2 since it only penetrates one matrix block. Because we use structured grid, every row should have the same number of cells, therefore 2 null cells are also introduced. Finally, the total number of cells increases from 3 ($1 \times 3 = 3$) to 9 ($3 \times 3 = 9$). The depth of each fracture cell is defined as the depth of the centroid of the corresponding fracture segment and the pore volume is defined as the volume of the fracture segment

$$V_f = S_{seg} w_f , \quad (3.10)$$

where S_{seg} is the area of the fracture segment perpendicular to the fracture aperture and w_f is the fracture aperture. In the simulator, we calculate the pore volumes of the fracture segments by assigning an effective porosity for each fracture cell

$$\phi_f = \frac{S_{seg} w_f}{V_b}, \quad (3.11)$$

where V_b is the bulk volume of the cell assigned to the fracture segment.

After adding cells to represent fracture segments, non-neighboring connections (NNCs) are subsequently defined. The aim for introducing NNCs is to allow flow communication between cells that are physically connected but not neighboring in computational domain. Three types of NNCs are defined as follows:

- NNC type I: connection between a fracture segment and the matrix cell it penetrates
- NNC type II: connection between fracture segments in an individual fracture
- NNC type III: connection between intersecting fracture segments

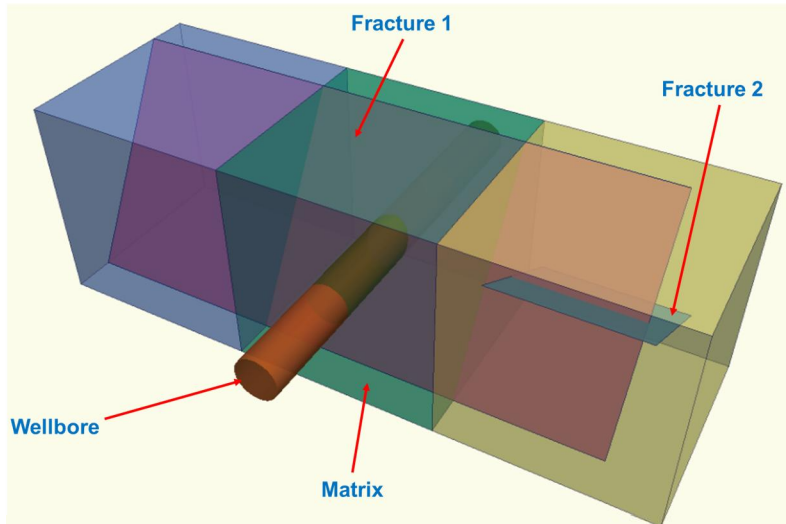
All three types of NNCs are shown by arrows in Figure 3.1b. The cells in each NNC pair are connected by transmissibility factors calculated by our preprocessor. Using these transmissibility factors, the volume flow rate of phase l between two cells in a NNC pair is

$$q = \lambda_l T_{NNC} \Delta P, \quad (3.12)$$

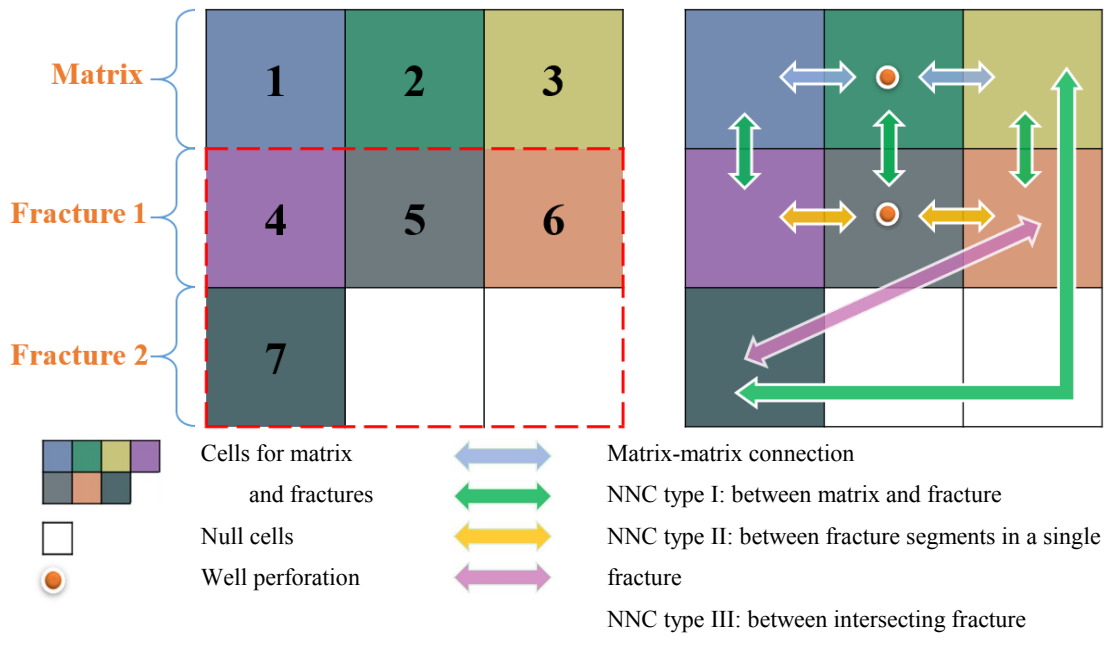
where λ_l is the relative mobility of phase l , T_{NNC} is the NNC transmissibility factor, ΔP is the potential difference between the cells. Generally, T_{NNC} can be expressed as

$$T_{NNC} = \frac{k_{NNC} A_{NNC}}{d_{NNC}}, \quad (3.13)$$

where k_{NNC} , A_{NNC} , and d_{NNC} are the permeability, contact area, and distance associated with this connection, respectively.



(a) Physical domain



(b) Computational domain

Figure 3.1: Explanation of EDFM. In (a) we show a Case with 3 matrix blocks, 2 fractures, and a wellbore in physical domain. In (b) we show the corresponding cells in computational domain and the arrows show different types of connections.

In addition to these NNCs, the connections between fractures and wells are also introduced by the EDFM. When a fracture segment intersects the wellbore trajectory (as shown in Figure 3.1a), we define the corresponding fracture cell as a wellblock by adding a well perforation for this cell as shown in Figure 3.1b. A fracture well index is subsequently defined for this cell.

The formulations of T_{NNC} for different types of NNCs and the equation for fracture well index will be discussed in next section.

3.2.3 Calculation of the NNC Transmissibility Factors and Fracture Well Index

This section presents a brief review of the formulations to calculate the connection factors. The assumptions and limitations are also discussed.

3.2.3.1 Matrix-Fracture Connection

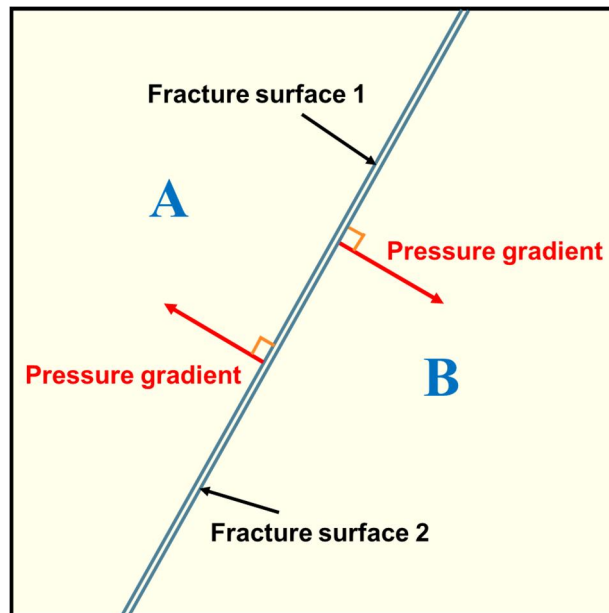


Figure 3.2: Illustration of the connection between matrix cell and fracture segment.

The NNC transmissibility factor between matrix and fracture segment depends on the matrix permeability and fracture geometry. When a fracture segment fully penetrates a matrix cell, if we assume a uniform pressure gradient in the matrix cell and that the pressure gradient is normal to the fracture plane as shown in Figure 3.2, the matrix-fracture transmissibility factor is

$$T_{f-m} = \frac{2A_f(\vec{\bar{K}} \cdot \vec{n}) \cdot \vec{n}}{d_{f-m}}, \quad (3.14)$$

where A_f is the area of the fracture segment on one side, $\vec{\bar{K}}$ is the matrix permeability tensor, \vec{n} is the normal vector of the fracture plane, and d_{f-m} is the average normal distance from matrix to fracture, which is calculated as

$$d_{f-m} = \frac{\int x_n dV}{V}, \quad (3.15)$$

where V is the volume of the matrix cell, dV is the volume element of matrix, and x_n is the distance from the volume element to the fracture plane.

If the fracture does not fully penetrate the matrix cell, the calculation of the transmissibility factor is complex since the pressure distribution in the matrix cell may deviate from the previous assumptions. In order to make the method non-intrusive, the same assumption as that of Li and Lee (2008) is made that the transmissibility factor is proportional to the area of the fracture segment inside the matrix cell.

3.2.3.2 Connection between Fracture Segments in an Individual Fracture

In the EDFM, a fracture can be discretized into many segments with different shapes, including triangle, quadrilateral, pentagon, and hexagon. An example is shown in Figure 3.3. Thus the connections between these segments are similar to those in 2D

unstructured grids. A simplified approximation similar to Karimi-Fard et al. (2004) is made in the EDFM. In this approximation, the transmissibility factor between a pair of neighboring segments 1 and 2 is evaluated using a two-point flux approximation scheme as

$$T_{seg} = \frac{T_1 T_2}{T_1 + T_2},$$

$$T_1 = \frac{k_f A_c}{d_{seg1}}, T_2 = \frac{k_f A_c}{d_{seg2}}, \quad (3.16)$$

where k_f is the fracture permeability, A_c is the area of the common face for these two segments, and d_{seg1} and d_{seg2} are the distances from the centroids of segments 1 and 2 to the common face, respectively. This two-point flux approximation scheme may lose some accuracy for 3D cases where the fracture segments may not form orthogonal grids. When the flow in the fracture plane becomes vital for the total flow, a multi-point flux approximation scheme may be required.

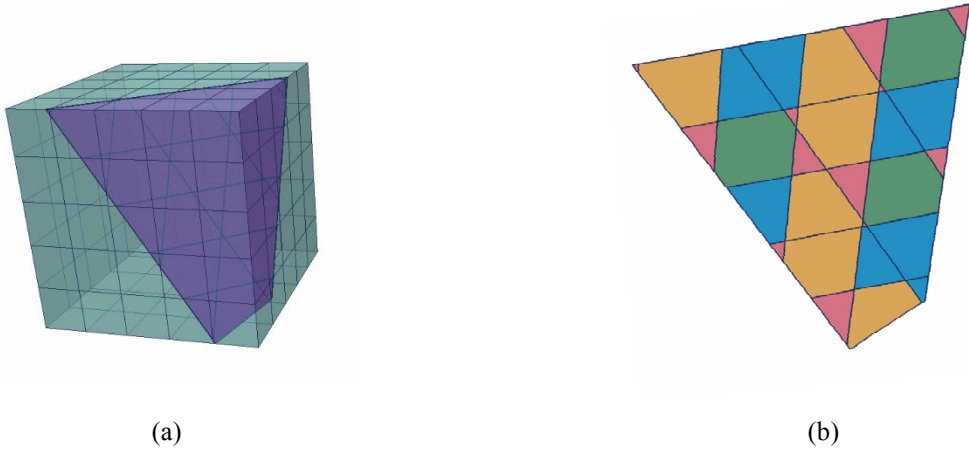


Figure 3.3: An example of different shapes of fracture segments in an individual fracture. The fracture is cut into 29 segments by the cell boundaries shown in (a). In (b), the segments are colored based on number of vertices. They can be triangle, quadrilateral, pentagon, or hexagon.

3.2.3.3 Fracture Intersection

Accurate and efficient modeling of fracture intersection is a challenging problem for discrete fracture modeling. The complexity of flow behavior at the fracture intersection makes it difficult to be modeled accurately. Moinfar et al. (2014) simplified this problem by assigning a transmissibility factor between intersecting fracture segments to approximate the mass transfer at the fracture intersection. The transmissibility factor is calculated as

$$\begin{aligned} T_{int} &= \frac{T_1 T_2}{T_1 + T_2}, \\ T_1 &= \frac{k_{f1} w_{f1} L_{int}}{d_{f1}}, T_2 = \frac{k_{f2} w_{f2} L_{int}}{d_{f2}}, \end{aligned} \quad (3.17)$$

where L_{int} is the length of the intersection line, and d_{f1} and d_{f2} are the weighted-average of the normal distances from the centroids of the subsegments (on both sides) to the intersection line. In Figure 3.4,

$$\begin{aligned} d_{f1} &= \int_{S_1} x_n dS_1 + \int_{S_3} x_n dS_3, \\ d_{f2} &= \int_{S_2} x_n dS_2 + \int_{S_4} x_n dS_4, \end{aligned} \quad (3.18)$$

where dS_i is the area element and S_i is the area of the fracture subsegment i . x_n is the distance from the area element to the intersection line. It is not necessary to perform integrations for the average normal distance. Since the subsegments are always polygon, geometrical method can be used to speed up the calculation.

The limitation of this fracture intersection model is that it cannot consider the complex flow mechanisms at the fracture intersection such as stream tube routing and complete mixing (Berkowitz et al. 1994) as the flow direction in each subsegment is unknown. The influence of intersection angle is not considered either. Therefore, it is only

an approximation and should not be used when the flow details at the fracture intersection are vital for the total flow.

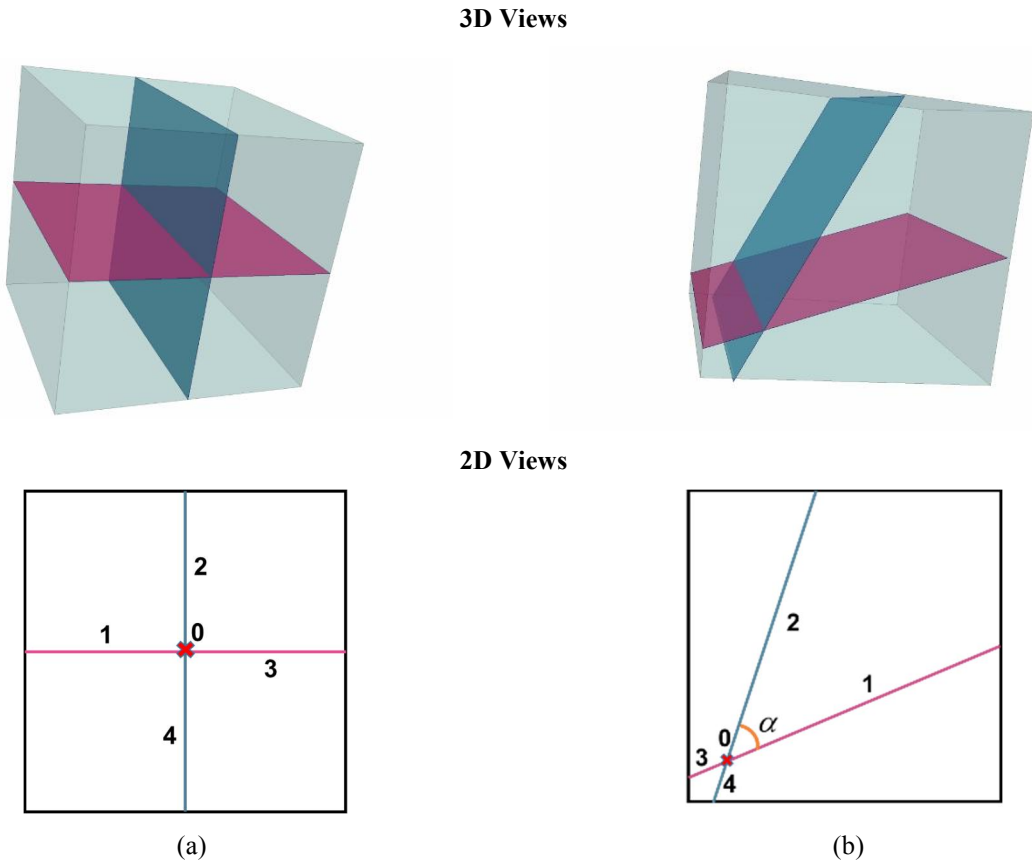


Figure 3.4: Illustration of the fracture intersection. At the intersection, every fracture segment is divided into 2 subsegments. In (a), all the subsegments have similar dimensions. In (b), there is a high contrast between areas of the subsegments.

3.2.3.4 Well-Fracture Intersection

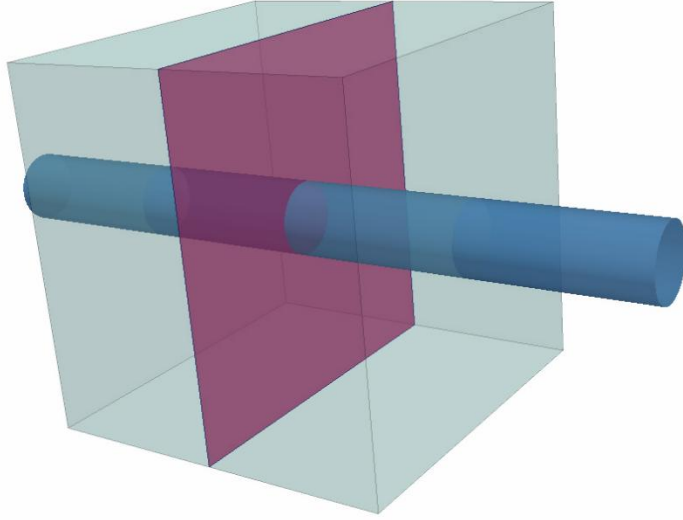


Figure 3.5: Illustration of the well-fracture intersection. The blue tube represents a wellbore and the red plane represents a fracture segment in a matrix gridblock.

In Moinfar et al. (2013c), the well-fracture intersections (as shown in Figure 3.5) in the EDFM are modeled by assigning an effective well index for each fracture segment that intersects the well trajectory. Based on the most commonly used formula proposed by Peaceman (1983)

$$WI = \frac{2\pi \sqrt{k_y k_z} \Delta x}{\ln(r_o / r_w)},$$

$$r_o = 0.28 \frac{(k_y \Delta z^2 + k_z \Delta y^2)^{1/2}}{k_y^{1/2} + k_z^{1/2}}, \quad (3.19)$$

Moinfar et al. (2013c) proposed a method to calculate the effective well indices for fracture wellblocks

$$WI_f = \frac{2\pi k_f w_f}{\ln(r_e / r_w)}, \quad (3.20)$$

$$r_e = 0.14\sqrt{L^2 + W^2}, \quad (3.21)$$

where k_f is the fracture permeability, w_f is the fracture aperture, L and W are the length and height of the fracture segment, respectively. This method can be derived by replacing the dimensions and permeability of the gridblock in Peaceman's model with those of the fracture segments.

It should be noted that the fractures normally have very high conductivities, thus the effective well indices can have large values. Our tests show that above some value (for example, 10,000 md-ft), further increase in WI_f will not affect the simulation results. Furthermore, large values of WI_f can cause numerical instability. Therefore, when the fracture permeability is very high, a smaller value, for example, 10,000 md-ft can be used as the effective well index to speed up the calculation without losing the accuracy.

3.2.4 Porosity cutoff method

The EDFM may introduce some small control volumes as the volumes of the fracture segments are typically small compared to that of matrix cells. These small control volumes may severely limit the time steps in the simulator. For fluid flow in fractures, the most influencing parameter is the fracture conductivity, which is defined as

$$F_{cd} = w_f \times k_f, \quad (3.22)$$

where w_f is the fracture aperture and k_f is the fracture permeability. If we increase the fracture aperture and decrease the fracture permeability, it is possible to keep the fracture conductivity unchanged, and this is a method used in some commercial reservoir simulators (*IMEX User Guide 2014*). Following this idea, in the EDFM, a “porosity cutoff” method

can be used. When the effective fracture porosity (ϕ_f) is lower than a “porosity cutoff value” ϕ_{cutoff} , the fracture aperture and permeability will be changed to

$$w_f^{new} = w_f \times \frac{\phi_{cutoff}}{\phi_f}, \quad (3.23)$$

$$k_f^{new} = k_f \times \frac{\phi_f}{\phi_{cutoff}}, \quad (3.24)$$

where w_f^{new} and k_f^{new} are the updated fracture aperture and fracture permeability, respectively. The updated effective fracture porosity is

$$\phi_f^{new} = \phi_{cutoff}. \quad (3.25)$$

It should be noticed that the change in ϕ_f will not result in any change in the connection factor calculations mentioned in the previous section. By changing the control volumes of fracture segments, the time step problem in simulation may to some extent be solved.

3.2.5 EDFM Preprocessor

The calculations of the connection factors, including NNC transmissibility factors and fracture well indices, depend only on gridding, reservoir permeability, and fracture geometries. No time-varying properties (such as pressure and saturation) are involved in the formulations. Therefore, the calculations of connection factors in the EDFM can be independent from reservoir simulation. Cavalcanto Filho et al. (2015) developed an EDFM preprocessor for UTCOMP (an in-house IMPES-type compositional reservoir simulation developed at The University of Texas) and UTCHEM for these calculations. The program was written in Python. The inputs of the preprocessor are

- Reservoir dimensions and grid size

- Matrix permeability (full tensor or only diagonal elements)
- Location of wells
- Number of fractures
- Permeability, aperture, and location (coordinates of the fracture plane vertices) of each fracture

In the preprocessor, it calculates

- Intersections between fracture planes and matrix cells
- Intersections between fractures
- Intersections between fracture planes and wellbore axes
- Coordinates of the fracture segment vertices
- Transmissibility factors for three types of NNCs
- Well indices for well-fracture intersection

For UTCOMP and UTCHEM simulators, the outputs of the preprocessor are

- The total number of fracture segments (which is also the number of fracture cells)
- Effective fracture porosity, permeability, and depth of each fracture cell
- Number of NNCs for each cell and lists of NNC pairs
- Transmissibility factors for NNCs
- Number of fracture wellblocks for each well
- Well index for each fracture-well intersection

The outputs of the EDFM preprocessor will be read into the reservoir simulators.

In simulation, the total number of gridblocks is increased to honor the fracture cells. Then NNCs and fracture wellblocks will be added for flow simulations. The EDFM preprocessor only calculates the phase independent part of the connection factors, and the phase dependent part is calculated by simulators. The corresponding changes in reservoir simulators are discussed in next chapter.

3.3 HIGHLIGHTS OF THE CHAPTER

- The UTCHEM reservoir simulator was developed to simulate different enhanced oil recovery processes. The basic features and governing equations of UTCHEM were introduced in this chapter as a basis for the implementation of the EDFM in UTCHEM in next chapter.
- The embedded discrete fracture model (EDFM) was developed as a combination of dual-continuum models and discrete fracture models. By adding extra fracture cells into the computational domain, the EDFM can keep the original functionalities of the simulators and avoid the computational complexity of unstructured gridding.
- Through non-neighboring connections (NNCs), the EDFM introduces the flow communications between matrix, fractures, and wells. Three types of NNC transmissibility factors and the fracture well indices are calculated in the EDFM.
- A porosity-cutoff method is used in the EDFM to avoid the time step problems caused by small control volumes.
- The input parameters of the EDFM are time-invariant, which leads to the development of an EDFM preprocessor. The EDFM preprocessor translates the geometry information about matrix and fractures into transport indices for reservoir simulators.

Chapter 4: Model Implementation and Verification

In this chapter, we first briefly introduce the formulations and methodology to implement the Embedded Discrete Fracture Model (EDFM) in the UTCHEM and commercial simulators. Subsequently, we present several simulation examples to examine the accuracy of the EDFM and its implementation. First, we show a case with intersecting orthogonal fractures, with all types of connections in the EDFM. We compare the results of UTCHEM-EDFM with CMG-EDFM and an explicit fracture model using local grid refinement. Then, the accuracy of the EDFM for modeling non-orthogonal fractures is confirmed through comparison with a carefully gridded fine model. Finally, a 3D case with an inclined fracture is presented. We perform a grid sensitivity study to show the accuracy of the EDFM with different grid sizes.

4.1 IMPLEMENTATION OF THE EDFM IN RESERVOIR SIMULATORS

Simulation of fluid flow in fractured reservoirs is a significant yet challenging problem in reservoir simulators. By using non-neighboring connections (NNCs), the EDFM can be implemented in reservoir simulators and empower the simulators to model fractured reservoirs without losing the original functionalities. In this section, we implemented the EDFM in both the UTCHEM reservoir simulator and commercial simulators. We first briefly discuss the implementation methodology and related formulations, and the verifications will also be presented.

4.1.1 EDFM in UTCHEM Reservoir Simulator

As introduced in Chapter 3, UTCHEM is a powerful reservoir simulator with many useful features for modeling of enhanced oil recovery processes. With the EDFM, the range of problems that UTCHEM can solve will be greatly extended. In general, two steps are required to implement the EDFM in simulators. First, the fracture cells need to be added

into the computational domain. Second, the corresponding cells in NNC pairs need to be connected to allow for flow communications.

In UTCHEM, fracture cells can be easily added into the computational domain by creating virtual cells. The pore volumes of these cells are set as the actual volume of the fracture segments. This can be done by assigning effective fracture porosity for these cells.

In Equation 3.11

$$\phi_f = \frac{S_{\text{seg}} w_f}{V_b}, \quad (3.11)$$

we set V_b as the volume of the matrix cell containing the fracture segment. The depths of the fracture cells are defined based on the position of the centroids of these segments. The total number of added cell is the same as the number of fracture segments.

The only connections of the fracture cells are the NNCs generated by the EDFM preprocessor. When adding these connections, we consider the mass conservation equation, pressure equation, and the energy conservation equation.

In Chapter 3, we show the mass conservation equation in UTCHEM as

$$\frac{\partial}{\partial t} (\phi \tilde{C}_k \rho_k) + \vec{\nabla} \cdot \left[\sum_{l=1}^{n_p} \rho_k \left(C_{kl} \vec{u}_l - \vec{\bar{D}}_{kl} \right) \right] = R_k. \quad (3.1)$$

If we integrate both sides of the equation over the volume of a gridblock, we can get

$$V_b \frac{\partial}{\partial t} \left(\overline{\phi \tilde{C}_k \rho_k} \right) + \sum_{i=1}^{n_s} \left[\sum_{l=1}^{n_p} \overline{\rho_k \left(C_{kl} \vec{u}_l - \vec{\bar{D}}_{kl} \right)} \right] S_i = V_b \overline{R_k}, \quad (4.1)$$

where V_b is the bulk volume of the gridblock, n_s is the number of common faces the gridblock has with neighboring gridblocks, and S_i is the area of the i th common face. $\overline{\phi \tilde{C}_k \rho_k}$ and $\overline{R_k}$ are averaged over V_b . $\overline{\rho_k \left(C_{kl} \vec{u}_l - \vec{\bar{D}}_{kl} \right)}$ is averaged over S_i and it is positive when the flow is from the gridblock to the neighboring gridblock. In Cartesian

grids, $n_s = 6$ for gridblocks away from boundaries, and $n_s < 6$ for gridblocks on boundaries.

In the EDFM, NNCs are added to account for the flow associated with fractures. Using a first-order approximation and considering the convective term only, the flow rate between two cells (m and n) within a NNC pair is

$$q_{m>n,l} = [(P_1 + P_{cl1} - \gamma_l h)|_m - (P_1 + P_{cl1} - \gamma_l h)|_n] T_{NNC,m-n} \lambda_{rlc}, \quad (4.2)$$

where $q_{m>n,l}$ is the volume flow rate of phase l from cell m to cell n and $T_{NNC,m-n}$ is the NNC transmissibility factor between cell m and cell n . If a gridblock has n_{NNC} NNCs with gridblocks $\{M_1, M_2, \dots, M_{n_{NNC}}\}$, and we include these flow terms in Equation 4.1, we can get

$$V_b \frac{\partial}{\partial t} \left(\overline{\phi \tilde{C}_k \rho_k} \right) + \sum_{i=1}^{n_p} \left[\sum_{l=1}^{n_p} \overline{\rho_k \left(C_{kl} \vec{u}_l - \vec{D}_{kl} \right)} \right] S_i - \sum_{j=1}^{n_{NNC}} \sum_{l=1}^{n_p} \rho_k C_{kl} q_{NNC,j,l} = V_b \overline{R_k}, \quad (4.3)$$

and

$$q_{NNC,j,l} = [(P_1 + P_{cl1} - \gamma_l h)|_{M_j} - (P_1 + P_{cl1} - \gamma_l h)] T_{NNC,j} \lambda_{rlc}, \quad (4.4)$$

where $q_{NNC,j,l}$ is the flow rate of phase l between a cell and its j th non-neighboringly connected cell in the EDFM (M_j) and $T_{NNC,j}$ is the transmissibility factor for this connection. We use Equation 4.3 as the modified version of the mass conservation equation in our implementation.

For the pressure equation, we make similar changes to include the NNCs. By rearranging the pressure equation in UTCHEM, we obtain

$$\varphi C_t \frac{\partial P_1}{\partial t} = \sum_{l=1}^{n_p} \vec{\nabla} \cdot \vec{K} \cdot \lambda_{rlc} \vec{\nabla} (P_l + P_{cl1} - \gamma_l h) + \sum_{k=1}^{n_{cv}} Q_k. \quad (4.5)$$

Integrating both sides of the equation and writing the surface integrations in discretized form, we have

$$\varphi C_t \frac{\partial \bar{P}_1}{\partial t} V_b = \sum_{i=1}^{n_s} \sum_{l=1}^{n_p} \left\{ \lambda_{rlc} \left[(P_l + P_{cl1} - \gamma_l h) |_{N_i} - (P_l + P_{cl1} - \gamma_l h) \right] T_i \right\} + \sum_{k=1}^{n_{cv}} \bar{Q}_k V_b , \quad (4.6)$$

where N_i ($i = 1, 2, \dots, n_s$) is the gridblock's i th neighboring gridblock, and T_i is the corresponding transmissibility factor between the gridblock and N_i . \bar{P}_1 and \bar{Q}_k are averaged over V_b . Here a first-order approximation of the flux is used. By including the flow terms related to NNCs, the equation becomes

$$\begin{aligned} \varphi C_t \frac{\partial \bar{P}_1}{\partial t} V_b &= \sum_{i=1}^{n_s} \sum_{l=1}^{n_p} \left\{ \lambda_{rlc} \left[(P_l + P_{cl1} - \gamma_l h) |_{N_i} - (P_l + P_{cl1} - \gamma_l h) \right] T_i \right\} \\ &+ \sum_{j=1}^{n_{NNC}} \sum_{l=1}^{n_p} \left\{ \lambda_{rlc} \left[(P_l + P_{cl1} - \gamma_l h) |_{M_j} - (P_l + P_{cl1} - \gamma_l h) \right] T_{NNC,j} \right\} + \sum_{k=1}^{n_{cv}} \bar{Q}_k V_b \end{aligned}, \quad (4.7)$$

and this is the modified version of pressure equation in our implementation.

Note that in an IMPES-type formulation, the pressure equation is solved implicitly. Therefore, the fracture cells increase the size of the matrix representing the discretized pressure equation and will to some extent increase the CPU time when compared to the case without fractures.

We apply similar changes in the energy conservation equation

$$\frac{\partial}{\partial t} \left[(1-\phi) \rho_s C_{vs} + \phi \sum_{l=1}^{n_p} \rho_l S_l C_{vl} \right] T + \vec{\nabla} \cdot \left(\sum_{l=1}^{n_p} \rho_l C_{pl} u_l T - \lambda_T \vec{\nabla} T \right) = q_H - Q_L . \quad (3.7)$$

By integrating both sides of the equation, adding the NNCs, and separating the conductive and convective terms, we get

$$\begin{aligned} V_b \frac{\partial}{\partial t} \left[(1-\phi) \rho_s C_{vs} + \phi \sum_{l=1}^{n_p} \rho_l S_l C_{vl} \right] \bar{T} \\ = \sum_{j=1}^{n_{NNC}} \sum_{l=1}^{n_p} \left\{ \overline{\rho_l C_{pl} T} q_{NNC,j} \right\} - \sum_{i=1}^{n_s} \left[\sum_{l=1}^{n_p} \overline{\rho_l C_{pl} u_l T} \right] S_i \\ + \sum_{i=1}^{n_s} \sum_{l=1}^{n_p} \left\{ (T_{N_i} - T) S_i \lambda_T / d_i \right\} + \sum_{j=1}^{n_{NNC}} \sum_{l=1}^{n_p} \left\{ (T_{M_j} - T) S_{NNC,j} \lambda_T / d_{NNC,j} \right\} \end{aligned}, \quad (4.8)$$

where \bar{T} is averaged over V_b , $\overline{\rho_l C_p T}$ and $\overline{\rho_l C_p u_l T}$ are averaged over the corresponding surface, T_{N_i} is the temperature of gridblock N_i , T_{M_j} is the temperature of gridblock M_j , and $S_{NNC,j}$ and $d_{NNC,j}$ are the area and distance associated with the j th NNC of the gridblock, respectively.

The fracture-well intersection can also be easily implemented by adding extra well perforations in the simulators. We skip this part as the details of the fracture well index calculation have already been discussed in Chapter 3.

With the modifications in the governing equations, the connections in the EDFM have been added into UTCHEM. We refer the modified version of UTCHEM as UTCHEM-EDFM.

4.1.2 EDFM in Commercial Reservoir Simulators

The description of the EDFM methodology in Chapter 3 is general and can be applied in different reservoir simulators. Since the major idea of the EDFM is to model flow communications using non-neighboring connections, any simulator with non-neighboring connection functionality can be used as an engine for the EDFM simulations. In addition, the range of problems the EDFM can handle and the physics involved depend mainly on the capability of the simulator. Here we describe the method to apply the EDFM in commercial simulators in a non-intrusive way without having access to the source code of the simulators.

Contrary to UTCHEM, in commercial simulators, there is no direct method to add virtual cells in computational domain. Therefore, an indirect method is used to create the fracture cells. By increasing N_x (the number of gridblocks in X direction), we append the fracture cells in X direction. The added N_x is

$$N_{x,add} = \text{Floor}\left[\left(N_{seg} - 1\right) / (N_y * N_z)\right] + 1, \quad (4.9)$$

where N_{seg} is the number of fracture segments, N_y and N_z are the numbers of gridblocks in Y and Z direction, respectively, and Floor is a function which returns the largest integer less than or equal to the value in the square bracket. Therefore, the new value for N_x is

$$N_{x,new} = N_{x,old} + N_{x,add}, \quad (4.10)$$

and the total number of added cells is

$$N_{B,add} = N_{x,add} \times N_y \times N_z. \quad (4.11)$$

Since only N_{seg} cells are required to represent the fracture segments, $(N_{B,add} - N_{seg})$ cells will be set as null cells.

It should be noted that there is no difference whether to add the extra cells in X, Y or Z direction. We choose X direction in our implementation due to memory consideration.

For the newly-added cells, their dimensions in Y and Z directions are determined by the original matrix grid size (Cartesian grid). In X direction, the dimension of these cells can be any chosen value. However, it should be noted that V_b in Equation 3.11 is the bulk volume of the added cell. Since $S_{seg} w_f$ is the actual volume of the fracture segment, the choice of cell dimension in X direction will influence the value of ϕ_f .

Since the simulator will automatically generate connections for these newly-added cells, we cancel all these connections through transmissibility multipliers and add non-neighboring connections. Many simulators allow the direct definition of NNC transmissibility factors (*IMEX User Guide* 2014; *Eclipse Reference Manual* 2014). As introduced before, these transmissibility factors are generated in EDFM preprocessor and passed to simulators through some keywords. In CMG, which is a commercial reservoir

simulator developed by Computer Modeling Group Ltd, the keyword is “SCONNECT”. In Eclipse, a commercial reservoir simulator developed by Schlumberger, the keyword is “NNC” or “NNCGEN”. We wrote a converter in Fortran to translate the outputs for UTCOMP to the format required by the commercial simulators.

Following the methodology described above, we apply the EDFM approach in CMG-IMEX. However, as stated before, the EDFM is a non-intrusive method that may be used in any finite-difference reservoir simulator capable of handling non-neighboring connections. Therefore, the methodology described in this section is also applicable to other simulators. In the rest of this thesis, when we use the EDFM in CMG-IMEX, we refer the simulator as CMG-EDFM.

4.2 MODEL VERIFICATIONS

In this section, we present several case studies to verify the accuracy of the EDFM as well as the model implementation in reservoir simulators.

4.2.1 3D Orthogonal Fractures

The operation of hydraulic fracturing may cause the reopening of pre-existing natural fractures, leading to complex fracture networks. In this section, we present a 3D case with 8 intersecting orthogonal fractures. The EDFM approach is compared to an explicit-fracture model where the fractures are modeled through local grid refinement (LGR), to verify the accuracy of the EDFM in modeling fracture networks. Figure 4.1 shows the dimensions of the reservoir and the positions of the well and fracture planes. The reservoir dimensions are $1560 \times 1000 \times 100$ ft, and the fractures do not fully penetrate the reservoir height (with a distance of 20 ft from the top and bottom of the reservoir). A horizontal well is located at the center of the reservoir. All the fracture planes are vertical

and parallel to the reservoir boundaries. The fractures have a width of 0.01 ft and a permeability of 10,000 md, which gives a fracture conductivity of 100 md-ft. A uniform $78 \times 50 \times 10$ matrix grid is used in this study, and the dimensions of the matrix cells are $20 \times 20 \times 10$ ft.

This example is primary depletion of a low permeability oil reservoir. The horizontal well has a constant bottomhole pressure. The flowing phases are water and oil. The reservoir is anisotropic as the permeabilities in X and Y directions are 10 times as that in Z direction. The viscosities of water and oil phases are assumed to be constant. The influences of capillary pressure and gravity are ignored in this case. Corey model is used for relative permeability curve for both matrix and fracture. Peaceman's model is used to calculate the well indices. The detailed reservoir properties and simulation parameters are summarized in Table 4.1.

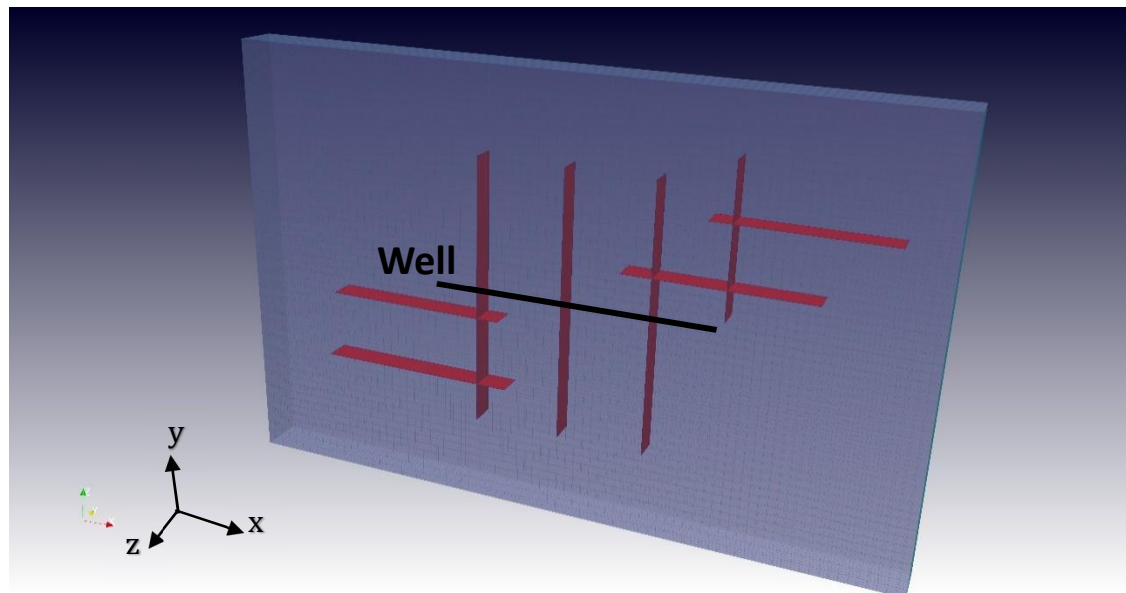


Figure 4.1: A reservoir model with 8 intersecting orthogonal fractures.

Reservoir Properties		Relative Permeability Curve	
Matrix permeability Kx (md)	0.1	Residual water saturation	0.2
Matrix permeability Ky (md)	0.1	Residual oil saturation	0.2
Matrix permeability Kz (md)	0.01	Water rel. perm. endpoint	0.8
Reservoir porosity	0.3	Oil rel. perm. endpoint	0.7
Reservoir pressure (psi)	3000	Water rel. perm. exponent	2.0
Reservoir Temperature (°F)	120	Oil rel. perm. exponent	2.0
Rock compressibility (psi^{-1})	1×10^{-6}	Well Properties	
Water compressibility (psi^{-1})	1×10^{-6}	Wellbore radius (ft)	0.5
Oil compressibility (psi^{-1})	1.64×10^{-6}	Well length (ft)	600
Water viscosity (cp)	0.8	Bottomhole pressure (psi)	1500
Oil viscosity (cp)	1	Simulation Parameters	
Initial water saturation	0.4	Simulation time (day)	1000
Initial oil saturation	0.6	Maximum time step (day)	10

Table 4.1: Reservoir properties and some of the simulation parameters.

Designed for verification purpose, this case has five fracture-fracture intersections and three fracture-well intersections in it. Therefore, all types of connections in the EDFM can be tested with this case. In the simulation, the number of fracture cells is 1164 and the maximum number of NNCs for a single fracture cell is 6 (2 in X or Y direction, 2 in Z direction, 1 with matrix cell, and 1 with intersected fracture segment). Three fracture cells are defined as wellblocks due to fracture-well intersections. We used the EDFM in both UTCHEM and CMG-IEMX for verification of the EDFM implementation. We also explicitly modeled the fractures through LGR in CMG-IMEX to verify the accuracy of the EDFM. In the local grid refinement model, the cells containing fractures are refined (into 5 sub-cells in the direction perpendicular to the fracture plane) and the permeability and porosity of the sub-cells in the middle are modified to the fracture permeability (10,000

md) and fracture porosity (1.0), respectively. To model the fracture intersections, the cells with fracture intersections are refined in both X and Y directions as shown in Figure 4.2.

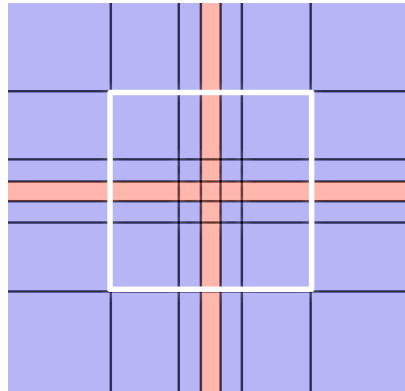


Figure 4.2: Illustration of local grid refinement at the fracture intersections in the fine model. The white box shows the size of the coarse gridblock. The sub-cells representing fractures are shown in orange and the sub-cells representing matrix are shown in blue.

Figures 4.3 and 4.4 show the average reservoir pressures, oil production rates, and water production rates of different models. As an observation, the results of UTCHEM-EDFM and CMG-EDFM are highly consistent in all three plots, verifying the implementation of UTCHEM-EDFM. Furthermore, the EDFM reaches very similar results as the LGR model, confirming its accuracy. Figure 4.5 shows the pressure profiles of Layer 5 (the layer in the middle) after 5 and 32 days of production predicted by UTCHEM-EDFM and CMG-LGR, and a very good agreement can be observed.

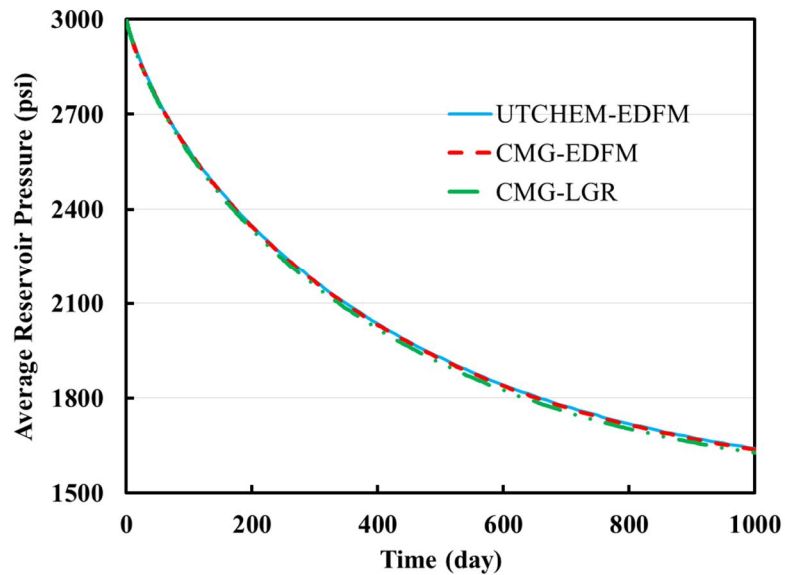
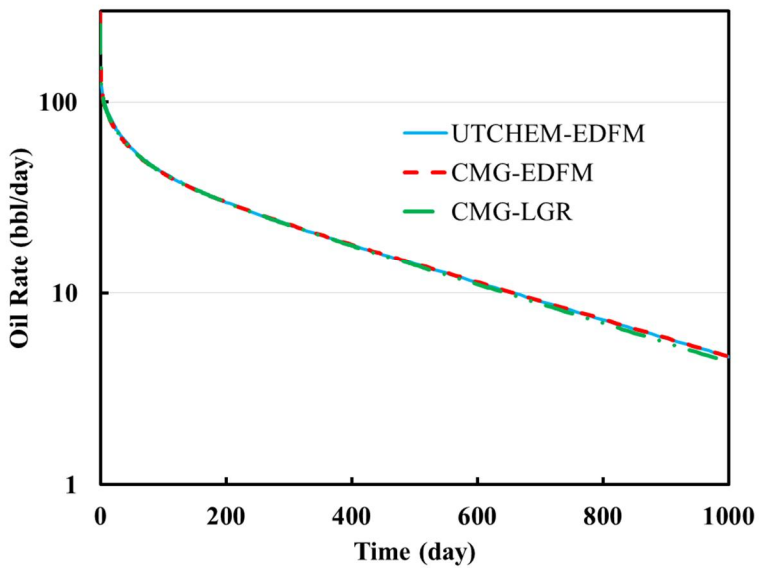
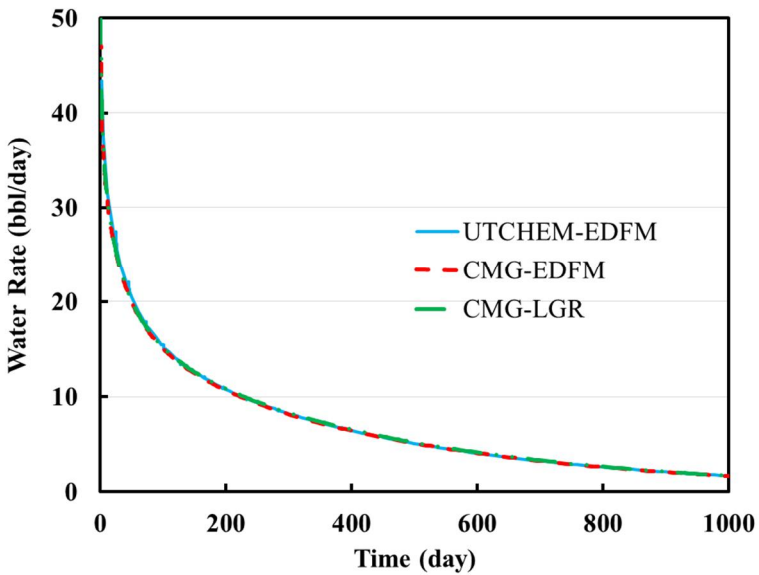


Figure 4.3: Comparison of average reservoir pressure for different models.



(a)



(b)

Figure 4.4: Comparison of (a) oil rate and (b) water rate of different models. Both of the rates are in reservoir condition. The oil rate is shown in log scale as it changes very rapidly during the early time.

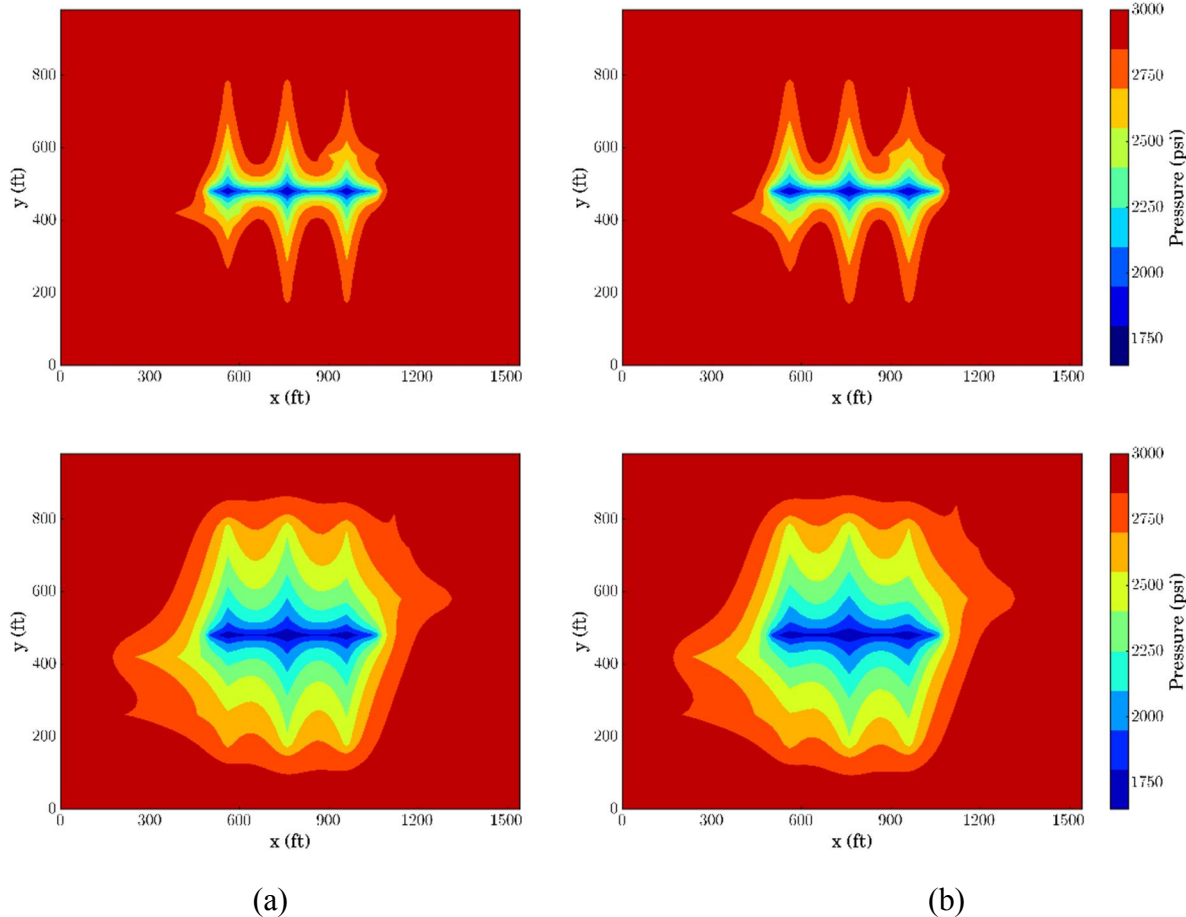


Figure 4.5: Pressure profiles of Layer 5 predicted by (a) UTCHEM-EDFM and (b) CMG-LGR. The rows from top to bottom show the pressure profiles for 5 days and 32 days, respectively.

4.2.2 2D Non-Orthogonal Fractures

In the previous case, different types of NNCs in the EDFM have been tested for orthogonal fractures. During hydraulic fracturing, the fractures tend to grow in the direction perpendicular to the minimum horizontal stress. In some cases, when the well axis deviates from the direction of the minimum horizontal stress, the preferred direction of fracture propagation will not be perpendicular to the wellbore. This often leads to the propagation of non-orthogonal fractures. One of the advantages of the EDFM is its flexibility in modeling fractures in any orientation.

In this section, we present a 2D case with four non-orthogonal fractures, and verify the applicability of the EDFM for modeling non-orthogonal fractures with an LGR model. Figure 4.6 shows the dimensions of the reservoir and the positions of the well and fracture planes.

This example is a primary depletion of an ultra-tight oil reservoir. Oil is the main flowing phase. The dimensions of the reservoir are $523.5 \times 600 \times 80$ ft. A uniform $349 \times 400 \times 1$ matrix grid is used in this study, and the dimensions of the matrix cells are $1.5 \times 1.5 \times 80$ ft. The aim of using such small gridblock size in this study is to make the simulation results using LGR more accurate. The reservoir is very tight, with a permeability of 0.0005 md. All the fractures have a same aperture of 0.015 ft, and the fracture permeability is set to be 10,000 md; therefore, the fracture conductivity is 150 md-ft. The capillary effect is not considered in this study. We use Corey model for the relative permeability curve. Other reservoir properties and some simulation parameters are summarized in Table 4.2.

We use both UTCHEM-EDFM and CMG-EDFM simulators to perform this case study. The number of fracture cells is 1204. Also, as an attempt, we created a model in CMG-IMEX using LGR to simulate the angle of the fractures. Since it is always difficult

to “exactly” model non-orthogonal fractures by grid refinement, a “zigzag” approach is used to approximately represent the non-orthogonal fractures as shown in Figure 4.7. The cells containing fractures are refined into 3×3 sub-grids.

Figure 4.8 compares the average reservoir pressure and Figure 4.9 compares the oil production rates for different models. Again, the accuracy of UTCHEM-EDFM is verified as we observe a high consistency between UTCHEM-EDFM and CMG-EDFM. In addition, as a close agreement between the EDFM and the LGR model can be observed, the accuracy of the EDFM for modeling non-orthogonal fractures is verified. The similar pressure profiles at different time (20 days, 90 days, and 300 days) predicted by UTCHEM-EDFM and CMG-LGR (shown in Figure 4.10) further confirm the model accuracy.

It should be pointed out that in the LGR model, the grid size and the properties of the refined gridblocks need to be carefully designed to model the fracture angle, which is painful. However, in the EDFM, it is natural and easy to model such fractures. With the EDFM preprocessor, any orientation of fractures can be easily modeled in the EDFM and no extra effort needs to be paid. This feature empowers the EDFM to be a convenient tool in uncertainty analysis as the orientations of fractures are always full of uncertainty.

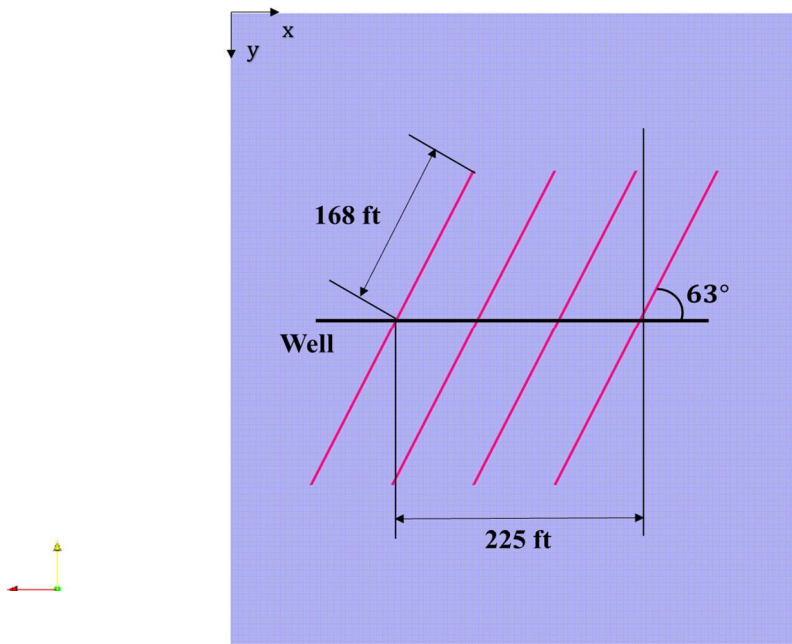


Figure 4.6: A reservoir model with 4 non-orthogonal fractures. Fractures have an intersection angle of 63° with the wellbore.

Reservoir Properties		Relative Permeability Curve	
Matrix permeability Kx (md)	0.0005	Residual water saturation	0.2
Matrix permeability Ky (md)	0.0005	Residual oil saturation	0.2
Matrix permeability Kz (md)	0.0005	Water rel. perm. endpoint	0.8
Reservoir porosity	0.12	Oil rel. perm. endpoint	0.7
Reservoir pressure (psi)	3000	Water rel. perm. exponent	2.0
Reservoir Temperature ($^{\circ}$ F)	120	Oil rel. perm. exponent	2.0
Rock compressibility (psi^{-1})	1×10^{-6}	Well Properties	
Water compressibility (psi^{-1})	1×10^{-6}	Wellbore radius (ft)	0.5
Oil compressibility (psi^{-1})	1.64×10^{-6}	Well length (ft)	265
Water viscosity (cp)	0.8	Bottomhole pressure (psi)	1000
Oil viscosity (cp)	1.0	Simulation Parameters	
Initial water saturation	0.2	Simulation time (day)	1000
Initial oil saturation	0.8	Maximum time step (day)	3

Table 4.2: Reservoir properties and some of the simulation parameters.

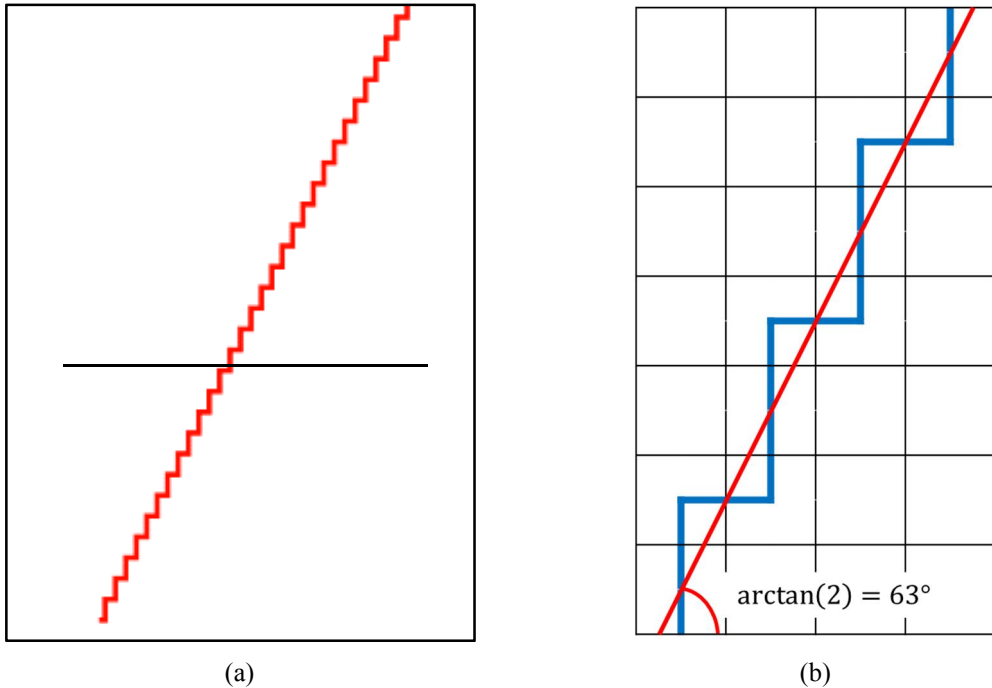


Figure 4.7: Explanation of “zigzag” in the fine model. The red lines in (a) represents the high permeability sub-grids for fractures. A closer view is given in (b), where the red line shows the actual fracture shape and the blue lines show the “zigzag” representation of the fracture shape.

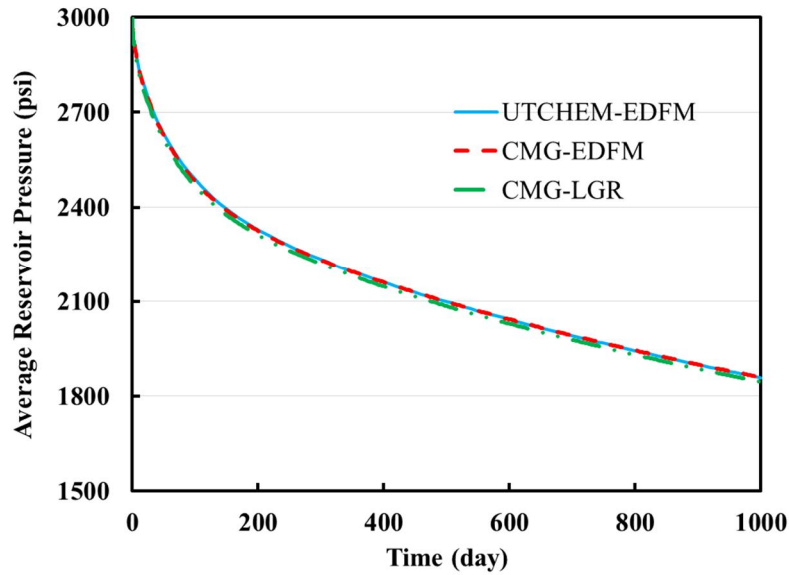


Figure 4.8: Comparison of average reservoir pressure for different models.

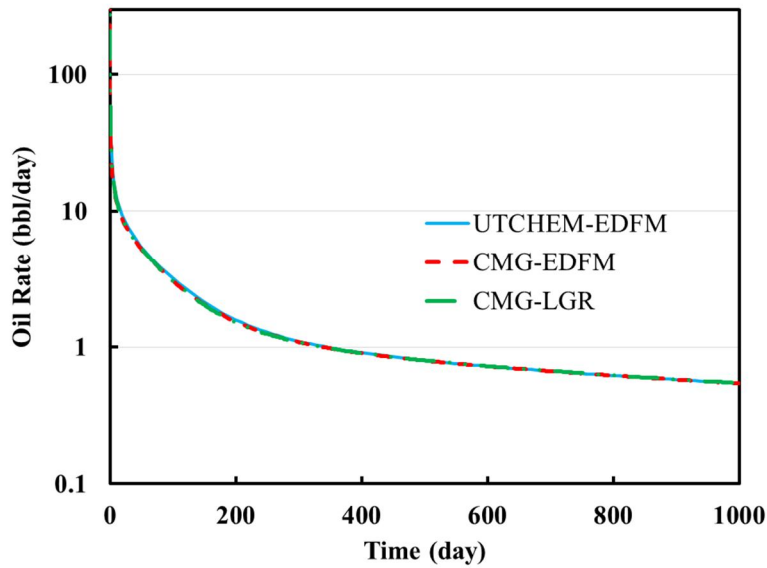


Figure 4.9: Comparison of oil production rates (reservoir condition) for different models. The oil rate is shown in log scale due to its rapid change during early time.

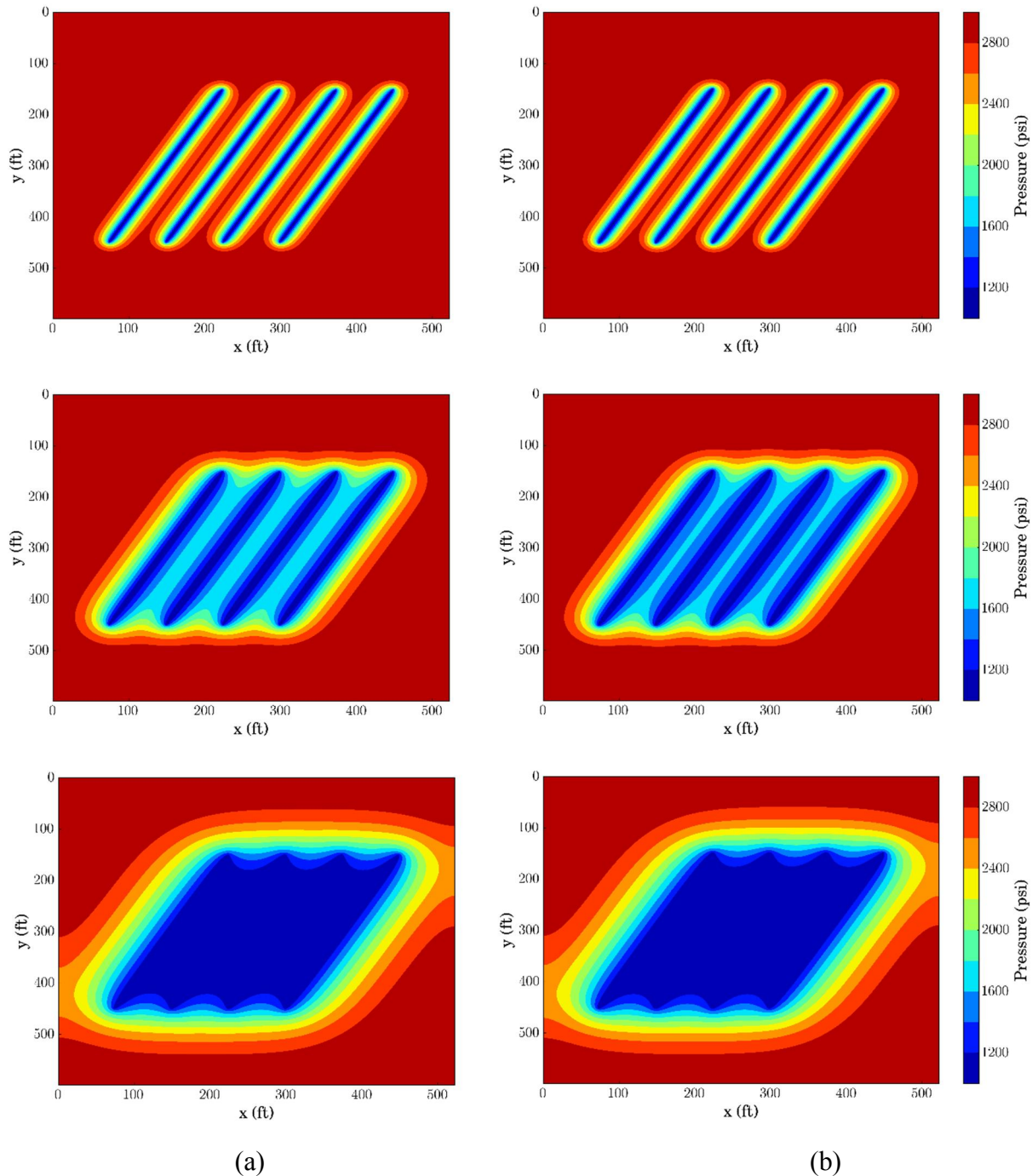


Figure 4.10: Pressure profiles predicted by (a) UTCHEM-EDFM and (b) CMG-LGR. The rows from top to bottom show the pressure profiles for 20 days, 90 days and 300 days, respectively.

4.2.3 3D Inclined Fracture

Generally, the overall hydraulic fracture plane in an isotropic medium is parallel, inclined, or perpendicular to the wellbore. If the shear stresses on the borehole wall make the maximum tensile stress different from the axial or tangential stress, inclined fractures may initiate (Daneshy 1973). The EDFM has the flexibility to handle inclined fractures. In Chapter 3, we showed an example of inclined fracture where the fracture segments can be triangle, quadrilateral, pentagon, or hexagon (Figure 3.3). In this section, we use this example to verify the accuracy of the EDFM for 3D inclined fracture modeling.

Figure 4.11 shows the dimensions of the reservoir and the positions of the well and fracture plane. The size of the reservoir is $1000 \times 1000 \times 1000$ ft. The inclined fracture has a dip angle of 43° , and the fracture plane intersects the reservoir boundary at four points: $(190, 0, 0)$, $(815, 1000, 0)$, $(0, 1000, 644.5)$, and $(1000, 118.8, 208.9)$. The fracture aperture is 0.01 ft and the fracture permeability is 8×10^5 md. The axis of the well is in Y direction and there is an intersection between the wellbore and the fracture plane.

The reservoir has an initial water saturation that is the same as the residual water saturation, so the main flowing phase is oil. The capillary effect is not considered in this study, but the influence of gravity is considered. Corey relative permeability model is applied in this study. Other reservoir properties and some simulation parameters are shown in Table 4.3.

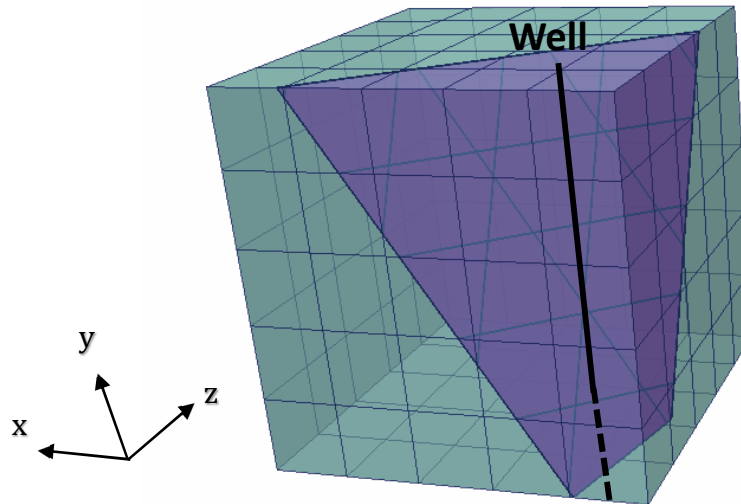


Figure 4.11: A reservoir model with an inclined fractures.

Reservoir Properties		Relative Permeability Curve	
Matrix permeability $K_x=K_y=K_z$ (md)	0.2	Residual water saturation	0.2
Reservoir porosity	0.2	Residual oil saturation	0.2
Reservoir pressure (psi)	3000	Water rel. perm. endpoint	0.8
Reservoir Temperature ($^{\circ}$ F)	120	Oil rel. perm. endpoint	0.7
Rock compressibility (psi^{-1})	1×10^{-6}	Water rel. perm. exponent	2.0
Water compressibility (psi^{-1})	1×10^{-6}	Oil rel. perm. exponent	2.0
Oil compressibility (psi^{-1})	1.64×10^{-6}	Well Properties	
Water viscosity (cp)	0.79	Wellbore radius (ft)	0.5
Oil viscosity (cp)	1.0	Well length (ft)	1000
Water density (lbm/ft^3)	62.4	Bottomhole pressure (psi)	1000
Oil density (lbm/ft^3)	40	Simulation Parameters	
Initial water saturation	0.2	Simulation time (day)	1000
Initial oil saturation	0.8	Maximum time step (day)	10

Table 4.3: Reservoir properties and some of the simulation parameters.

A fine-grid explicit-fracture model is created in CMG-IMEX as an attempt to model the fracture shape. In this model, a uniform $70 \times 70 \times 70$ matrix grid is used, with the dimensions of the matrix cells of $14.3 \times 14.3 \times 14.3$ ft. The inclined fracture is represented using a stair-stepping method where the cells intersected by the fracture plane are set with high permeability and porosity. In terms of permeability, to maintain the fracture conductivity, the permeability of these cells are modified to $k_{eff} = k_f \times w_f / w_{f,eff} = 559$ (md), where k_f and w_f are the real fracture permeability and aperture, respectively, and $w_{f,eff}$ is the effective fracture aperture, which is the size of the gridblock (14.3 ft) in this case. The porosity of these cells are modified to 1.0. Figure 4.12 shows the high permeability cells (to represent fracture) in the fine-grid simulation.

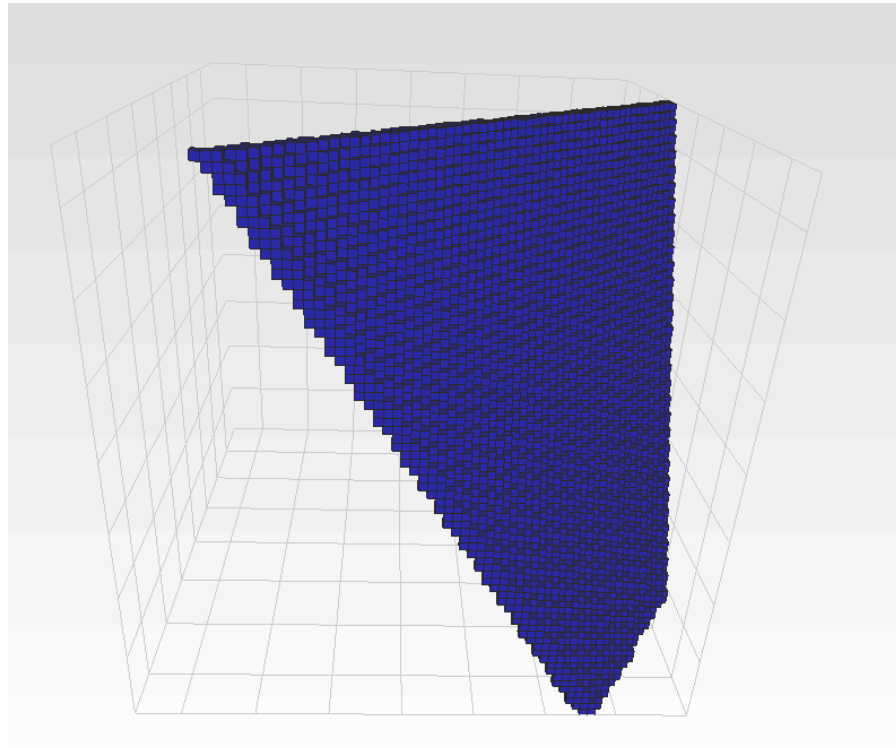


Figure 4.12: High permeability cells in the fine-grid model.

We performed three simulation runs using CMG-EDFM with different grid resolutions to check the convergence of the EDFM as the grid size decreases. The grid size used are summarized in Table 4.4. Figure 4.13 compares the average reservoir pressure for different models and Figure 4.14 presents the pressure profiles after 20 days of production. Both figures indicate that the EDFM can reach similar results as the fine-grid simulation, confirming of the accuracy of the EDFM for modeling inclined fractures.

Case	Case 1	Case 2	Case 3
Grid size	$5 \times 5 \times 5$	$10 \times 10 \times 10$	$20 \times 20 \times 20$
Cell dimensions (ft)	$200 \times 200 \times 200$	$100 \times 100 \times 100$	$50 \times 50 \times 50$
Number of fracture cells	29	113	451

Table 4.4: Gridding information for the EDFM simulations. Three different grid sizes are used.

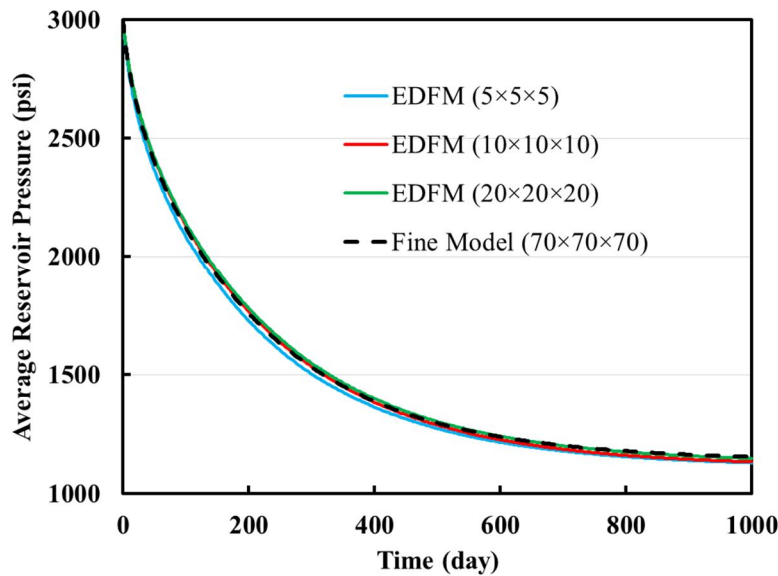


Figure 4.13: Comparison of average reservoir pressure predicted by fine-grid models and the EDFM approach with different matrix grid size.

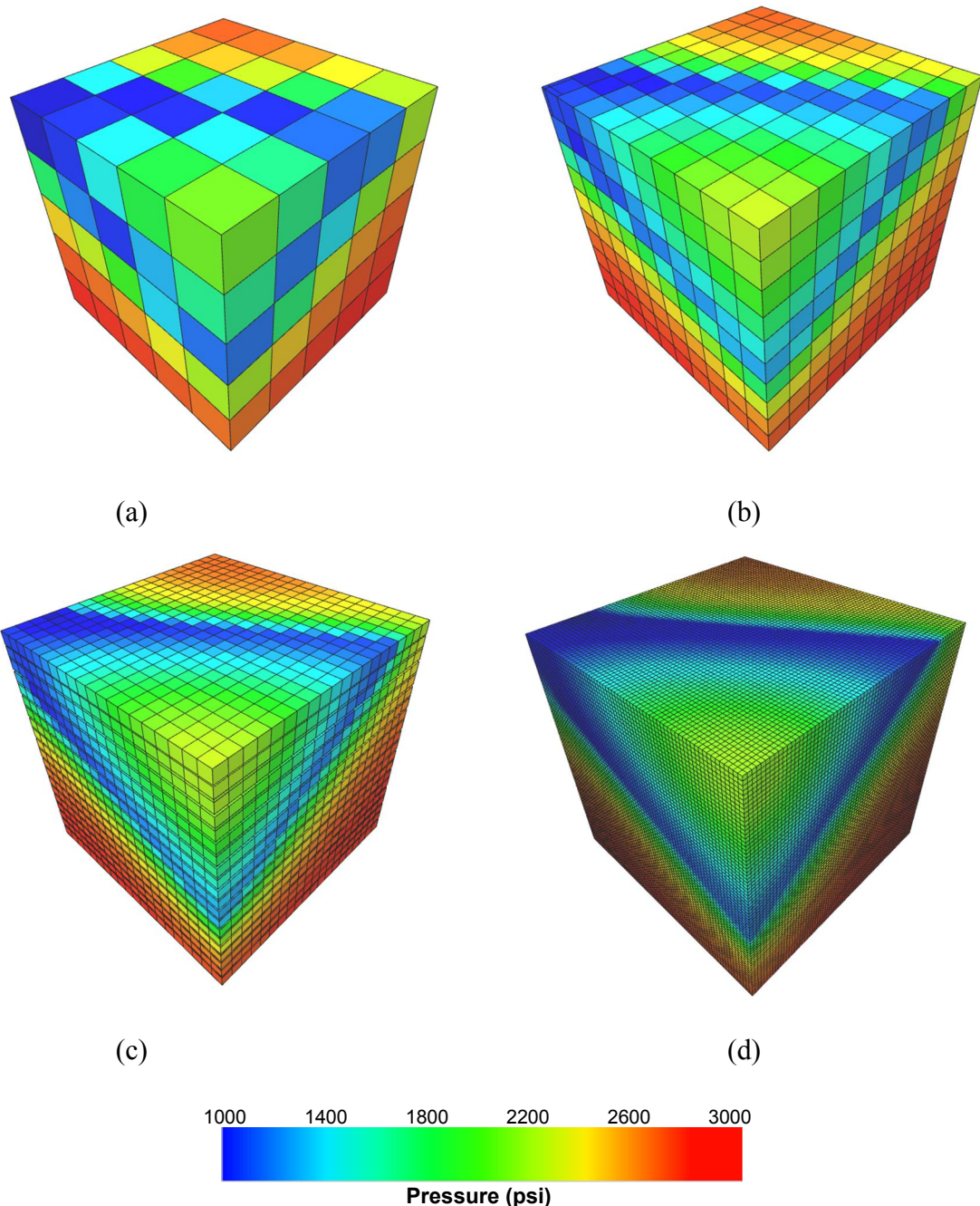


Figure 4.14: Pressure profiles predicted by (a) EDFM using a $5 \times 5 \times 5$ matrix grid (b) EDFM using a $10 \times 10 \times 10$ matrix grid (c) EDFM using a $20 \times 20 \times 20$ matrix grid (d) Fine-grid model using a $70 \times 70 \times 70$ grid.

It should also be noted that with increasing grid resolution, the accuracy of the EDFM would also be improved. Since in the EDFM, the fractures are partitioned into segments by the matrix cell boundaries, the finer the matrix grid is, the more fracture segments we would obtain (as shown in Table 4.4), and hence more accurate results can be obtained for the pressure calculations in the fracture plane. Also, the decreased grid size can effectively reduce the errors brought by the assumptions made in the NNC transmissibility factor calculations. Therefore, when possible, a smaller grid size is preferred in the EDFM simulation.

4.3 HIGHLIGHTS OF THE CHAPTER

- The formulations of the UTCHEM are modified to add extra connections in order to account for the fluid flow associated with fracture cells.
- Making use of the non-neighboring connection functionalities, we applied the EDFM to commercial simulators in a non-intrusive way.
- The accuracy of the UTCHEM-EDFM and CMG-EDFM was confirmed through comparison with LGR or fine-grid models.
- Examples of intersecting orthogonal fractures, non-orthogonal fractures, and 3D inclined fractures were presented. Through comparison with LGR or fine-grid models, the EDFM approach was proven to be accurate as well as flexible for different fracture orientations and dip angles.
- The accuracy of the EDFM can be improved with higher grid resolution.

Chapter 5: Application of the Embedded Discrete Fracture Model (EDFM) using UTCHEM and Commercial Simulators²

In Chapter 4, we showed the accuracy and applicability of the EDFM through several verification cases. In this chapter, we apply the EDFM to several field case studies to show the potential applications of this approach. First, we use the EDFM to model fractures with different orientations to investigate the influence of the intersection angle between hydraulic fractures and the wellbore. In the second example, we present a 3D water flooding case to show the applicability of the EDFM in modeling large-scale natural fractures. The influences of grid resolution and fracture relative permeability curve are also studied. Towards the end of this chapter, we modify the original formulations in the EDFM for simulation of a multi-lateral well stimulation technology. The modified formulations are confirmed by comparison with a multi-branch well method.

5.1 INFLUENCE OF FRACTURE-WELL INTERSECTION ANGLE

In Chapter 4, we presented a case verifying the EDFM for modeling non-orthogonal fractures. During hydraulic fracturing, there may be some uncertainties associated with the orientations of the fractures. The intersection angle between fractures and wellbore may have a significant influence on pressure distribution around fractures and ultimately influence the total production. In this section, we investigate the influence of this intersection angle by changing the orientations of the fractures. The simulator used in this study is UTCHEM-EDFM.

²Parts of this chapter has been presented in the following conference: Cavalcante Filho, J. S. de A., Xu, Y., Sepehrnoori, K et al. 2015. Modeling Fishbones Using the Embedded Discrete Fracture Model Formulation: Sensitivity Analysis and History Matching. Presented at the SPE Annual Technical Conference and Exhibition, Houston, Texas, 28-30 September. This paper was supervised by Kamy Sepehrnoori. Jose Sergio de Araujo Cavalcante Filho finished the code development and history matching part. Håkon Høgstøl provided the production data for the fishbone pilot test.

The reservoir size and the positions of the fractures are shown in Figure 5.1. The dimensions of the reservoir are $1000 \times 1500 \times 80$ ft. A horizontal production well is located at the center of the reservoir. All the fracture planes are vertical and have an intersection angle of α with the wellbore. With apertures of 0.015 ft and permeabilities of 10000 md, the fracture conductivities are 150 md-ft. A uniform $200 \times 300 \times 1$ matrix grid is used in this study, and the dimensions of the matrix cells are $5 \times 5 \times 80$ ft. The viscosities of water and oil phases are assumed to be constant and capillary effects are ignored. Peaceman's model is used to calculate the well indices. Corey model is used for the relative permeability curve for matrix cells. For fracture cells, a straight-line relative permeability model is used as shown in Figure 5.2. The detailed reservoir properties and simulation parameters are summarized in Table 5.1.

We rotate the fractures and change the angle α to 90° , 75° , 60° , 45° , and 30° . The fracture half-length is kept constant as 300 ft. The positions of the fractures with different α are shown in Figure 5.3.

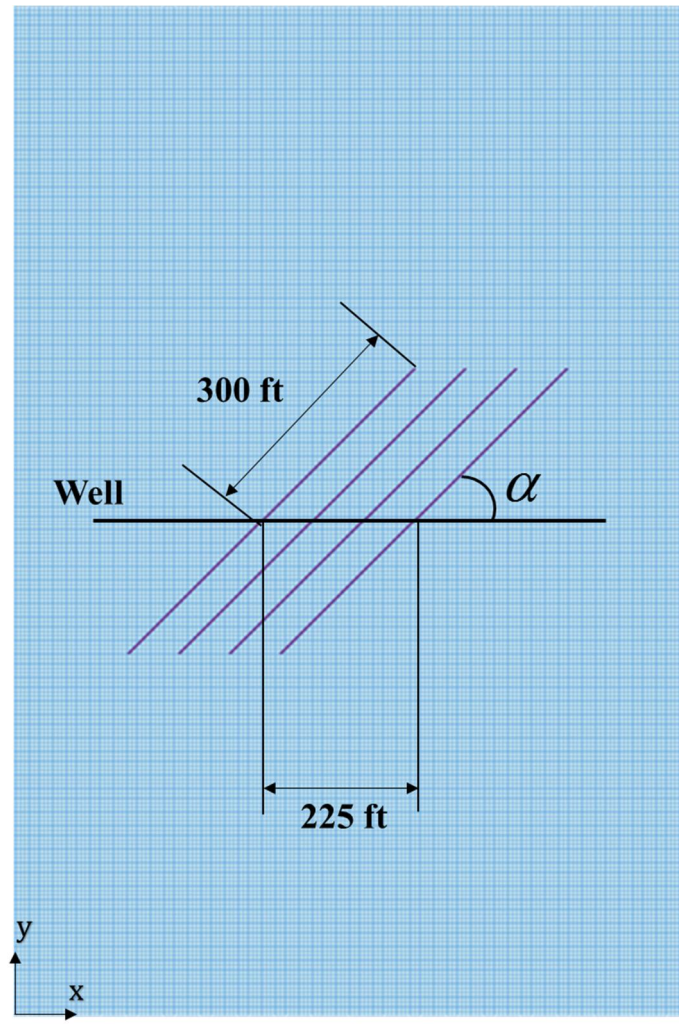


Figure 5.1: A reservoir model with 4 non-orthogonal fractures. Fractures have an angle of α with the X axis.

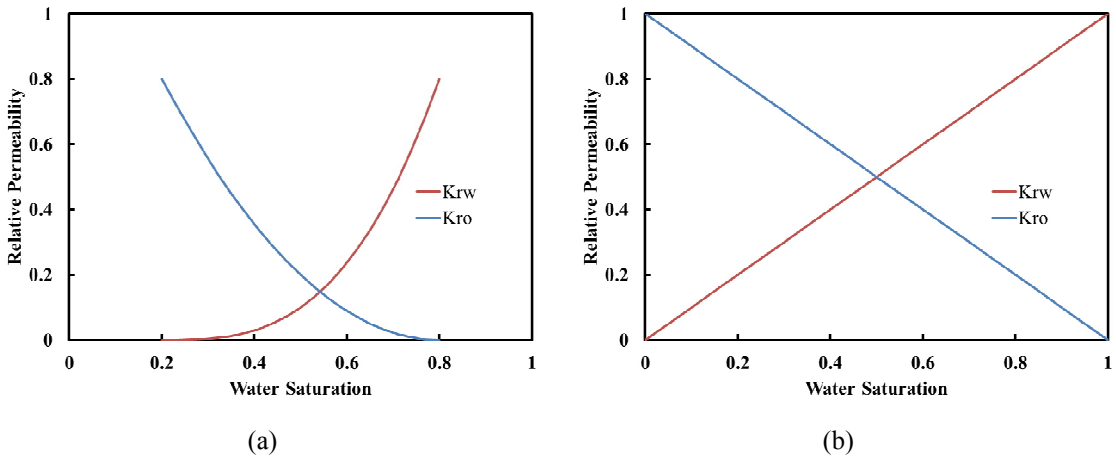


Figure 5.2: Relative permeability curves for (a) matrix cells and (b) fracture cells.

Reservoir Properties		Relative Permeability Curve	
Matrix permeability K _x (md)	0.01	Residual water saturation	0.2
Matrix permeability K _y (md)	0.01	Residual oil saturation	0.2
Matrix permeability K _z (md)	0.01	Water rel. perm. endpoint	0.8
Reservoir porosity	0.15	Oil rel. perm. endpoint	0.8
Reservoir pressure (psi)	3000	Water rel. perm. exponent	3.0
Reservoir Temperature (°F)	120	Oil rel. perm. exponent	2.0
Rock compressibility (psi ⁻¹)	5×10^{-6}	Well Properties	
Water compressibility (psi ⁻¹)	1×10^{-6}	Wellbore radius (ft)	0.5
Oil compressibility (psi ⁻¹)	1×10^{-6}	Well length (ft)	800
Water viscosity (cp)	0.8	Bottomhole pressure (psi)	1000
Oil viscosity (cp)	3.0	Simulation Parameters	
Initial water saturation	0.2	Simulation time (day)	1000
Initial oil saturation	0.8	Maximum time step (day)	3

Table 5.1: Reservoir properties and some of the simulation parameters.

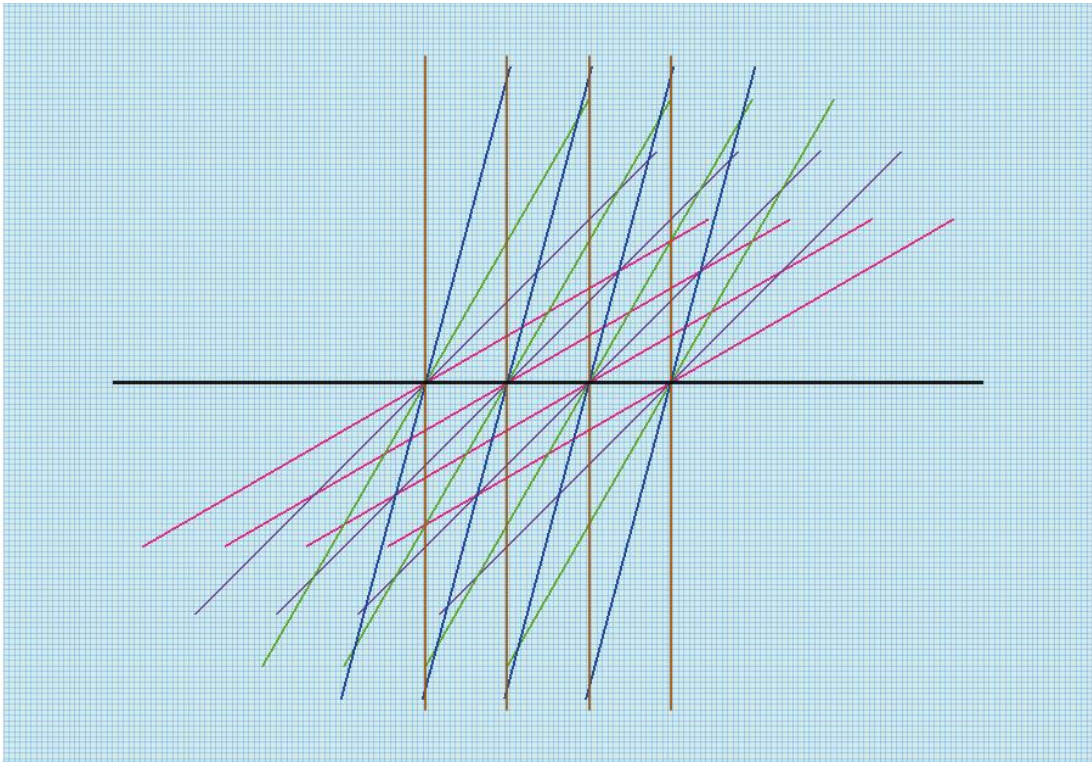


Figure 5.3: Positions of the fractures with different α . Lines with different colors show fractures with different well-fracture intersection angles. Five values of α are chosen in this study ($90^\circ, 75^\circ, 60^\circ, 45^\circ$, and 30°).

Figures 5.4 and 5.5 present the average reservoir pressure and cumulative oil production for all cases. As shown in the figures, when the intersection angle α decreases, the reservoir pressure decreases slower, and the well produces less oil. More details can be found if we look at the oil production rates shown in Figure 5.6. At the very early days (before 7 days), the oil rates are almost the same for all cases. After 7 days, the production rate for $\alpha = 30^\circ$ drops below the rates of other cases. Later, at 11 days, the production rate for $\alpha = 45^\circ$ also decreases compared to the other three cases. As an observation, the smaller α is, the sooner the production rate starts to drop compared to other cases. This can be explained by inter-fracture pressure interference. Since the fractures have very high conductivity, the production rate from the reservoir is mainly

controlled by the flow from matrix to fractures. This type of flow is highly affected by the pressure interference between fractures. Since the distance between fractures in X direction (denoted as D_x) is the same, the distance in the direction perpendicular to the fracture planes (denoted as D_\perp) is proportional to $\sin(\alpha)$, that is

$$D_\perp = D_x \sin(\alpha). \quad (5.1)$$

At the very early time (before 7 days in this study), the pressure fields of adjacent fractures will not affect each other very much. Since the fracture half-length is the same for all cases, the oil production rates are also the same. Later, as the pressure fields of different fractures start to influence each other, the lower α is, the smaller D_\perp is, and the earlier the pressure interference will happen. Also, the smaller D_\perp is, the more pressure interference there will be. Figure 5.7 shows the pressure profiles of different cases after 60 days, where different levels of interference can be easily observed.

At the late time (after 200 days), radial flow becomes dominant as shown in Figure 5.8. We get almost the same oil rates for all cases. Therefore, the differences in cumulative oil production between cases mainly depend on the early stage production. According to Equation 5.1, the pressure interference in early stage is closely related to $\sin(\alpha)$. In order to confirm our analysis, in Figure 5.9, we plot the cumulative oil production vs. $\sin(\alpha)$ after 100 days, 500 days, and 1000 days. As we expect, a linear relationship is observed. The higher $\sin(\alpha)$ is, the less inter-fracture pressure interference we have, and the higher production we get. This linear relationship provides us with a convenient way to estimate the influence of the fracture-well intersection angle on oil production.

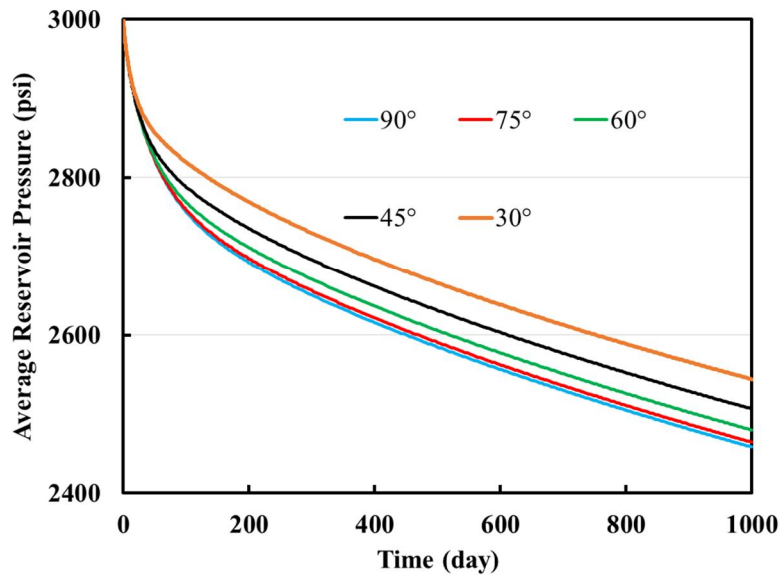


Figure 5.4: Average reservoir pressure for different fracture angles.

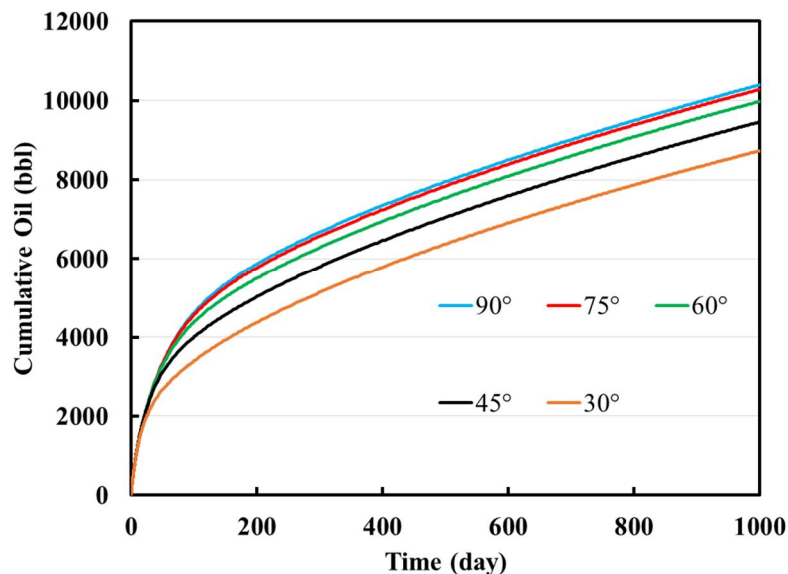


Figure 5.5: Cumulative oil production (reservoir condition) for different fracture angles.

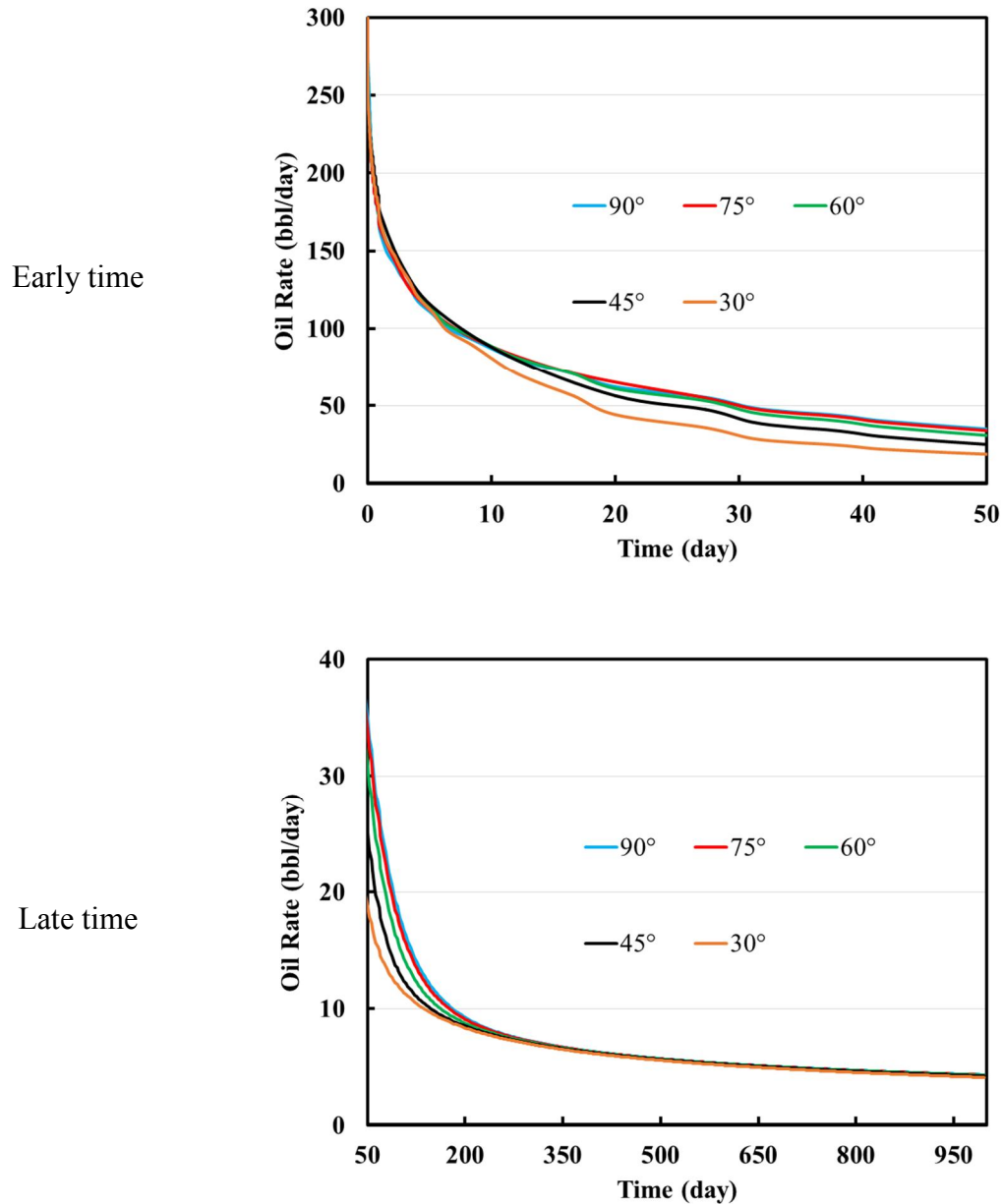


Figure 5.6: Oil production rates (reservoir condition) for different fracture angles at early time and late time.

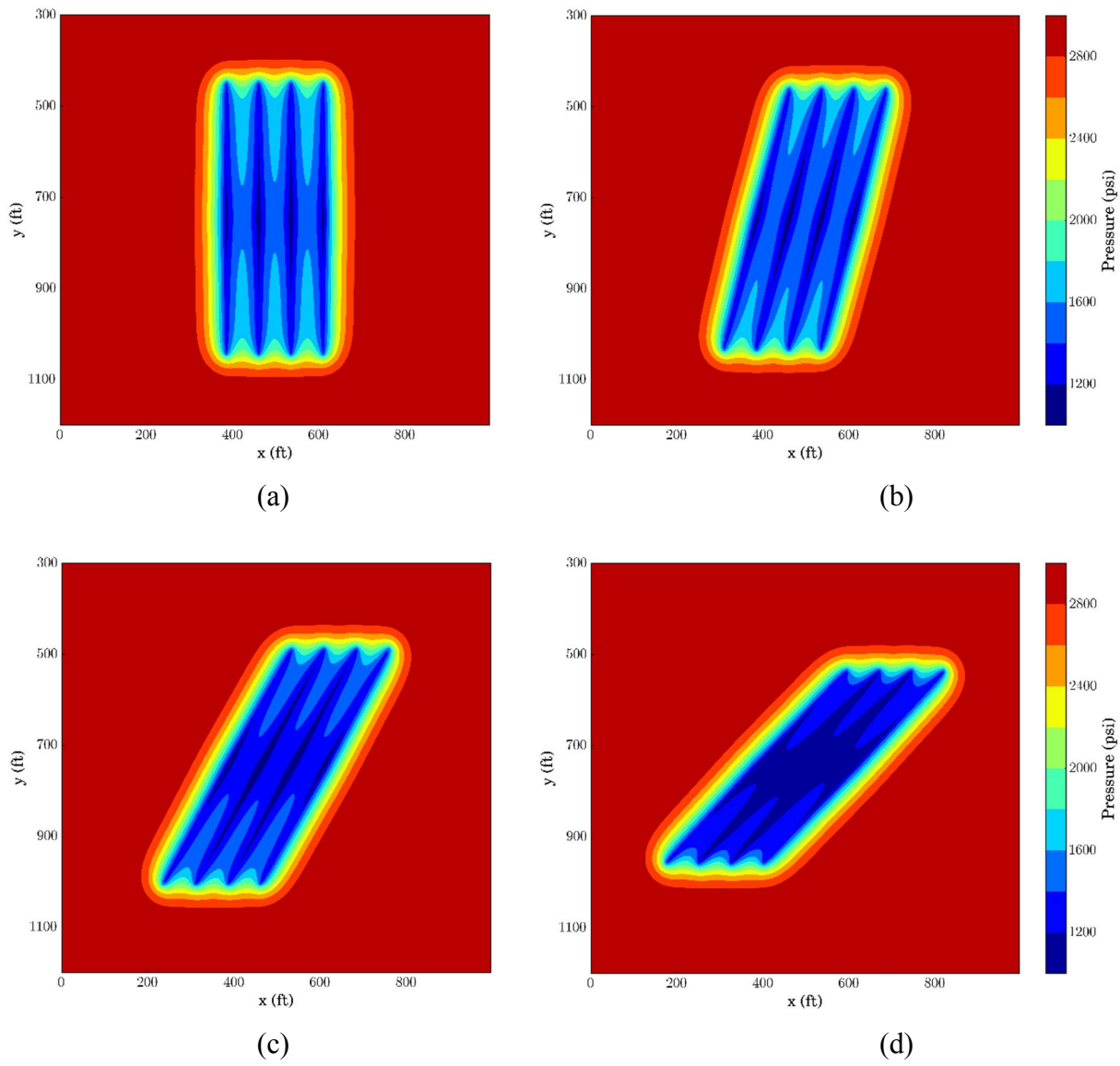
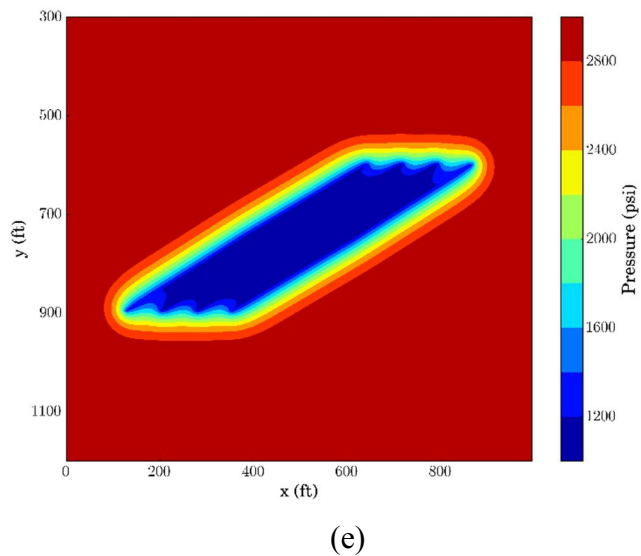


Figure 5.7: Pressure profiles predicted by UTCHEM-EDFM at 60 days for (a) $\alpha=90^\circ$ (b) $\alpha=75^\circ$ (c) $\alpha=60^\circ$ (d) $\alpha=45^\circ$, and (e) $\alpha=30^\circ$.



(e)

Figure 5.7: Continued.

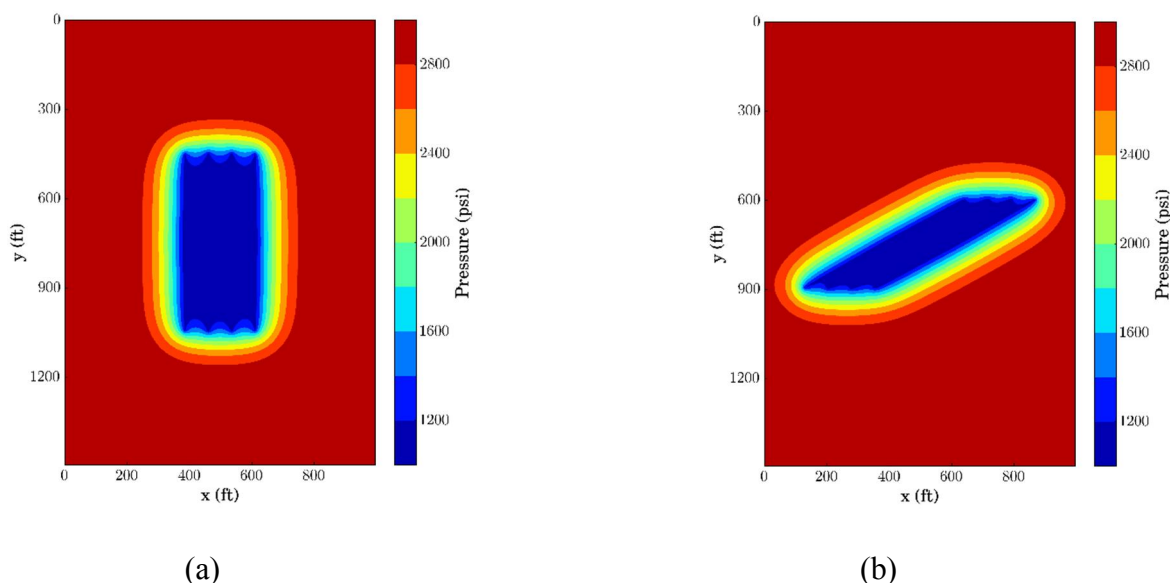


Figure 5.8: Pressure profiles at 200 days for (a) $\alpha=90^\circ$ (b) $\alpha=30^\circ$. Radial flow can be observed.

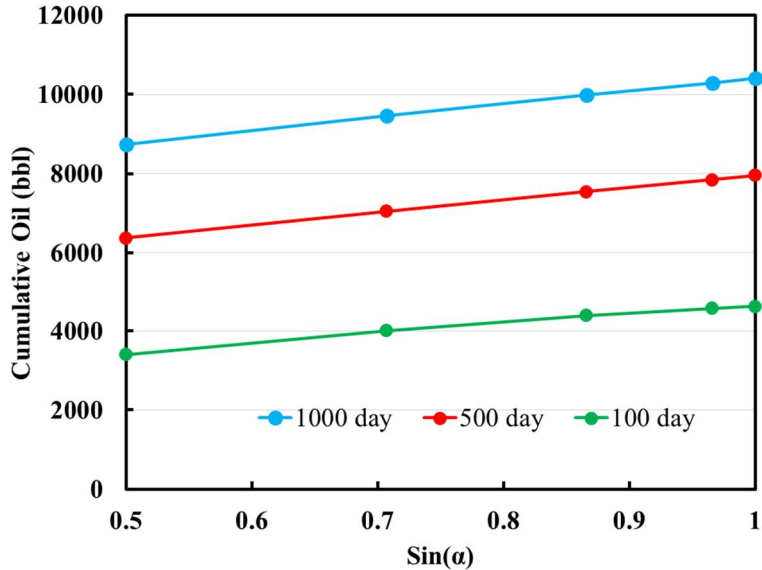


Figure 5.9: Cumulative oil production (reservoir condition) for different α after 100 days, 500 days, and 1000 days.

5.2 WATER FLOODING IN NATURALLY FRACTURED RESERVOIR

There are many reservoirs in the world that are naturally fractured. Natural fractures are considered as conductive pathways in reservoirs and they greatly influence the flow behaviors of the reservoir as the fluids tend to flow along these pathways. Therefore, it is significant to accurately characterize and simulate the natural fracture systems in order that proper production scheme can be made. In this section, we present an example of water flooding in a 3D oil reservoir. For all cases in this study, we use UTCHEM-EDFM.

The reservoir model used in this study is shown in Figure 5.10, with the dimensions of $500 \times 500 \times 40$ ft. It has 8 large-scale fractures with different dip angles ranging from 60° to 90° . The fracture apertures are 0.01 ft and the fracture permeabilities are 3×10^6 md,

giving a fracture conductivity of 3×10^4 md-ft. Figure 5.11 shows the fracture planes in top and slanted views. We put 6 water injectors (with constant injection rate) and 4 producers (with constant bottomhole pressure) in the reservoir. The total injection time is 500 days, and the total injected volume is 0.12 PV. We use a uniform $60 \times 60 \times 2$ matrix grid in the simulation, and the gridblock dimensions are $8.33 \times 8.33 \times 20$ ft.

For relative permeability curves, we use Corey model for the matrix and a straight-line model for fracture cells. Gravity effect is considered in the study and the influence of capillary pressure is not considered. Other reservoir properties and some simulation parameters are presented in Table 5.2.

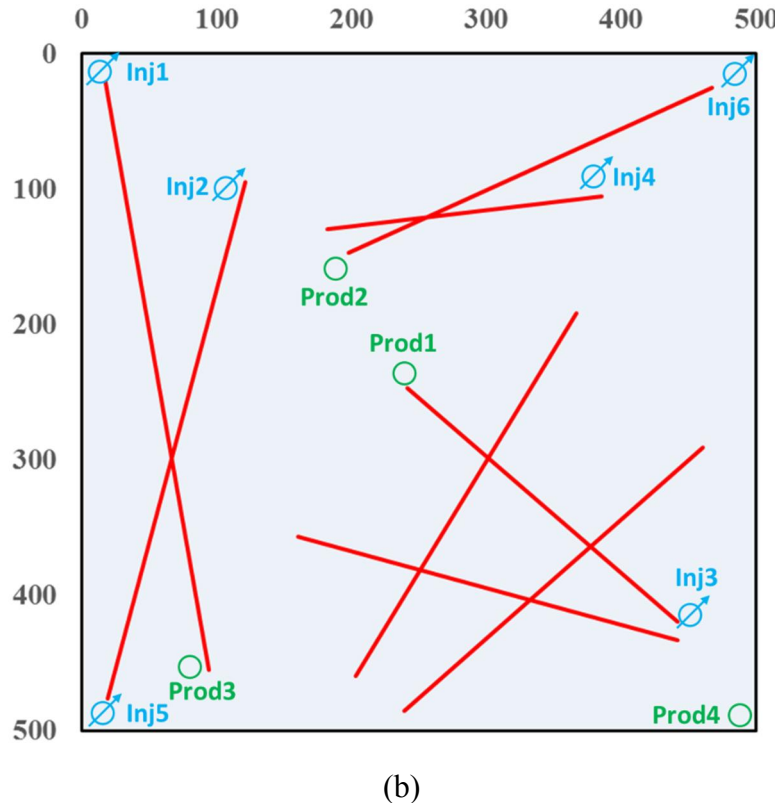
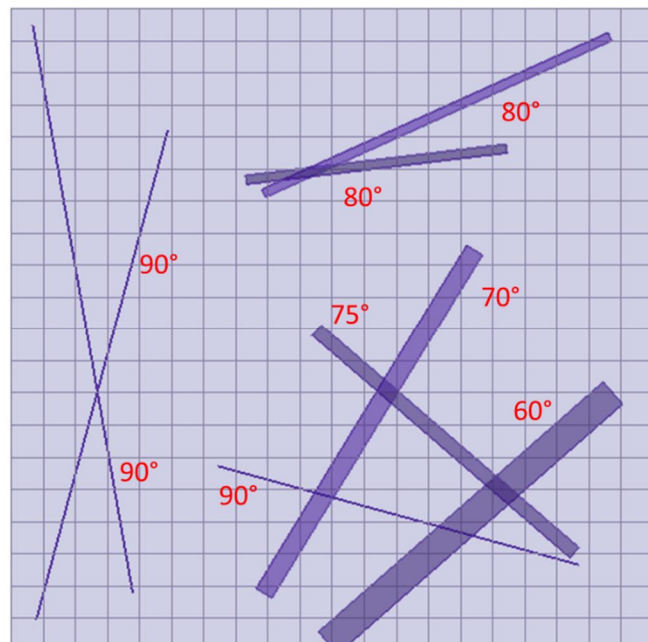
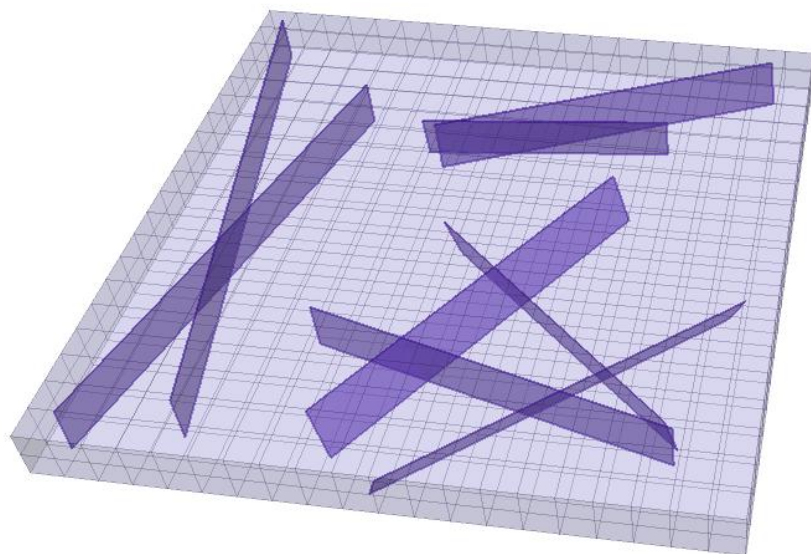


Figure 5.10: A reservoir model with 8 large-scale fractures. The blue circles represent injectors and the green circles represent producers. The fractures are represented by red lines.



(a)



(b)

Figure 5.11: 3D views of the fractures planes. (a) Top view. (b) Slanted view. The numbers in (a) represent the dip angles of the fractures.

Reservoir Properties		Relative Permeability Curve	
Matrix permeability Kx (md)	2.0	Residual water saturation	0.2
Matrix permeability Ky (md)	2.0	Residual oil saturation	0.2
Matrix permeability Kz (md)	0.2	Water rel. perm. endpoint	0.21
Reservoir porosity	0.28	Oil rel. perm. endpoint	0.70
Reservoir pressure (psi)	3000	Water rel. perm. exponent	1.5
Reservoir Temperature (°F)	105	Oil rel. perm. exponent	2.5
Rock compressibility (psi^{-1})	3×10^{-6}	Well Parameters	
Water compressibility (psi^{-1})	1×10^{-6}	Wellbore radius (ft)	0.33
Oil compressibility (psi^{-1})	1×10^{-6}	Well length (ft)	40
Water viscosity (cp)	0.79	Injection rate (bbl/day, injectors)	20
Oil viscosity (cp)	6.3	Injection time (day)	500
Water density (lbm/ft ³)	62.4	Bottomhole pressure (psi, producers)	3000
Oil density (lbm/ft ³)	53.4	Simulation Parameters	
Initial water saturation	0.45	Simulation time (day)	500
Initial oil saturation	0.55	Maximum time step (day)	3

Table 5.2: Reservoir properties and some of the simulation parameters.

For comparison, we also perform a simulation run without considering the fractures. Figure 5.12 shows the oil saturation profiles for both cases. As we can see, the existence of fractures totally changes the flow in reservoir. Without fractures, the injected water moves gradually away from the injectors to sweep the reservoir. When there are large-scale fractures in the reservoir, radial flow can hardly be observed. Instead, the water front moves along the fractures and the regions around the fractures are swept first (low oil saturation in Figure 5.12). Figure 5.13 shows the oil production rates of the four producers in the absence and presence of fractures. For Prod1, Prod2, and Prod3, the large-scale fractures connect them to injectors, resulting in a low reservoir sweep efficiency and low oil production rates compared to the case without fractures. For Prod4, the oil production rate is also negatively affected due to the fact the most of the injected water from Inj3

moves along the fractures and therefore the area around Prod4 is not swept efficiently by water. The results above indicate that the existence of large-scale natural fractures greatly affects the fluid flow during water flooding processes. Fractures serve as highly conductive channels for the injected water and the swept regions will be greatly changed. Therefore, attention must be paid to the positions of fractures in order to make a better water flooding scheme for naturally fractured reservoirs.

The gravity effect can also be observed in Figure 5.14. A higher saturation of water (which is the denser phase) in the bottom layer can be observed than in the top layer.

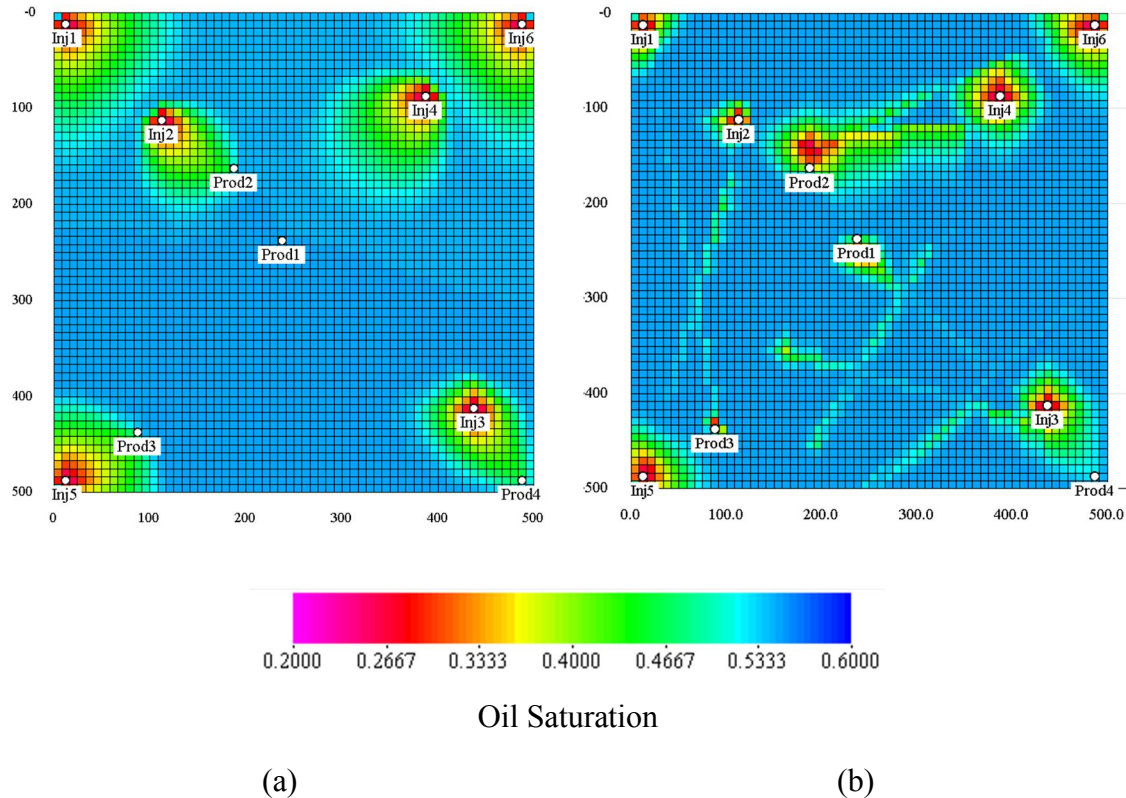


Figure 5.12: Oil Saturation profiles (bottom layer) after 500 days. (a) Without fractures
(b) With fractures.

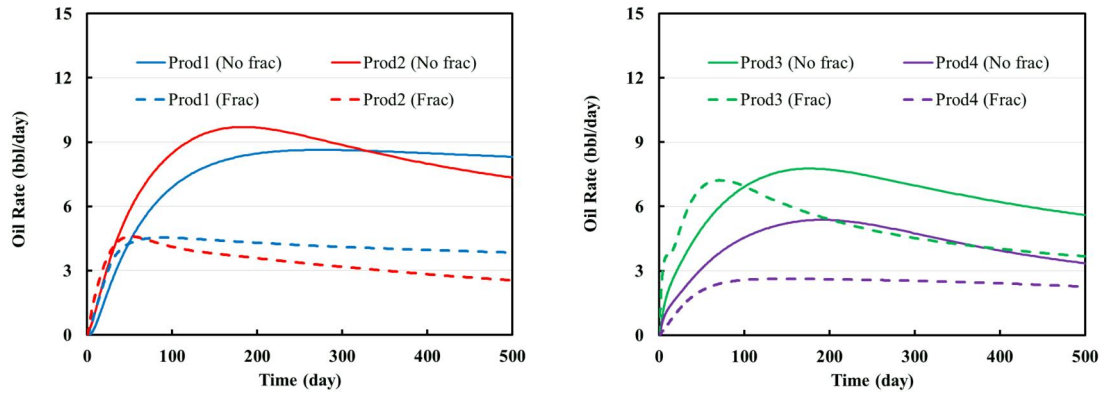


Figure 5.13: Comparison of the producers' oil production rates (reservoir condition) for cases with and without fractures ("Frac" and "No frac").

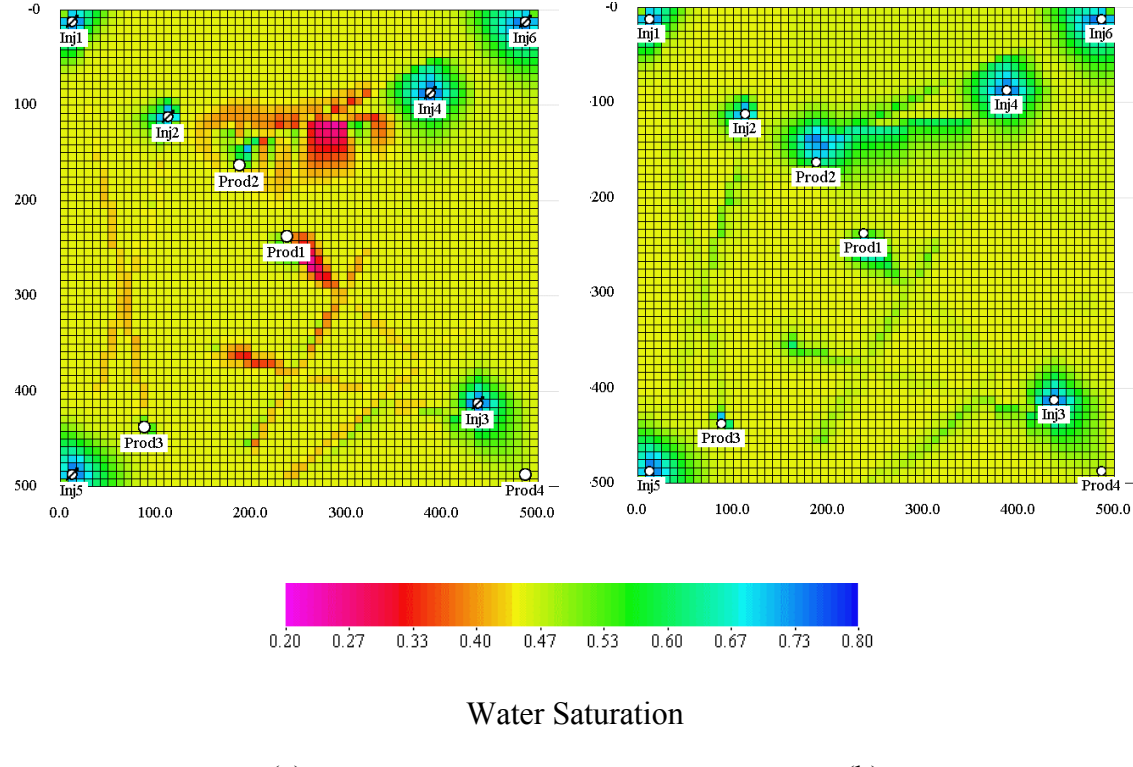


Figure 5.14: Water saturation profiles after 500 days predicted by the EDFM. (a) Top layer (b) Bottom layer.

We perform two additional simulations with uniform $20 \times 20 \times 2$ and $100 \times 100 \times 2$ matrix grids to investigate the influence of grid resolution on the EDFM. Figure 5.15 shows the oil production rates for these cases and Figure 5.16 shows the oil saturation profiles for different grid resolutions. As can be seen, in the $20 \times 20 \times 2$ grid, the gridblock size is not small enough to accurately simulate the water flooding process. In addition, the results using $60 \times 60 \times 2$ and $100 \times 100 \times 2$ grids are quite similar, indicating that the EDFM can maintain the accuracy for water flooding simulations as long as appropriate gridblock size is used.

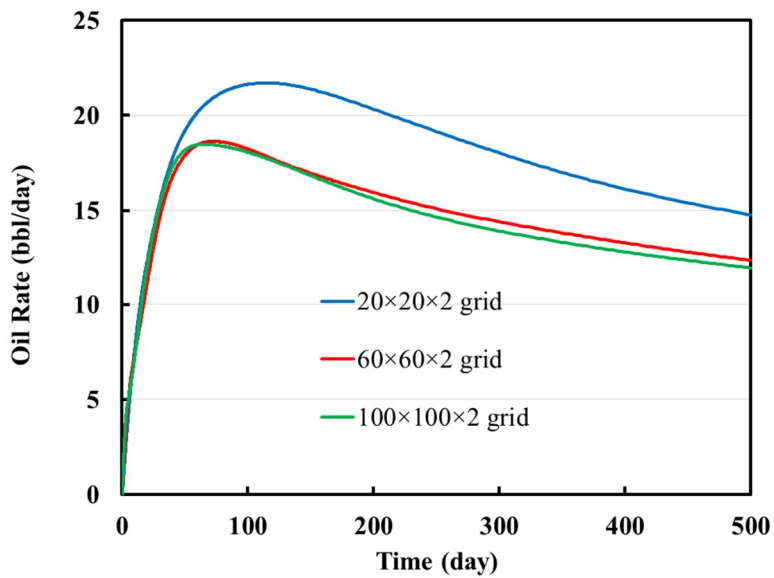


Figure 5.15: Oil production rates (reservoir condition) predicted by the EDFM using different grid resolutions.

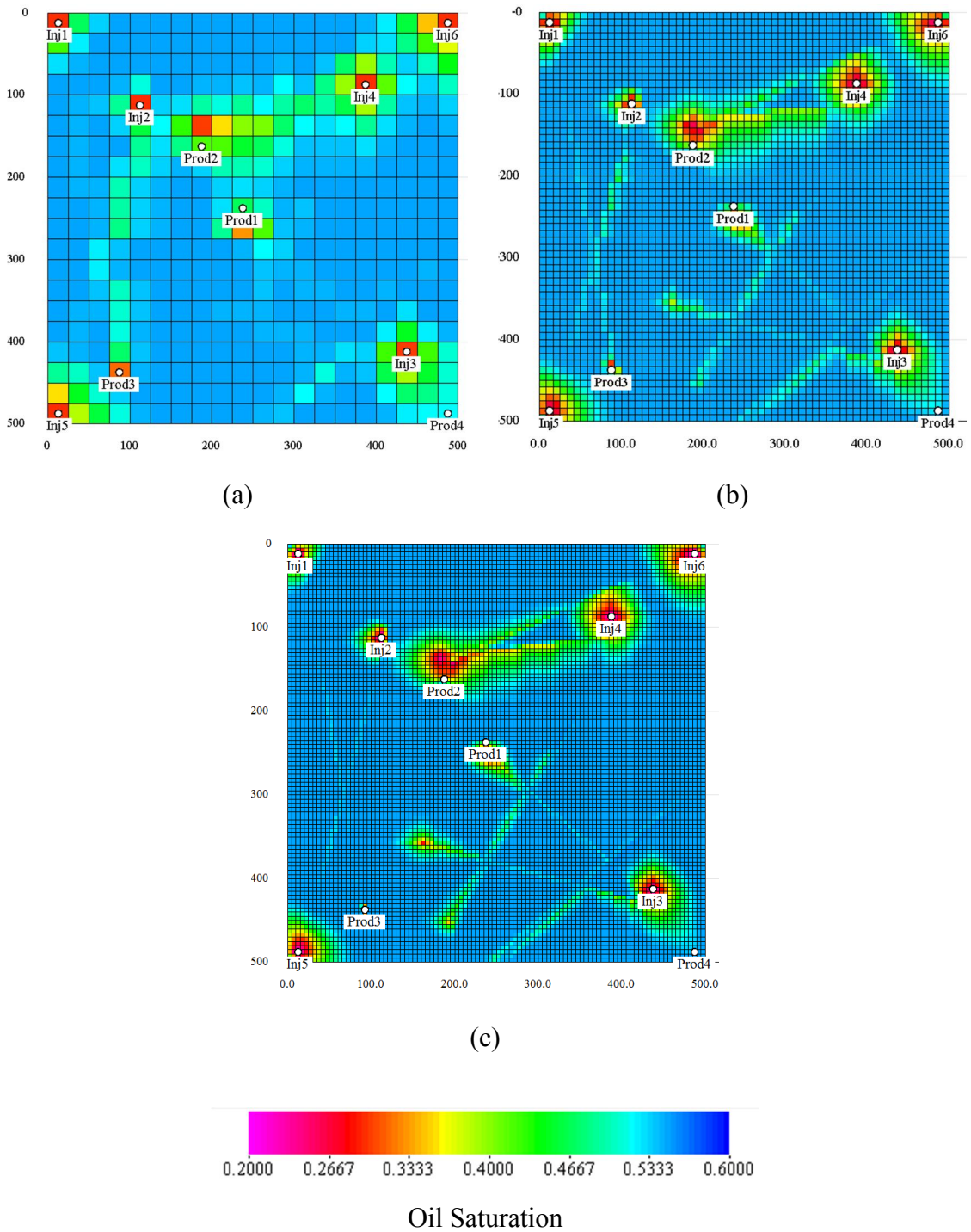


Figure 5.16: Oil saturation profiles (bottom layer) after 500 days predicted by the EDFM with (a) $20 \times 20 \times 2$ grid (b) $60 \times 60 \times 2$ grid (c) $100 \times 100 \times 2$ grid.

We also investigate the impact of the fracture relative permeability curve. For the previous study, we assumed a straight-line model for fracture cells. Porte et al. (2005) showed that for a water-oil system, if there is water injected into fractures, a non-straight-line fracture relative permeability curve should be used. Here we perform an additional simulation run, where the relative permeability curve for fracture cells is the same as the one for matrix (Corey model). Figure 5.17 shows the oil saturation profiles after 500 days and Figure 5.18 shows the oil production rates for both cases. It can be observed that the fracture relative permeability curve has a great impact on oil production rate. When using Corey model for fracture relative permeability, the oil production rate has a great increase compared to the case using straight-line model. This result can be explained using the relative mobility curves in Figure 5.19. In Figure 5.19, we compare the relative mobility curves for both simulation runs. For water saturation around 0.45 (the initial water saturation), in straight-line model, the water phase has a much higher relative mobility than the oil phase; however, in Corey model, the water and oil relative mobilities have close values. Therefore, considering the flow competence between the two phases, in the latter case, there will be more oil flowing in the fractures, resulting in more oil production.

This example shows the importance of fracture relative permeability curves for the simulation results. With large-scale natural fractures in reservoirs, the overall production is to some degree determined by the flow in fractures. Therefore, attention needs to be paid to the choice of fracture relative permeability model to make an accurate simulation.

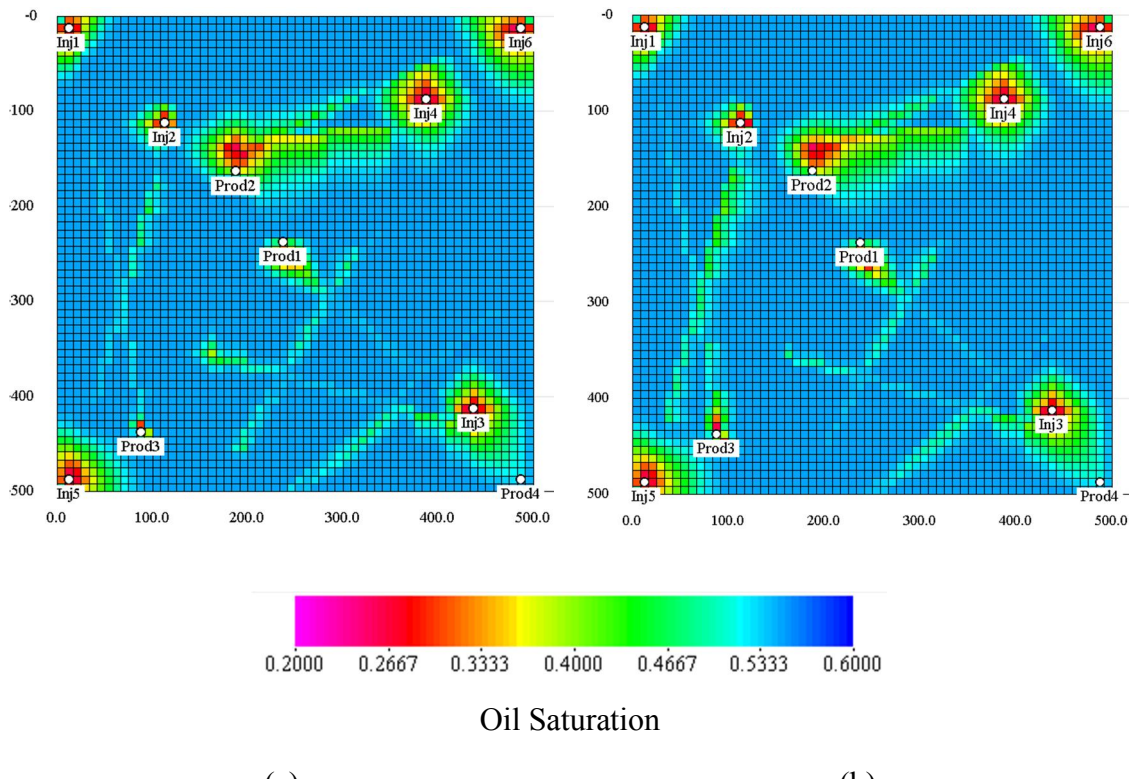


Figure 5.17: Oil saturation profiles (bottom layer) after 500 days predicted by the EDFM using different fracture relative permeability models. (a) Straight-line model (b) Corey model (the same as matrix).

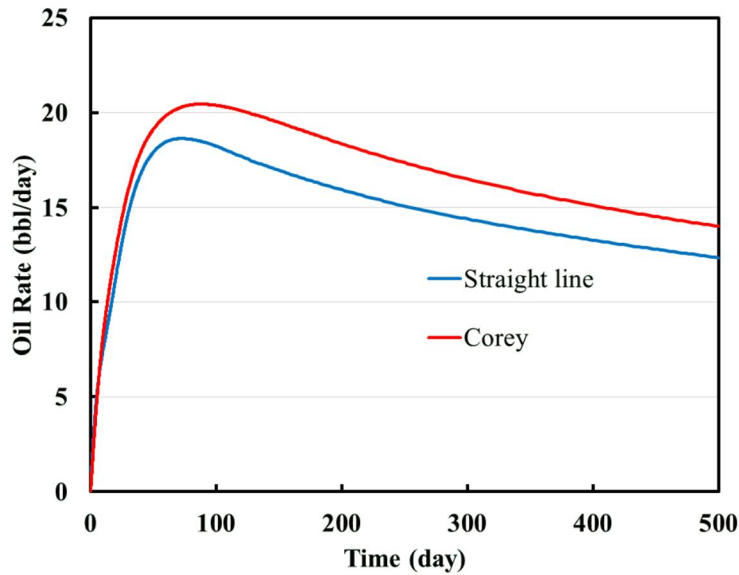


Figure 5.18: Oil production rates (reservoir condition) for different fracture relative permeability models.

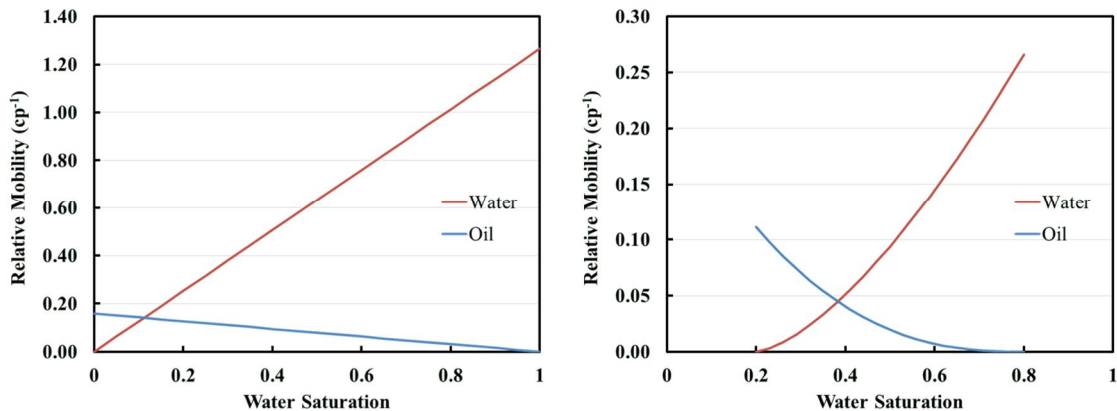


Figure 5.19: Relative mobility for different relative permeability models. (a) Straight-line model (b) Corey model (the same as matrix).

5.3 FISHBONE WELL SIMULATION WITH THE EDFM

5.3.1 Multi-lateral Well Stimulation Technology

Fishbone well is a multi-lateral well stimulation technology designed for low-permeability reservoirs. In a fishbone well, the system creates a series of open holes in sequence off a main horizontal well as a part of completion (as shown in Figure 5.20). These open holes are called laterals, and they provide vertical flow paths in the reservoir that are similar to hydraulic fractures, improve the reservoir connectivity to the well and increase the well productivity index.

Recently, Freyer and Shaoul (2011) and Rice et al. (2014) described a stimulation technology to create fishbone laterals through acid injection, known as “Fishbones”. In their technology, four open holes are created in each sub, with a length of up to 40 ft and a diameter of 0.5 in to 0.75 in. Figure 5.21 shows the stimulation system of this technology. To create the open holes, in each sub, four 40-ft long needles are radially distributed around the casing at 90° phasing. These needles can be precisely located across pre-selected intervals. During stimulation, the acid is pumped through the needles and the formation ahead of the needle is jetted away to form the holes. As shown in Figure 5.21, the needles exit the sub at an angle of 40° relative to the wellbore but the final angle of the laterals is 90° due to the bending of the needles.

In pilot tests, this technology has been applied to a coalbed methane reservoir and a carbonate reservoir. In the first pilot test in Carbonate reservoir (at the Austin Chalk Formation), the Fishbones stimulation system was successfully installed in a horizontal well and 60 fishbone laterals were created within 5 hours (Rice et al. 2014). The test proves 30 times increase in well productivity index.



Figure 5.20: A 3D visualization of the Fishbone well (<http://www.fishbones.as>).

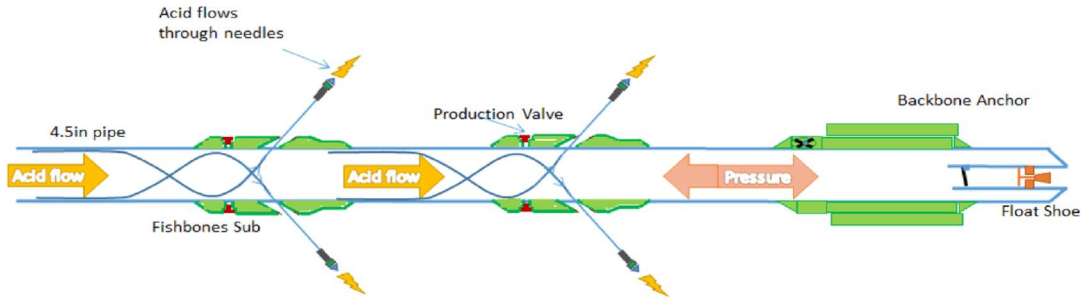


Figure 5.21: A schematic for the Fishbones stimulation system (Carvajal et al. 2015).

Fishbones is a promising as well as a novel well stimulation technology. When compared to traditional acid stimulation methods, it eliminates the uncertainties in acid treatment, guaranteeing an efficient distribution of stimulation solution (Carvajal et al. 2015). If compared to hydraulic fracturing, the Fishbones technology avoids the usage of large amounts of water and sand, which leads to a relatively low cost. It overcomes two problems in hydraulic fracturing, including the uncertain fracture propagation and production decline due to fracture closure. In addition, less fluid is used in this technology; therefore, the risks of groundwater containment and stimulation fluid flow-back are reduced (Freyer and Shaoul 2011).

Some research has been conducted to model the novel well geometry of fishbone well and investigate its influence on production using fine-grid models or analytical models (Freyer and Shaoul 2011; Yu et al. 2009; Maricic et al. 2008). In our work, we have shown the accuracy and flexibility of the EDFM. In addition, the EDFM can be easily incorporated into history matching or sensitivity analysis frameworks, which may facilitate a comprehensive study of this well stimulation technology. Therefore, in this section, we make an effort to modify the formulations in the EDFM approach in order that the fishbone laterals can be modeled as equivalent fractures in the EDFM and the influence of this new well geometry can be investigated.

5.3.2 Modeling Fishbones Using the Modified EDFM Formulations

In the EDFM, the fractures are modeled as planes and the flow communications associated with fractures are modeled through transport indices between NNC pairs. Since the fishbone laterals have different geometries from fractures, we modify the formulations of transport index calculations in the EDFM to model fishbone laterals as equivalent fractures as shown in Figure 5.22.

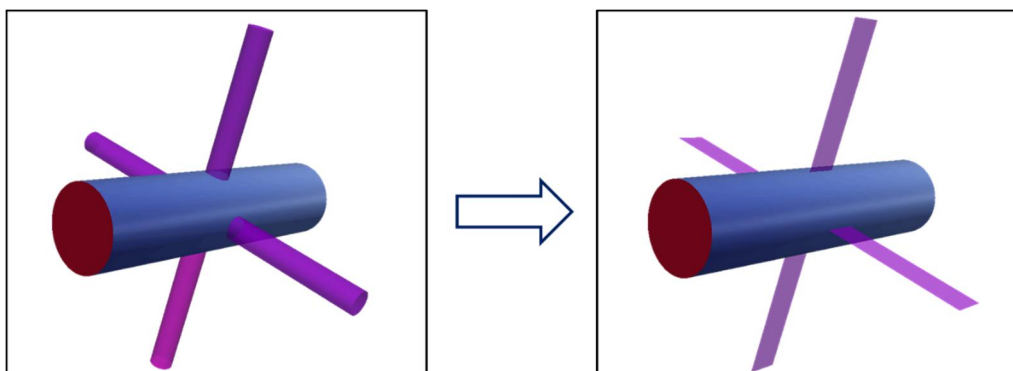


Figure 5.22: Illustration of the fishbone modeling methodology. We model the fishbone laterals as equivalent fractures in this study.

The equivalent fractures should have the same flow properties as the fishbone laterals. First, the length of the equivalent fractures is set the same as the fishbone laterals. Then, to determine the aperture and height of the equivalent fractures, we use a relationship to maintain the cross sectional area of the fishbone laterals

$$w_f \times h_f = \frac{\pi D_{hole}^2}{4}, \quad (5.2)$$

where w_f and h_f are the aperture and height of the equivalent fractures, respectively. D_{hole} is the diameter of the fishbone open hole. In our study, we fix w_f as 1 ft; therefore

$$h_f \propto \frac{\pi D_{hole}^2}{4}. \quad (5.3)$$

The calculations of the transport indices associated with the equivalent fractures are explained in Figure 5.23. Analogous to the fracture segments in the EDFM, the fishbone laterals are cut into lateral segments by matrix cell boundaries. For the flow communication between lateral segments in an individual fishbone lateral (similar to NNC Type II in the EDFM), Hagen-Poiseuille equation is used to calculate the transmissibility factor

$$T_{seg} = \frac{\pi D_{hole}^4}{128 d_{L-L}}, \quad (5.4)$$

where D_{hole} is the diameter of the fishbone open hole and d_{L-L} is the distance between the centers of two neighboring lateral segments.

For the fishbone-well flow, the equivalent well index is

$$WI = \frac{k A_{hole}}{d_{L-W}}, \quad (5.5)$$

where k is the permeability of the open hole, which is evaluated using Hagen-Poiseuille equation as

$$k = \frac{D_{hole}^2}{32}, \quad (5.6)$$

where A_{hole} is the area of the open hole, $A_{hole} = \frac{\pi D_{hole}^2}{4}$, and d_{L-W} is the distance between the center of the lateral segment to the wellbore. Therefore,

$$WI = \frac{kA_{hole}}{d_{L-W}} = \frac{\pi D_{hole}^4}{128d_{L-W}}. \quad (5.7)$$

For the flow from matrix to fishbone laterals (similar to NNC Type I in the EDFM), we use a similar formulation as that for matrix-well flow. In Peaceman's model, if we assume that the axis of well is in X direction, the well index is

$$WI = \frac{2\pi\sqrt{k_y k_z} \Delta x}{\ln(r_o / r_w)}, \quad r_o = 0.28 \frac{(k_y \Delta z^2 + k_z \Delta y^2)^{1/2}}{k_y^{1/2} + k_z^{1/2}}, \quad (5.8)$$

where k_y and k_z are the matrix permeability in Y and Z direction, respectively. r_w is the wellbore radius and r_o is the equivalent radius. Δx , Δy , and Δz are the wellblock dimensions in X, Y, and Z directions, respectively. Since the fishbone laterals have similar shape as the wellbore, similar formulation can be applied to calculate the matrix-fishbone flow transport index. If the axis of the horizontal well is in X direction, the axes of the fishbone laterals will be in Y and Z directions, respectively. For fishbone laterals in Y direction, we use

$$T_{M-L,y} = \frac{2\pi\sqrt{k_x k_z} \Delta L_{fb}}{\ln(r_o / r_f)}, \quad r_o = 0.28 \frac{(k_x \Delta z^2 + k_z \Delta x^2)^{1/2}}{k_x^{1/2} + k_z^{1/2}}, \quad (5.9)$$

and similarly, for fishbone laterals in Z direction, we use

$$T_{M-L,z} = \frac{2\pi\sqrt{k_x k_y} \Delta L_{fb}}{\ln(r_o / r_L)}, \quad r_o = 0.28 \frac{(k_x \Delta y^2 + k_y \Delta x^2)^{1/2}}{k_x^{1/2} + k_y^{1/2}}, \quad (5.10)$$

where $T_{M-L,y}$ and $T_{M-L,z}$ are the corresponding transmissibility factors, ΔL_{fb} and r_L are the length and radius of the fishbone lateral segment, respectively, and k_x , k_y , and k_z are the corresponding matrix permeabilities.

The new formulations are used in the modified EDFM for the transmissibility factor calculations in order that the fishbone well geometry can be properly modeled in the EDFM.

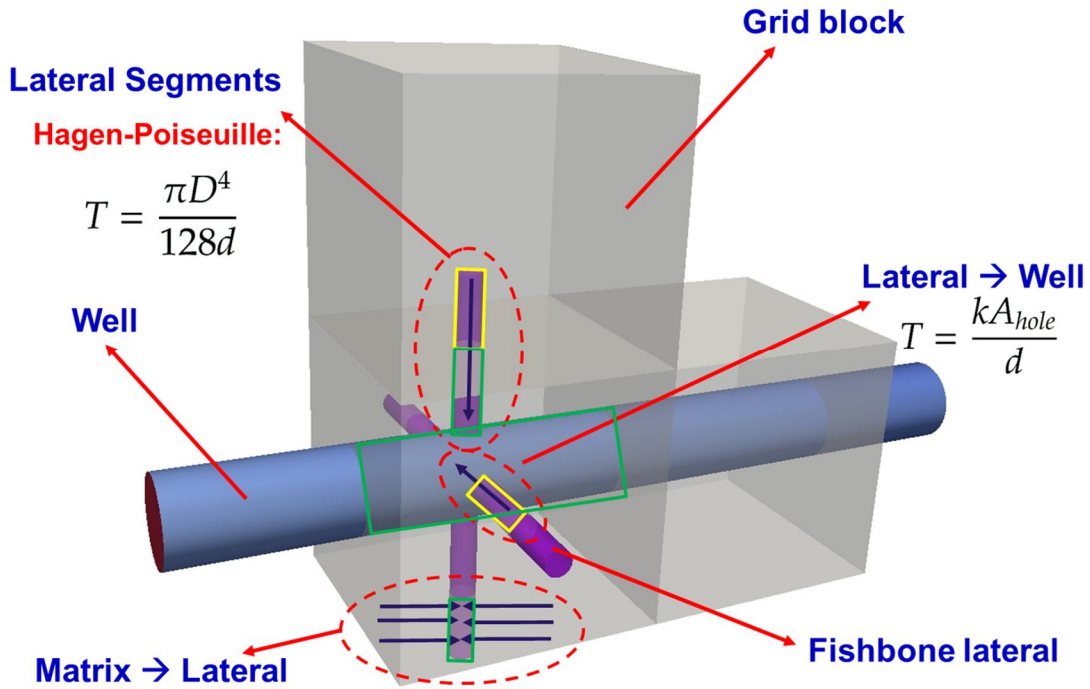


Figure 5.23: Explanation of the transport index calculations in the fishbone well modeling.

5.3.3 Multi-Branch Well Method

After introducing our new formulations for the EDFM, we verified our model against another approach to modeling fishbone wells, that is, the multi-branch well method.

In the EDFM, the fishbone laterals are regarded as equivalent fractures. However, they can also be considered as part of the well. In the multi-branch well method, the laterals are considered as “branches” of the main horizontal wellbore. Therefore, the methods to model the well in reservoir simulation can also be used to model the laterals.

In traditional reservoir simulators, the direction of the wellbore is defined as “X”, “Y”, or “Z”. However, as shown in Figure 5.20, in a fishbone well, the axes of “branches” (fishbone laterals) have different directions from the main wellbore. Therefore, the direction of the fishbone wellbore cannot be defined by a single “X”, “Y”, or “Z”. In the multi-branch method, this difficulty can be resolved by adding a “direction factor” in the well index calculations for the gridblocks containing branches. Assuming Peaceman’s model is applied, if the main horizontal wellbore is in X direction and if we define the wellbore direction as “X”, then for a gridblock with a Y direction branch, the “direction factor” is

$$DF_{y,x} = \frac{2\pi\sqrt{k_x k_z} \Delta y}{\ln(r_{oy}/r_f)} / \frac{2\pi\sqrt{k_y k_z} \Delta x}{\ln(r_{ox}/r_w)},$$

$$r_{oy} = 0.28 \frac{(k_x \Delta z^2 + k_z \Delta x^2)^{1/2}}{k_x^{1/2} + k_z^{1/2}},$$

$$r_{ox} = 0.28 \frac{(k_y \Delta z^2 + k_z \Delta y^2)^{1/2}}{k_y^{1/2} + k_z^{1/2}}, \quad (5.11)$$

where Δx , Δy , and Δz are the gridblock dimensions, r_f is the radius of the fishbone lateral, r_w is the wellbore radius, and k_x , k_y , k_z are the matrix permeabilities in different directions. As a correction factor, $DF_{y,x}$ can be directly input into simulators as

a multiplier (for example, “ff” in CMG) for the original well index calculated by Peaceman’s model. Similar equations can also be derived for $DF_{z,x}$.

It should be noted that when $\Delta x = \Delta y = \Delta z$, $r_f = r_w$, and $k_x = k_y = k_z$, $DF_{y,x} = DF_{z,x} = 1$, then no correction is needed. Otherwise, missing of these correction factors will lead to inaccuracy in the simulation results.

If a gridblock contains both a segment of well and fishbone lateral segments, the corresponding well indices will be added together to get an effective well index for that gridblock.

In the next section, we present case studies to compare both models to verify our modified EDFM formulations.

5.3.4 Comparison of the Modified EDFM and the Multi-Branch Well Method

In this section, we perform several case studies using both models to verify the modified EDFM formulations. Figure 5.24 shows the reservoir model we use in this study. The dimensions of the reservoir are $1560 \times 1000 \times 100$ ft. A horizontal production well is located at the center of the reservoir (Layer 5) with 60 fishbone laterals. We discretize the matrix using a uniform $78 \times 50 \times 10$ matrix grid and the dimensions of the matrix cells are $20 \times 20 \times 10$ ft.

The viscosities of water and oil phases are assumed to be constant. The initial water saturation is equal to the residual water saturation; therefore, oil is the main flowing phase. Peaceman’s model is used in the well productivity index calculation. We ignore the influence of capillary pressure and gravity in this study and Corey model is used for matrix relative permeability curve. For fishbone cells, a straight-line relative permeability model

is used. Detailed reservoir properties and simulation parameters are summarized in Table 5.3.

In order to evaluate the influence of permeability anisotropy on fishbone well performance, we performed two case studies, one using an isotropic reservoir and another using an anisotropic reservoirs. In the former case, the reservoir has a permeability of 1 md in all directions. In the latter case, the permeability in Z direction is 10 times lower than that in X and Y directions.

The number of fishbone subs is also varied to investigate its influence. In this study we selected four cases, where the numbers of fishbone subs are 1, 2, 4, and 15, respectively. Correspondingly, the numbers of fishbone laterals are 4, 8, 16, and 60, respectively. The positions of the fishbone laterals for different scenarios are shown in Figure 5.25. For the case with 60 laterals, the distance between adjacent subs is 40 ft. We assume that the length and radius of the fishbone laterals are 40 ft and 0.033 ft, respectively, which are typical values for the Fishbones technology. Furthermore, for simplicity, we set the radius of the main wellbore to also 0.033 ft, making the direction factors easier to calculate. The simulator we used for the EDFM approach is UTCHEM-EDFM and the one for multi-branch well method is CMG-IMEX.

Figures 5.26 and 5.27 show the cumulative oil production predicted by two models for the isotropic case and anisotropic case, respectively. The close agreement confirms the accuracy of the modified EDFM formulations. Figure 5.28 presents the pressure profiles after 5 days predicted by both models as a further confirmation.

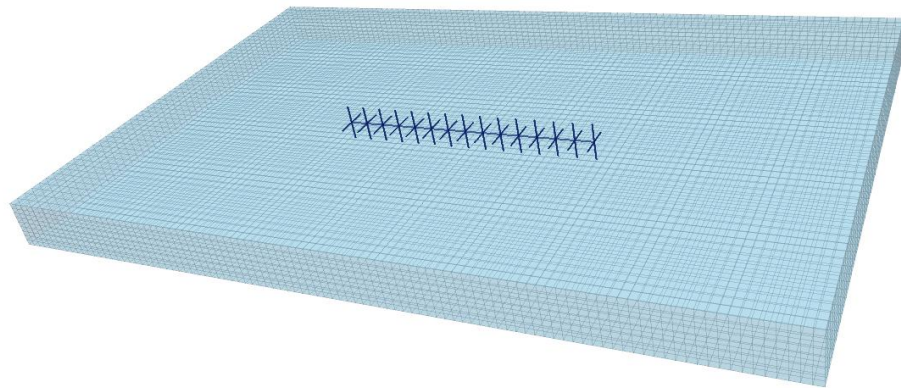
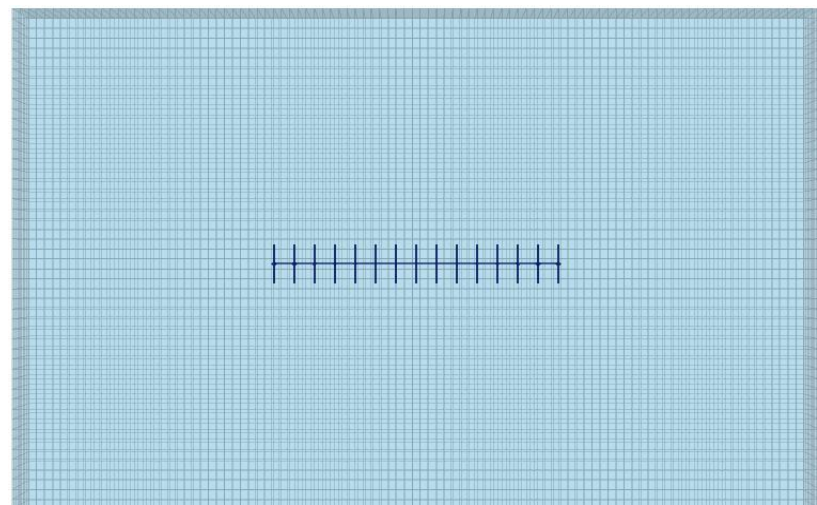


Figure 5.24: Reservoir dimensions and location of the horizontal well and fishbone subs.

Reservoir Properties		Relative Permeability Curve	
Matrix permeability Kx (md)	1.0	Residual water saturation	0.2
Matrix permeability Ky (md)	1.0	Residual oil saturation	0.2
Matrix permeability Kz (md)	1.0 0.1	Water rel. perm. endpoint	0.8
Reservoir porosity	0.3	Oil rel. perm. endpoint	0.7
Reservoir pressure (psi)	3000	Water rel. perm. exponent	4.0
Reservoir Temperature (°F)	60	Oil rel. perm. exponent	2.0
Rock compressibility (psi^{-1})	1×10^{-6}	Well Properties	
Water compressibility (psi^{-1})	0.0	Wellbore radius (ft)	0.033
Oil compressibility (psi^{-1})	1×10^{-6}	Well length (ft)	560
Water viscosity (cp)	0.8	Bottomhole pressure (psi)	2800
Oil viscosity (cp)	1.0	Simulation Parameters	
Initial water saturation	0.2	Simulation time (day)	180
Initial oil saturation	0.8	Maximum time step (day)	1

Table 5.3: Reservoir properties and some of the simulation parameters.

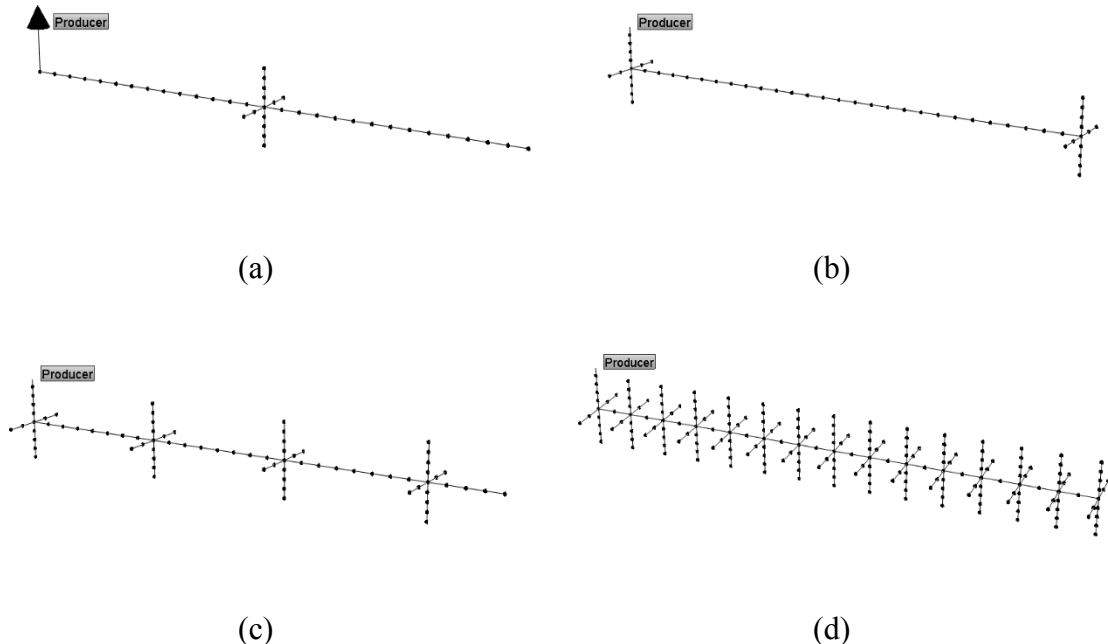


Figure 5.25: Positions of the fishbone subs for cases with (a) 4 fishbone laterals (b) 8 fishbone laterals (c) 16 fishbone laterals and (d) 60 fishbone laterals.

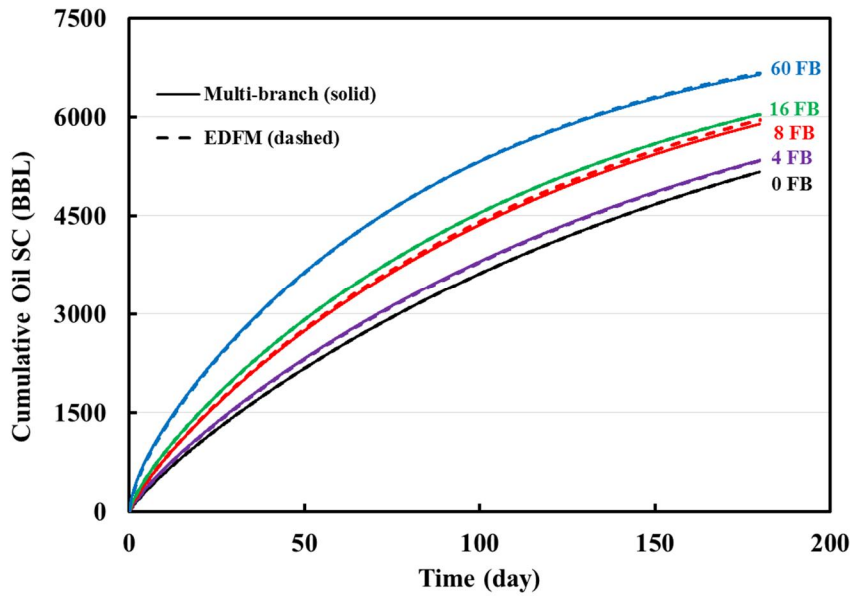


Figure 5.26: Comparison of cumulative oil production (reservoir condition) between multi-branch approach and the EDFM approach for the isotropic case. Different curves show results for different numbers of fishbone laterals.

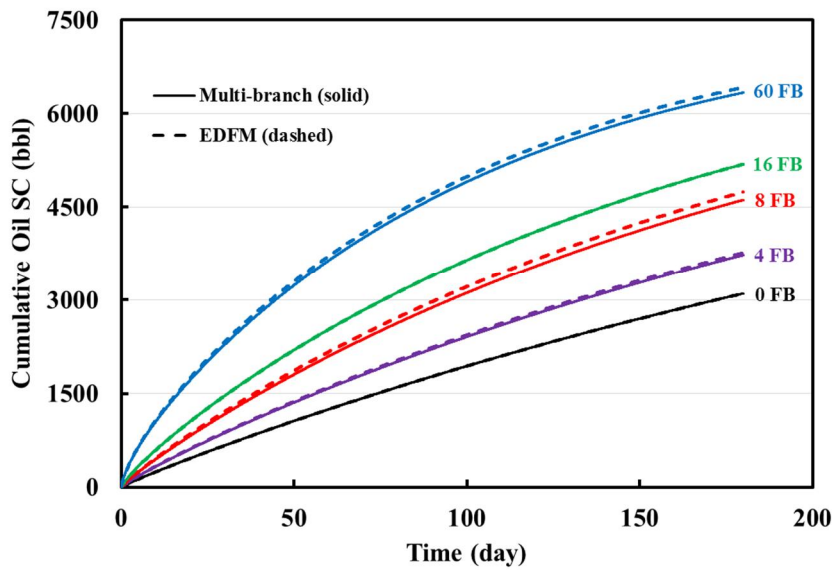
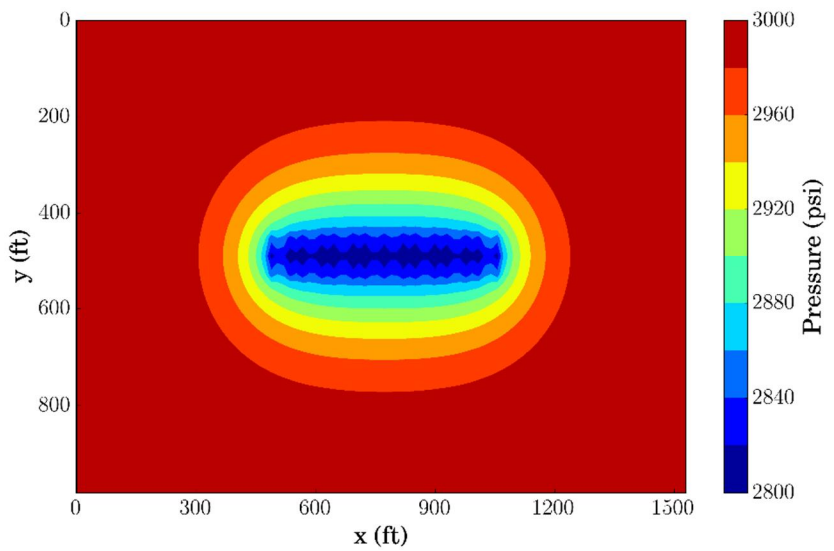
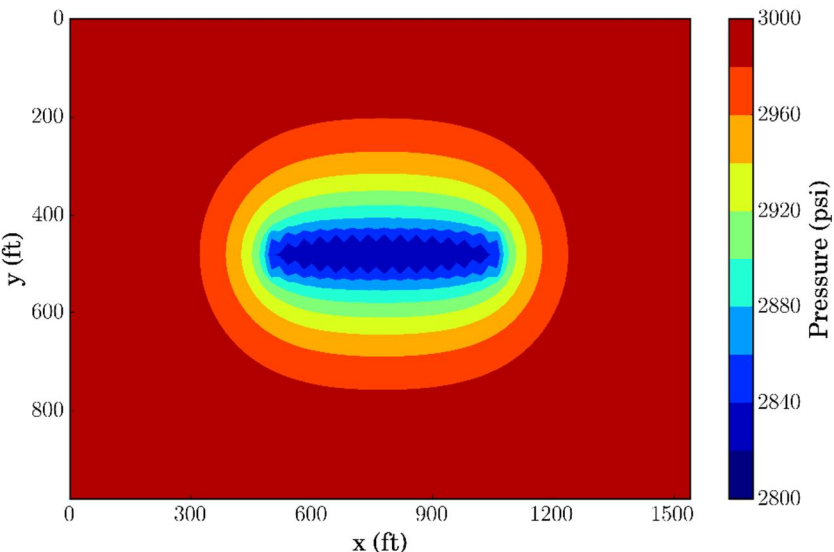


Figure 5.27: Comparison of cumulative oil production (reservoir condition) between multi-branch approach and the EDFM approach for the anisotropic case. Different curves show results for different numbers of fishbone laterals.



(a)



(b)

Figure 5.28: Pressure profiles after 5 days predicted by (a) Modified EDFM (b) Multi-branch method.

5.3.5 Simulation result analysis

Based on the simulation results, there are some interesting observations related to the performance of fishbone wells.

5.3.5.1 Fishbone Lateral Number Impact

For both isotropic case and anisotropic case, an increase of fishbone lateral number (n_L) results in more reservoir contact area, which brings more oil production. However, the additional production brought by each lateral (ΔCOP_L , defined by Equation 5.12) will not always increase. Figure 5.29 shows the variation of ΔCOP_L with n_L . For low n_L , the impact of each lateral is determined by the pressure interference between the lateral and the main horizontal well. Therefore, when we move the laterals from the middle of the wellbore (for case $n_L = 4$) to the ends (for case $n_L = 8$), each lateral contributes more to oil production. As n_L further increases to 16 or 60, the spacing between laterals decreases, and the inter-lateral pressure interference begins to take effect, leading to low ΔCOP_L .

$$\Delta COP_L = \frac{COP|_{n_L} - COP|_0}{n_L}, \quad (5.12)$$

where $COP|_{n_L}$ is the cumulative oil production for a case with n_L laterals, and $COP|_0$ is the cumulative oil production for a case with no fishbone lateral.

Based on the above analysis, the positions and spacing of fishbone laterals should be carefully designed. Since more laterals result in higher mechanical cost, n_L should be optimized to decrease the inter-lateral pressure interference and maximize the economic benefits of this technology.

5.3.5.2 Reservoir Anisotropy Impact

Although in both cases, the existence of the laterals greatly improves the oil production, we observe higher significance of the laterals in the anisotropic reservoir. With a vertical permeability 10 times lower than horizontal permeability, the reservoir connectivity in vertical direction is much lower than that in horizontal direction. Therefore, the fishbone laterals in vertical direction contribute significantly to the overall reservoir-well connectivity. Since the reservoir height is relatively low (100 ft) in our case, this impact can be easily observed. In general, we expect the fishbone to be more effective in anisotropic reservoirs than in isotropic reservoirs.

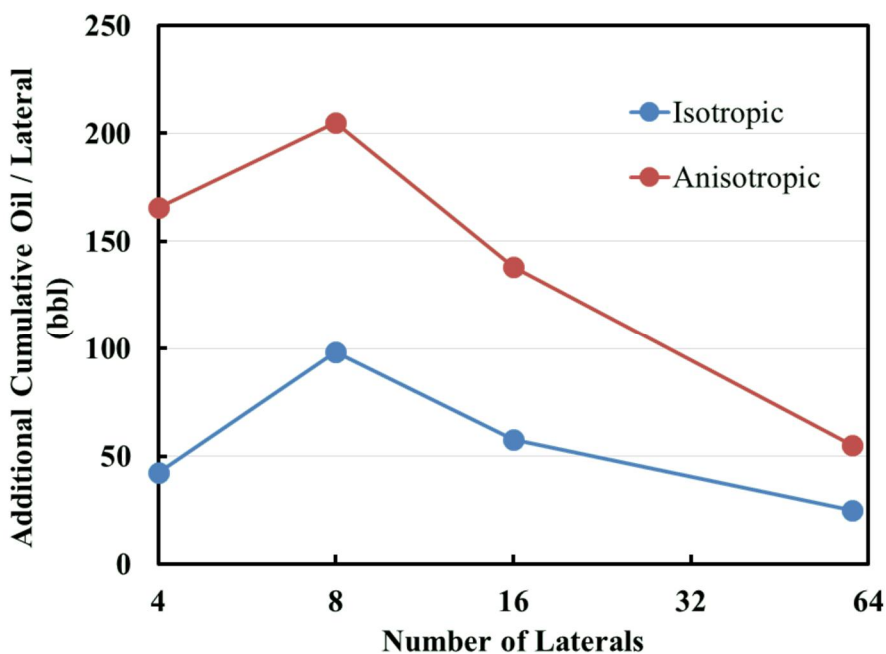


Figure 5.29: Variation of ΔCOP_L with fishbone lateral numbers. The X axis is shown in log scale.

5.3.6 Porosity Cutoff Application

In Chapter 3, we discussed the porosity cutoff method in the EDFM, which can speed up the simulation. Using the isotropic case with 60 fishbone laterals, we perform simulations with different porosity cutoff values ϕ_{cutoff} to investigate the impact of porosity cutoff on both accuracy and computational performance of the EDFM. We performed all the simulation on Petros cluster using one processor. The cluster is owned by the Center for Petroleum and Geosystems Engineering (CPGE) at the University of Texas at Austin. It has 32 compute nodes, and each node has a 16 GB memory and 4 CPUs with the frequency of 2.73 GHz.

Figure 5.30 presents the simulation results with different ϕ_{cutoff} . Table 5.4 shows the corresponding CPU times for the simulations. It can be observed that when using porosity cutoff values of 1×10^{-5} , 1×10^{-4} , and 1×10^{-3} , the simulation results remain almost unchanged. However, the CPU time decreases from 7329 seconds (for no porosity cutoff) to 24 seconds (for $\phi_{cutoff} = 1\times10^{-3}$). Further increase of ϕ_{cutoff} will lead to inaccurate results and the improvement in CPU performance is not significant.

This study confirms the applicability of porosity cutoff method in the EDFM approach. When choosing appropriate ϕ_{cutoff} , this method can greatly improve the CPU performance of the EDFM. However, for different problems, the appropriate value of ϕ_{cutoff} may differ. It is suggested that this value can be determined from numerical experiments similar to the studies we presented here. Generally, we recommend a value of $1\times10^{-4}\sim1\times10^{-3}$ as a first attempt.

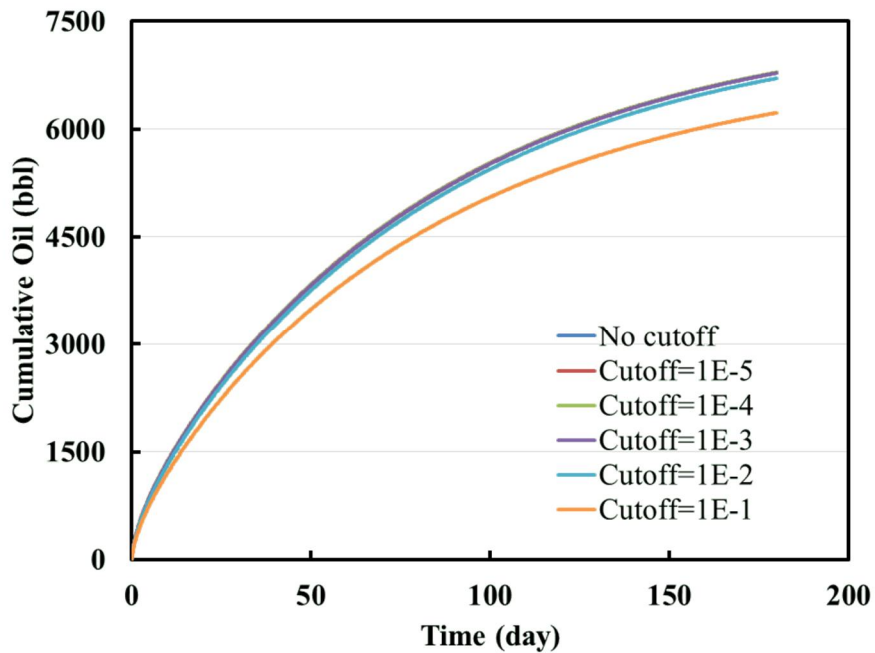


Figure 5.30: Verification of porosity cutoff method for the isotropic case with 60 fishbone laterals.

Porosity Cutoff	No cutoff	1×10^{-5}	1×10^{-4}	1×10^{-3}	1×10^{-2}	1×10^{-1}
CPU Time (second)	7329	4515	110	24	20	18

Table 5.4: CPU time for different porosity cutoff values.

5.4 HIGHLIGHTS OF THE CHAPTER

- Examples of primary depletion from hydraulically fractured reservoir, water flooding in NFR, and primary depletion from fishbone well were presented to show the flexibility, applicability, robustness, and extensiveness of the EDFM approach.
- The intersection angle between hydraulic fractures and the wellbore can be conveniently modeled through the EDFM approach. This angle was shown to

impact the early-time production rate by influencing the inter-fracture pressure interference.

- By using appropriate matrix grid size, the EDFM was shown to be accurate in modeling water flooding processes. The relative permeability curve for fracture cells is important for the simulation results.
- The formulations of the EDFM are modified to model the fishbone well geometry. The accuracy of the modified formulations were confirmed through comparison with a multi-branch well method.
- The positions and spacing of fishbone laterals were shown to impact the pressure interference between well-lateral and lateral-lateral.
- The Fishbones technology was shown to be more effective in anisotropic reservoirs with low vertical permeability.
- The usefulness and accuracy of the porosity cutoff method were confirmed. The simulation time can be greatly reduced when appropriate porosity cutoff value is chosen.

Chapter 6: Summary, Conclusions and Recommendations

In this chapter, the summary and conclusions for this work is presented followed by the recommendations for future work.

6.1 SUMMARY AND CONCLUSIONS

We now present the summary and conclusions of this research as follows:

1. The Embedded Discrete Fracture Model (EDFM) was initially developed by Li and Lee (2008) as a combination of dual-continuum approaches and discrete fracture models (DFM). In this approach, the structured grid for matrix is maintained by discretizing the fracture planes with matrix cell boundaries and adding fracture cells. This approach honors the computational performance of structured grids as well as the accuracy and flexibility of explicit-fracture modeling (such as fracture modeling using unstructured grids). Non-neighboring connections (NNCs) and fracture wellblocks are introduced in the EDFM to account for the flow communications associated with fractures (Li and Lee 2008; Moinfar et al. 2014; Moinfar et al. 2013c).
2. We implemented the EDFM approach in UTCHEM, an in-house reservoir simulator developed at The University of Texas, to study complex fluid flow problems in 3D naturally fractured or hydraulically fractured reservoirs. We presented the modified governing equations in UTCHEM-EDFM to illustrate the implementation.
3. We also applied the EDFM approach in commercial simulators in a non-intrusive way. By adding extra cells in X direction and making use of the non-neighboring connection functionality provided by commercial simulators, we successfully empower these simulators to model complex fractures.

4. We verified the EDFM as well as its implementation in reservoir simulators using a 3D case with intersecting orthogonal fractures. All types of connections in the EDFM were considered in the simulation. By comparing the results with a local grid refinement model, the accuracy of the EDFM was verified.
5. The accuracy of the EDFM for modeling non-orthogonal fractures and inclined fractures was also verified by its match with carefully designed local grid refinement model and fine-grid model, respectively.
6. Several simulation case studies were conducted to show the applicability, robustness, flexibility and extensiveness of the EDFM. The examples involved primary depletion from hydraulically fractured reservoir, water flooding in naturally fractured reservoir, and primary depletion from fishbone well.
7. Flexibility of the EDFM was shown through a series of case studies with different fracture-well intersection angles. The intersection angle greatly influences the early time production in a way that it influences the intensity of inter-fracture pressure interference. The late time production will not be significantly affected due to the radial flow around fractures.
8. We presented a 3D case to show the applicability of the EDFM for modeling water flooding processes in naturally fractured reservoirs. Using appropriate grid resolution, the influence of large-scale natural fractures on the water flooding process was effectively modeled by the EDFM. The relative permeability curve for fracture cells is also shown to be important for water flooding processes as it greatly influence the mobility contrast between water and oil phases in fractures.
9. We presented the modeling of fishbone well geometry to show the extensiveness of the EDFM. With modifications in the transmissibility factor formulations, the EDFM is capable of modeling this multi-lateral well stimulation technology. We

- verified the accuracy of the modified formulations through comparison with a multi-branch well method.
10. The fishbone well geometry was shown to be effective for production improvement, especially for anisotropic reservoirs. The fishbone laterals provide vertical flow paths for fluids and improve the reservoir-well connectivity. In addition, the positions and spacing of the laterals should be optimized through numerical studies. The positions of laterals affect the interference between fishbone and the horizontal well and the distance between adjacent laterals influences inter-lateral pressure interference.
 11. The porosity cutoff method was shown to be accurate and effective in the case studies of fishbone well modeling. An appropriate porosity cutoff value can greatly reduce the computational time while keeping high accuracy.

6.2 RECOMMENDATIONS FOR FUTURE WORK

1. Verify more aspects of the EDFM and its implementation in UTCHEM-EDFM. Although several case studies have been presented in this thesis to verify the accuracy of the model and the implementation, there are still some aspects not involved. For example, for future study of non-isothermal fractured reservoirs, it is highly recommended to validate the modified energy conservation equation in UTCHEM-EDFM with thermal cases.
2. Apply the EDFM using enhanced oil recovery (EOR) processes in reservoir simulations to investigate the influence of hydraulic fractures and natural fractures on the applicability of different EOR methods. As mentioned in Chapter 3, the UTCHEM reservoir simulator is capable of handling various

complex EOR processes, such as polymer flooding, surfactant flooding, and steam injection. With the capability of the EDFM, UTCHEM-EDFM can be a powerful tool for studies of such processes in fractured reservoirs.

3. Integrate the EDFM into the history matching and sensitivity analysis framework. An advantage of the EDFM is its non-intrusive property. Using the EDFM, one can easily change the geometries of fractures in simulations; therefore, the uncertainties associated with fractures can be investigated in sensitivity analysis and history matching.
4. Add permeability tensor for fracture planes. Similar to matrix, the fracture can also have different permeability values in different directions. The permeability anisotropy in fracture plane may have great influence in the modeling of large-scale hydraulic fractures.
5. Evaluate the influence of time-varying fracture properties on well production. The use of fully-coupled fluid flow and geomechanics model is recommended.
6. Investigate the applicability of porosity cutoff method. Conduct a series of numerical experiments to determine the appropriate porosity cutoff values for different types of fractures and reservoirs.
7. Investigate the computational performance of the EDFM and compare it with other fracture simulation approaches, such as local grid refinement and unstructured gridding. Since the EDFM has been applied to commercial simulators, fair comparison in CPU time between the EDFM and other approaches can be made through carefully designed numerical experiments.
8. Combine the EDFM with fracture diagnostic technologies. The fracture diagnostic tools provide the location and geometries of the fractures, which

are the inputs of the EDFM preprocessor. Therefore, the combination of these two technologies can provide a rapid production analysis tool for fractured media.

9. Combine the EDFM with fracture propagation modeling techniques to optimize fracture treatment designs.

Nomenclature

A	contact area
c	compressibility
C	concentration
\hat{C}	adsorbed concentration
\tilde{C}	overall (sum over all phases) volume per unit pore volume
C_p	heat capacity at constant pressure
C_v	heat capacity at constant volume
COP	cumulative oil production
d	distance
d_{seg}	distance from the centroid of segment to the common face
dV	volume element
D	distance between fractures
\bar{D}	dispersive flux
D_{hole}	diameter of open hole
DF	direction factor
F_{cd}	fracture conductivity
h	depth
h_f	height of fracture segment
k	matrix permeability
k_r	relative permeability
K	permeability
$\overrightarrow{\overrightarrow{K}}$	permeability tensor
L	characteristic length of the block
L_{int}	length of the intersection line
\vec{n}	normal vector of the fracture plane
n_{cv}	total number of volume-occupying species

n_L	number of fishbone lateral
n_p	number of phases
n_s	number of common faces a gridblock has with neighboring gridblocks
n_{NNC}	number of non-neighboring connections
N	number of normal sets of fractures
N_B	number of cells
N_{seg}	number of fracture segments
N_x	number of gridblocks in X direction
N_y	number of gridblocks in Y direction
N_z	number of gridblocks in Z direction
P	pressure
P_c	capillary pressure
q	volume flow rate
q_H	enthalpy source term per bulk volume
Q	source/sink term
Q_L	heat loss to overburden and underburden formations or soil
r_L	fishbone lateral radius
r_o	equivalent radius in Peaceman's model
r_w	wellbore radius
R	source term
S	phase saturation or area
t	time
T	reservoir temperature
T_{NNC}	non-neighboring connection transmissibility factor
T_s	transfer function
\vec{u}	flux
V	volume
V_b	bulk volume
w	aperture

W	height of fracture segment
WI	well index
x_n	distance from an area or volume element to the fracture plane

Greek Symbols

α	fracture-well intersection angle
γ	specific gravity
ΔP	potential difference
Δx	block dimension in X direction
Δy	block dimension in Y direction
Δz	block dimension in Z direction
λ_r	relative mobility
λ_T	thermal conductivity
μ	fluid viscosity
ρ	density relative to a reference value
σ	shape factor
ϕ	matrix porosity
ϕ_{cutoff}	porosity cutoff value

Subscripts / Superscripts

c	correction for fluid compressibility
f	fracture
i	index of neighboring connection
j	index of non-neighboring connection
k	component
l	phase
L	fishbone lateral
m	matrix
M_j	non-neighboring gridblock

N_i	neighboring gridblock
NNC	non-neighboring connection
P_R	reference phase pressure
s	soil
seg	fracture segment
t	total
T	total
x	X-coordinate direction
y	Y-coordinate direction
z	Z-coordinate direction
α	phase
\perp	in the direction perpendicular to the fracture plane

Acronyms

CVFE	Control-Volume Finite-Element
DFM	Discrete Fracture Model
DG	Discontinuous Galerkin
EDFM	Embedded Discrete Fracture Model
LGR	Local Grid Refinement
MFE	Mixed-Finite-Element
MINC	Multiple Interacting Continua
MPFA	Multi-Point Flux Approximation
NFR	Naturally Fractured Reservoir
NNC	Non-Neighboring Connection
TPFA	Two-Point Flux Approximation

References

- Abushaikha, A.S. and Gosselin, O.R. 2008. Matrix-Fracture Transfer Function in Dual-Media Flow Simulation: Review, Comparison and Validation. Presented at the Europec/EAGE Conference and Exhibition, Rome, Italy, 9-12 June. SPE-113890-MS. <http://dx.doi.org/10.2118/113890-MS>.
- Baca, R.G., Arnett R.C., and Langford D.W. 1984. Modelling Fluid Flow in Fractured-Porous Rock Masses by Finite-Element Techniques. *International Journal for Numerical Methods in Fluids* **4** (4): 337–348. <http://dx.doi.org/10.1002/fld.1650040404>.
- Barenblatt, G.I., Zheltov, Iu.P., and Kochina I.N. 1960. Basic Concepts in the Theory of Seepage of Homogeneous Liquids in Fissured Rocks. *Journal of Applied Mathematics and Mechanics* **24** (5): 1286–1303. [http://dx.doi.org/10.1016/0021-8928\(60\)90107-6](http://dx.doi.org/10.1016/0021-8928(60)90107-6).
- Bastian, P., Chen, Z., Ewing R.E. et al. 2000. Numerical Simulation of Multiphase Flow in Fractured Porous Media. In Numerical treatment of multiphase flows in porous media, pp. 50-68. Springer Berlin Heidelberg.
- Beckner, B. L., Firoozabadi, A., and Aziz, K. 1988. Modeling Transverse Imbibition in Double-Porosity Simulators. Presented at the SPE California Regional Meeting, Long Beach, California, 23-25 March. SPE-17414-MS. <http://dx.doi.org/10.2118/17414-MS>.
- Berkowitz, B., Naumann, C., and Smith, L. 1994. Mass Transfer at Fracture Intersections: An Evaluation of Mixing Models. *Water Resour. Res.* **30** (6): 1765–1773. <http://dx.doi.org/10.1029/94WR00432>.
- Blaskovich, F.T., Cain, G.M., Sonier, F. et al. 1983. A Multicomponent Isothermal System for Efficient Reservoir Simulation. Presented at the Middle East Oil Technical Conference and Exhibition, Manama, Bahrain, 14-17 March. SPE-11480-MS. <http://dx.doi.org/10.2118/11480-MS>.
- Carvajal, E. I., Caline, Y., Rylance, M. et al. 2015. Open-Hole Completion Based Mechanical Diversion of Acid/Chemical Stimulation Operations: Design, Deployment and Field Trial Results. Presented at the SPE Hydraulic Fracturing Technology Conference, The Woodlands, Texas, 3-5 February. SPE-173355-MS. <http://dx.doi.org/10.2118/173355-MS>.
- Cavalcante Filho, J. S. de A., Shakiba, M., Moinfar, A. et al. 2015. Implementation of a Preprocessor for Embedded Discrete Fracture Modeling in an IMPEC Compositional Reservoir Simulator. Presented at the SPE Reservoir Simulation Symposium, Houston, Texas, 23-25 February. SPE-173289-MS. <http://dx.doi.org/10.2118/173289-MS>.

- Chang, M.-M. 1993. Deriving the Shape Factor of a Fractured Rock Matrix. No. NIPER--696. National Inst. for Petroleum and Energy Research, Bartlesville, OK.
- Chen, C.-C. and Rajagopal, R. 1997. A Multiply-Fractured Horizontal Well in a Rectangular Drainage Region. *SPE J.* **2** (4): 455-465. SPE-37072-PA. <http://dx.doi.org/10.2118/37072-PA>.
- Chen, W. H., Wasserman M.L., and Fitzmorris R. E. 1987. A Thermal Simulator for Naturally Fractured Reservoirs. Presented at the SPE Symposium on Reservoir Simulation, San Antonio, Texas, 1-4 February. SPE-16008-MS. <http://dx.doi.org/10.2118/16008-MS>.
- Cinco-ley, H. and Samaniego-V., F. 1981. Transient Pressure Analysis for Fractured Wells. *J Pet Technol* 33 (09): 1749-1766. SPE-7490-PA. <http://dx.doi.org/10.2118/7490-PA>.
- Cinco-Ley, H., Samaniego-V., F., and Dominguez-A., N. 1978. Transient Pressure Behavior for a Well with a Finite-Conductivity Vertical Fracture. *SPE J.* **18** (4): 253-264. SPE-6014-PA. <http://dx.doi.org/10.2118/6014-PA>.
- Cipolla, C.L., Fitzpatrick, T., Williams, M.J. et al. 2011. Seismic-to-Simulation for Unconventional Reservoir Development. Presented at the SPE Reservoir Characterization and Simulation Conference and Exhibition, Abu Dhabi, 9–11 October. SPE-146876-MS. <http://dx.doi.org/10.2118/146876-MS>.
- Cipolla, C.L., Lolon, E.P., Erdle, J.C. et al. 2010. Reservoir Modeling in Shale-Gas Reservoirs. *SPE Res Eval & Eng* **13** (4): 638-653. SPE-125530-PA. <http://dx.doi.org/10.2118/125530-PA>.
- Cipolla, C. L., Warpinski, N. R., Mayerhofer, M. et al. 2010. The Relationship between Fracture Complexity, Reservoir Properties, and Fracture-Treatment Design. *SPE Prod & Oper* **25** (4): 438-452. SPE-115769-PA. <http://dx.doi.org/10.2118/115769-PA>.
- Cipolla, C.L., Weng, X., Mack, M.G. et al. 2011. Integrating Microseismic Mapping and Complex Fracture Modeling to Characterize Fracture Complexity. Presented at the SPE Hydraulic Fracturing Technology Conference, The Woodlands, Texas, 24-26 January. SPE-140185-MS. <http://dx.doi.org/10.2118/140185-MS>.
- Coats, K.H., Dempsey, J.R., and Henderson, J.H. 1971. The Use of Vertical Equilibrium in Two-Dimensional Simulation of Three-Dimensional Reservoir Performance. *SPE J.* **11** (1): 63–71. SPE-2797-PA. <http://dx.doi.org/10.2118/2797-PA>.
- Daneshy, A.A. 1973. A Study of Inclined Hydraulic Fractures. *SPE J.* **13** (2): 61-68. SPE-4062-PA. <http://dx.doi.org/10.2118/4062-PA>.

Dean R.H., Lo L.L. 1988. Simulations of Naturally Fractured Reservoirs. *SPE Res Eng* **3** (02): 638-648. SPE-14110-PA. <http://dx.doi.org/10.2118/14110-PA>.

Eclipse Reference Manual. 2014. Schlumberger.

Far, M.E., Sayers, C.M., Thomsen, L. et al. 2013. Seismic Characterization of Naturally Fractured Reservoirs Using Amplitude versus Offset and Azimuth Analysis. *Geophysical Prospecting* **61** (2): 427–47. <http://dx.doi.org/10.1111/1365-2478.12011>.

Fernø, M.A. 2012. *Enhanced Oil Recovery in Fractured Reservoirs*. INTECH Open Access Publisher.

Fisher, M.K., Heinze, J.R., Harris, C.D. et al. 2004. Optimizing Horizontal Completion Techniques in the Barnett Shale Using Microseismic Fracture Mapping. Presented at the SPE Annual Technical Conference and Exhibition, Houston, Texas, 26-29 September. SPE-90051-MS. <http://dx.doi.org/10.2118/90051-MS>.

Frantz, J.H., Sawyer, W.K., MacDonald, M.J. et al. 2005. Evaluating Barnett Shale Production Performance-Using an Integrated Approach. Presented at the SPE Annual Technical Conference and Exhibition, 9-12 October, Dallas, Texas. SPE-96917-MS. <http://dx.doi.org/10.2118/96917-MS>.

Freyer, R. and Shaoul, J.R. 2011. Laterals Stimulation Method. Presented at the Brasil Offshore, Macaé, Brazil, 14-17 June. SPE-143381-MS. <http://dx.doi.org/10.2118/143381-MS>.

Fu, Y., Yang, Y.-K., and Deo, M. 2005. Three-Dimensional, Three-Phase Discrete-Fracture Reservoir Simulator Based on Control Volume Finite Element (CVFE) Formulation. Presented at the SPE Reservoir Simulation Symposium, The Woodlands, Texas, 31 January-2 February. SPE-93292-MS. <http://dx.doi.org/10.2523/93292-MS>.

Gale, J. F W, Robert M. Reed, and Jon Holder. 2007. Natural Fractures in the Barnett Shale and Their Importance for Hydraulic Fracture Treatments. *AAPG Bulletin* **91** (4): 603–22. <http://dx.doi.org/10.1306/11010606061>.

Geiger, S., Matthai, S.K., Niessner, J. et al. 2009. Black-Oil Simulations for Three-Component, Three-Phase Flow in Fractured Porous Media. *SPE J.* **14** (2): 338–354. SPE-107485-PA. <http://dx.doi.org/10.2118/107485-PA>.

Gilman, J.R. 1986. An Efficient Finite-Difference Method for Simulating Phase Segregation in the Matrix Blocks in Double-Porosity Reservoirs. *SPE Res Eng* **1** (4): 403–413. SPE-12271-PA. <http://dx.doi.org/10.2118/12271-PA>.

- Gilman, J.R., and Kazemi, H. 1983. Improvements in Simulation of Naturally Fractured Reservoirs. *SPE J.* **23** (4). SPE-10511-PA. <http://dx.doi.org/10.2118/10511-PA>.
- Gringarten, A. C. and Raghavan, R. 1974. Unsteady-State Pressure Distribution Created by a Well with a Single Infinite-Conductivity Vertical Fracture. *SPE J.* **14** (4): 347–360. SPE-4051-PA. <http://dx.doi.org/10.2118/4051-PA>.
- Hajibeygi, H., Karvounis, D. and Jenny, P. 2011. A Hierarchical Fracture Model for the Iterative Multiscale Finite Volume Method. *J. Comput.Phys.* **230** (24): 8729-8743. <http://dx.doi.org/10.1016/j.jcp.2011.08.021>.
- Hill, A.C., and Thomas, G.W. 1985. A New Approach for Simulating Complex Fractured Reservoirs. Presented at the Middle East Oil Technical Conference and Exhibition, Bahrain, 11-14 March. SPE-13537-MS. <http://dx.doi.org/10.2118/13537-MS>.
- Hoteit, H. and Firoozabadi, A. 2006. Compositional Modeling of Discrete-Fractured Media Without Transfer Functions by the Discontinuous Galerkin and Mixed Methods. *SPE J.* **11** (3): 341-352. SPE-90277-PA. <http://dx.doi.org/10.2118/90277-PA>.
- Hui, M.-H., Mallison, B. T., Fyrozjaee, M. H. et al. 2013. The Upscaling of Discrete Fracture Models for Faster, Coarse-Scale Simulations of IOR and EOR Processes for Fractured Reservoirs. Presented at the SPE Annual Technical Conference and Exhibition New Orleans, Louisiana, 30 September-2 October. SPE-166075-MS. <http://dx.doi.org/10.2118/166075-MS>.
- IMEX User Guide*. 2014. Computer Modeling Group.
- Jiang, J., Shao, Y., and Younis, R. M. 2014. Development of a Multi-Continuum Multi-Component Model for Enhanced Gas Recovery and CO₂ Storage in Fractured Shale Gas Reservoirs. Presented at the SPE Improved Oil Recovery Symposium, Tulsa, Oklahoma, 12-16 April. SPE-169114-MS. <http://dx.doi.org/10.2118/169114-MS>.
- Juanes, R., Samper, J., and Molinero, J. 2002. A General and Efficient Formulation of Fractures and Boundary Conditions in the Finite Element Method. *International Journal for Numerical Methods in Engineering* **54** (12): 1751-1774. <http://dx.doi.org/10.1002/nme.491>.
- Karimi-Fard, M., Durlofsky, L. J. and Aziz, K. 2004. An Efficient Discrete-Fracture Model Applicable for General-Purpose Reservoir Simulators. *SPE J.* **9** (2): 227-236. SPE-88812-PA. <http://dx.doi.org/10.2118/88812-PA>.

- Karimi-Fard, M. and Firoozabadi, A. 2003. Numerical Simulation of Water Injection in Fractured Media using the Discrete-Fractured Model and the Galerkin Method. *SPE Res Eval & Eng* **6** (2): 117-126. SPE-83633-PA. <http://dx.doi.org/10.2118/83633-PA>.
- Kazemi, H. 1969. Pressure Transient Analysis of Naturally Fractured Reservoirs with Uniform Fracture Distribution. *SPE J.* **9** (4): 451-462. SPE-2156-A. <http://dx.doi.org/10.2118/2156-A>.
- Kazemi, H., Merrill, L.S., Porterfield K.L. et al. 1976. Numerical Simulation of Water-Oil Flow in Naturally Fractured Reservoirs. *SPE J.* **16** (6): 317-26. SPE-5719-PA. <http://dx.doi.org/10.2118/5719-PA>.
- Kim, J.-G., and Deo, M.D. 2000. Finite Element, Discrete-Fracture Model for Multiphase Flow in Porous Media. *AIChE Journal* **46** (6): 1120-1130. <http://dx.doi.org/10.1002/aic.690460604>.
- Lee, C.H., Yu, J.-L., and Hwung, H.-H. 1993. Fluid Flow and Connectivity in Fractured Rock. *Water Resources Management* **7** (2): 169-184. <http://dx.doi.org/10.1007/BF00872480>.
- Lee, S.H., Lough, M.F. and Jensen, C.L. 2001. Hierarchical Modeling of Flow in Naturally Fractured Formations with Multiple Length Scales. *Water Resour. Res.* **37** (3): 443-455. <http://dx.doi.org/10.1029/2000WR900340>.
- Lemonnier, P. and Bourbiaux, B. 2010. Simulation of Naturally Fractured Reservoirs. State of the Art. *Oil Gas Sci. Technol.* **65** (2): 239-262. <http://dx.doi.org/10.2516/ogst/2009067>.
- Li, L. and Lee, S.H. 2008. Efficient Field-Scale Simulation of Black Oil in a Naturally Fractured Reservoir Through Discrete Fracture Networks and Homogenized Media. *SPE Res Eval & Eng* **11** (4): 750-758. SPE-103901-PA. <http://dx.doi.org/10.2118/103901-PA>.
- Li, X., Zhang, D., and Li, S. 2015. A Multi-Continuum Multiple Flow Mechanism Simulator for Unconventional Oil and Gas Recovery. *Journal of Natural Gas Science and Engineering* **26**: 652-69. <http://dx.doi.org/10.1016/j.jngse.2015.07.005>.
- Lim, K.T. and Aziz, K. 1995. Matrix-Fracture Transfer Shape Factors for Dual-Porosity Simulators. *Journal of Petroleum Science and Engineering* **13** (3-4): 169-178.
- Litvak, B. L. 1985. Simulation and Characterization of Naturally Fractured Reservoirs. *Proc., Reservoir Characterization Technical Conference*, Dallas, Texas, 29 April-1 May.
- Manrique, E.J., Muci, V.E., and Gurfinkel, M. E. 2007. EOR Field Experiences in Carbonate Reservoirs in the United States. *SPE Res Eval & Eng* **10** (6): 667-686. SPE-100063-PA. <http://dx.doi.org/10.2118/100063-PA>.

- Maricic, N., Mohaghegh, S. D., and Artun, E. 2008. A Parametric Study on the Benefits of Drilling Horizontal and Multilateral Wells in Coalbed Methane Reservoirs. *SPE Res Eval & Eng* **11** (6): 9–12. SPE-96018-PA. <http://dx.doi.org/10.2118/96018-PA>.
- Matthai, S. K., Geiger, S., Roberts, S. G et al. 2007. Numerical Simulation of Multi-Phase Fluid Flow in Structurally Complex Reservoirs. Geological Society, London, Special Publications 292 (1): 405–429. <http://dx.doi.org/10.1144/SP292.22>.
- Matthai, S., Menzentsev, A. ,and Belayneh, M. 2005. Control-VolumeFinite-Element Two Phase Flow Experiments with Fractured Rock Represented byUnstructured 3D Hybrid Meshes. Presented at the SPE ReservoirSimulation Symposium, The Woodlands, Texas, 31 January-2 February. SPE-93341-MS. <http://dx.doi.org/10.2118/93341-MS>.
- Maxwell, S. C., Urbancic, T. I., Steinsberger, N., & Zinno et al. 2002. Microseismic Imaging of Hydraulic Fracture Complexity in the Barnett Shale. Presented at the SPE Annual Technical Conference and Exhibition, San Antonio, Texas, 29 September-2 October. SPE-77440-MS. <http://dx.doi.org/10.2118/77440-MS>.
- Moinfar, A., Narr, W., Hui, M.-H. et al. 2013. Comparison of Discrete-Fracture and Dual-Permeability Models for Multiphase Flow in Naturally Fractured Reservoirs. Presented at the SPE Reservoir Simulation Symposium, The Woodlands, Texas, 21-23 February. SPE-142295-MS. <http://dx.doi.org/10.2118/142295-MS>.
- Moinfar, A., Sepehrnoori, K., Johns, R.T. et al. 2013. Coupled Geomechanics and Flow Simulation for an Embedded Discrete Fracture Model. Presented at the SPE Reservoir Simulation Symposium, The Woodlands, Texas, 18-20 February. SPE-163666-MS. <http://dx.doi.org/10.2118/163666-MS>.
- Moinfar, A., Varavie, A., Sepehrnoori, K. et al. Development of a Coupled Dual Continuum and Discrete Fracture Model for the Simulation of Unconventional Reservoirs. Presented at the SPE Reservoir Simulation Symposium, The Woodlands, Texas, 18-20 February. SPE-163647-MS. <http://dx.doi.org/10.2118/163647-MS>.
- Moinfar, A., Varavei, A., Sepehrnoori, K. et al. 2014. Development of an Efficient Embedded Discrete Fracture Model for 3D Compositional Reservoir Simulation in Fractured Reservoirs. *SPE J.* **19** (2): 289-303. SPE-154246-PA. <http://dx.doi.org/10.2118/154246-PA>.
- Monteagudo, J. and Firoozabadi, A. 2004. Control-Volume Method for NumericalSimulation of Two-Phase Immiscible Flow in Two- and Three-DimensionalDiscrete-Fractured Media. *Water Resour. Res.* **40** (7): 1-20. <http://dx.doi.org/10.1029/2003WR002996>.

Nelson, R. 2001. *Geologic Analysis of Naturally Fractured Reservoirs*. Gulf Professional Publishing.

Noorishad, J. and Mehran, M. 1982. An Upstream Finite Element Method for Solution of Transient Transport Equation in Fractured Porous Media. *Water Resour. Res.* **18** (3): 588-596. <http://dx.doi.org/10.1029/WR018i003p00588>.

Oda, M. 1985. Permeability Tensor for Discontinuous Rock Masses. *Geotechnique*, **35** (4), 483-495. <http://dx.doi.org/10.1680/geot.1985.35.4.483>.

Olson, J. E. 2008. Multi-fracture propagation modeling: Applications to hydraulic fracturing in shales and tight gas sands. Presented at the 42nd U.S. Rock Mechanics Symposium (USRMS), San Francisco, California, 29 June-2 July.

Paluszny, A., Matthai, S. K., and Hohmeyer, M. 2007. Hybrid Finite Element-Finite Volume Discretization of Complex Geologic Structures and a New Simulation Workflow Demonstrated on Fractured Rocks. *Geofluids* **7** (2): 186–208. <http://dx.doi.org/10.1111/j.1468-8123.2007.00180.x>.

Panfili, P. and Cominelli, A. 2014. Simulation of Miscible Gas Injection in a Fractured Carbonate Reservoir using an Embedded Discrete Fracture Model. Presented at the Abu Dhabi International Petroleum Exhibition and Conference, Abu Dhabi, 10-13 November. SPE-171830-MS. <http://dx.doi.org/10.2118/171830-MS>.

Peaceman, D.W. 1983. Interpretation of Well-Block Pressures in Numerical Reservoir Simulation With Nonsquare Grid Blocks and Anisotropic Permeability. *SPE J.* **23** (3): 531–543. SPE-10528-PA. <http://dx.doi.org/10.2118/10528-PA>.

Pope, G.A. and Nelson, R.C. 1978. A Chemical Flooding Compositional Simulator. *SPE J.* **18** (5): 339–54. SPE-6725-PA. <http://dx.doi.org/10.2118/6725-PA>.

De la Porte, J. J., Kossack, C. A., and Zimmerman, R. W. 2005. SPE 95241 The Effect of Fracture Relative Permeabilities and Capillary Pressures on the Numerical Simulation of Naturally Fractured Reservoirs. Presented at the SPE Annual Technical Conference and Exhibition, Dallas, Texas, 9-12 October. SPE-95241-MS. <http://dx.doi.org/10.2118/95241-MS>.

Pruess, K., and Narasimhan, T.N. 1985. A Practical Method for Modeling Fluid and Heat Flow in Fractured Porous Media. *SPE J.* **25** (1): 14–26. SPE-10509-PA. <http://dx.doi.org/10.2118/10509-PA>.

- Pruess, K., and Narasimhan, T. N. 1982. On Fluid Reserves and the Production of Superheated Steam from Fractured, Vapor-Dominated Geothermal Reservoirs. *Journal of Geophysical Research* **87** (B11): 9329. <http://dx.doi.org/10.1029/JB087iB11p09329>.
- Raghavan, R. S., Chen, C. C., and Agarwal, B. 1997. An Analysis of Horizontal Wells Intercepted by Multiple Fractures. *SPE J.* **2** (3): 235–245. SPE-27652-PA. <http://dx.doi.org/10.2118/27652-PA>.
- Reiss, L.H. 1980. *The Reservoir Engineering Aspects of Fractured Formations*, Vol. 3. Editions Technip.
- Rice, K., Jorgensen T., and Waters, J. 2014. First Installation of Efficient and Accurate Multilaterals Stimulation Technology in Carbonate Oil Application. Presented at the SPE Eastern Regional Meeting, Charleston, WV, 21-23 October. SPE-171021-MS. <http://dx.doi.org/10.2118/171021-MS>.
- Rossen, R.H. 1977. Simulation of Naturally Fractured Reservoirs with Semi-Implicit Source Terms. *SPE J.* **17** (3): 201–210. SPE-5737-PA. <http://dx.doi.org/10.2118/5737-PA>.
- Rossen, R.H., and Shen, E.I.C. 1989. Simulation of Gas/Oil Drainage and Water/Oil Imbibition in Naturally Fractured Reservoirs. *SPE Res Eng* **4** (4): 464-470. SPE-16982-PA. <http://dx.doi.org/10.2118/16982-PA>.
- Saidi, A.M. 1983. Simulation of Naturally Fractured Reservoirs. Presented at the SPE Reservoir Simulation Symposium, San Francisco, California, 15-18 November. SPE-12270-MS. <http://dx.doi.org/10.2118/12270-MS>.
- Sandve, T. H., Berre, I., and Nordbotten, J. M. 2012. An efficient multi-point flux approximation method for Discrete Fracture–Matrix Simulations. *Journal of Computational Physics* **231** (9): 3784-3800. <http://dx.doi.org/10.1016/j.jcp.2012.01.023>
- Shakiba, M. 2014. *Modeling and Simulation of Fluid Flow in Naturally and Hydraulically Fractured Reservoirs Using Embedded Discrete Fracture Model (EDFM)*. MS Thesis, The University of Texas at Austin, Austin, Texas (December 2014).
- Shakiba, M. and Sepehrnoori, K. 2015. Using Embedded Discrete Fracture Model (EDFM) and Microseismic Monitoring Data to Characterize the Complex Hydraulic Fracture Networks. Presented at the SPE Annual Technical Conference and Exhibition, Houston, Texas, 28-30 September. SPE-175142-MS. <http://dx.doi.org/10.2118/175142-MS>.
- Thomas L.K., Dixon T.N., and Pierson R.G. 1983. Fractured Reservoir Simulation, *SPE J.* **23** (1): 42-54. SPE-9305-PA. <http://dx.doi.org/10.2118/9305-PA>.

UTCHEM Technical Documentation. 2011. The University of Texas at Austin.

Wan, J., and K. Aziz. 2002. Semi-Analytical Well Model of Horizontal Wells with Multiple Hydraulic Fractures. *SPE J.* **7** (4): 26–27. SPE81190-PA. <http://dx.doi.org/10.2118/81190-PA>.

Warpinski, N. R., Mayerhofer, M. J., Vincent et al. 2009. Stimulating Unconventional Reservoirs: Maximizing Network Growth While Optimizing Fracture Conductivity. *J Can Pet Technol* **48** (10): 39–51. SPE-114173-PA. <http://dx.doi.org/10.2118/114173-PA>.

Warren, J.E. and Root, P.J. 1963. The Behavior of Naturally Fractured Reservoirs. *SPE J.* **3** (3): 245-255. SPE-426-PA. <http://dx.doi.org/10.2118/426-PA>.

Weng, X., Kresse, O., Cohen, C.-E. et al. 2011. Modeling of Hydraulic-Fracture-Network Propagation in a Naturally Fractured Formation. *SPE Prod & Oper* **26** (4): 368-380. SPE-140253-PA. <http://dx.doi.org/10.2118/140253-PA>.

Wu, K. and Olson, J. E. 2014. Mechanics Analysis of Interaction Between Hydraulic and Natural Fractures in Shale Reservoirs. Presented at the SPE/AAPG/SEG Unconventional Resources Technology Conference, Denver, Colorado, 25-27 August. SPE-2014-1922946-MS. <http://dx.doi.org/10.15530/urtec-2014-1922946>.

Wu, K. and Olson, J. E. 2015. Simultaneous Multifracture Treatments: Fully Coupled Fluid Flow and Fracture Mechanics for Horizontal Wells. *SPE J.* **20** (2): 337-346. SPE-167626-PA. <http://dx.doi.org/10.2118/167626-PA>.

Wu, Y.-S. and Pruess, K. 1988. A Multiple-Porosity Method for Simulation of Naturally Fractured Petroleum Reservoirs. *SPE Res Eng* **3** (1): 327–336. SPE-15129-PA. <http://dx.doi.org/10.2118/15129-PA>.

Yu, W., Huang, S., Wu, K. et al. 2014. Development of a Semi-Analytical Model for Simulation of Gas Production in Shale Gas Reservoirs. Society of Petroleum Engineers. Presented at the SPE/AAPG/SEG Unconventional Resources Technology Conference, Denver, Colorado, 25-27 August. SPE-2014-1922945-MS. <http://dx.doi.org/10.15530/urtec-2014-1922945>.

Wei, Y., Wu, K., and Sepehrnoori, K. 2015. A Semianalytical Model for Production Simulation From Nonplanar Hydraulic-Fracture Geometry in Tight Oil Reservoirs. *SPE J.* SPE-178440-PA. (in press; posted October 2015).

Xiance, Y., Guo, B., Ai, C. et al. 2009. A comparison between multi-fractured horizontal and fishbone wells for development of low-permeability fields. Presented at the Asia Pacific

Oil and Gas Conference & Exhibition, Jakarta, Indonesia, 4-6 August. SPE-120579-MS.
<http://dx.doi.org/10.2118/120579-MS>.

Zhou, W., Banerjee, R., Poe, B. et al. 2014. Semianalytical Production Simulation of Complex Hydraulic-Fracture Networks. *SPE J.* **19** (1): 6 – 18. SPE-157367-PA.
<http://dx.doi.org/10.2118/157367-PA>.